

UNIVERSITY OF L'AQUILA

MASTER THESIS

**Reduced order methods for
computational fluid dynamics
parametric problems with finite
volume discretization**

Author:
Saddam N.Y. HIJAZI

Supervisor:
Prof. Corrado LATTANZIO
External Supervisor:
Prof. Gianluigi ROZZA
Co-Advisors:
Dr Andrea MOLA
Dr Giovanni STABILE

*A thesis submitted in fulfillment of the requirements
for the degree of Master of science*

in the

Erasmus Mundus Joint Program Mathematical Modelling in
Engineering (MATHMODS)
Department of Mathematics and Computer Science DISIM

October 5, 2016

Declaration of Authorship

I, Saddam N.Y. HIJAZI, declare that this thesis titled, "Reduced order methods for computational fluid dynamics parametric problems with finite volume discretization" and the work presented in it are my own. I confirm that:

- This work was done wholly or mainly while in candidature for a research degree at this University.
- Where any part of this thesis has previously been submitted for a degree or any other qualification at this University or any other institution, this has been clearly stated.
- Where I have consulted the published work of others, this is always clearly attributed.
- Where I have quoted from the work of others, the source is always given. With the exception of such quotations, this thesis is entirely my own work.
- I have acknowledged all main sources of help.
- Where the thesis is based on work done by myself jointly with others, I have made clear exactly what was done by others and what I have contributed myself.

Signed:

Date:

“Stand on the battlefield of your dream and fight for it.”

Mahmoud Darwish

UNIVERSITY OF L'AQUILA

*Abstract*Erasmus Mundus Joint Program Mathematical Modelling in Engineering
(MATHMODS)

Department of Mathematics and Computer Science DISIM

Master of science

**Reduced order methods for computational fluid dynamics parametric
problems with finite volume discretization**

by Saddam N.Y. HIJAZI

Reduced order modelling (ROM) has become a very important tool in computational sciences and engineering, where in these fields we have a numerous number of emerging applications in which ROM has played a very powerful role. In particular, problems coming from multi physics and multi-scale problems have benefited from the presence of ROM as a new tool to reduce computational cost very effectively.

Before going into more details about the history of ROM, let us just have a brief overview of historical aspects of mathematical modelling and numerical analysis as two main branches of applied mathematics. In our life we have many problems that appear in engineering, physics or life sciences for which we will try to build a mathematical model that can describe those phenomena in a proper way and it happens very often that it is described by a partial differential equation (PDE) as a model of our problem: this PDE can be solved very rarely using analytical techniques, so from here it becomes very important the need for finding an alternative approach for solving this PDE and this is what numerical analysis of PDE can do, such that is we have to develop a numerical scheme to solve the PDE efficiently, in order to obtain a suitable approximation. Before going through the process of solving the PDE and implementing the numerical scheme we have to look on the underlying nature of the problem and to classify what type of PDE we have in our problem, then it comes the study of the issues of well-posedness and regularity of the solution which might be helpful in sorting out what kind of numerical scheme we would need and which simulator to use for solving the problem. Another thing to be checked is about some features of the numerical scheme, like the convergence and the stability, as well as the computational efficiency of our scheme, since it is very important to bear in mind that we have usually limited resources for computation and that can be a problem if it is not taken into consideration.

Acknowledgements

Thanks to ALLAH, the most beneficent, the most merciful, whose blessings allow me to successfully complete my master Thesis. I would like to express my deepest thanks to my highly respected Professor Gianluigi Rozza for his advises, guidance, patience and encouraging words during the time I needed it most, also I want to thank all my other advisors in this thesis: Professor Corrado Lattanzio, Dr Andrea Mola and Dr Giovanni Stabile for helping and guiding me in writing this thesis, also I want to express my gratitude to Dr Stefano Lorenzi for his great help and patience. I would like to thank all the team of mathlab in SISSA and my colleagues for being near by me always and willing to help as much as they can. I want to say thanks to all MATHMODS coordinators, student helpers, staff and students for these two incredible years here in Italy and Germany, It has been my pleasure to meet you and to learn from you.

This thesis work is dedicated to my parents, my brothers and all my family. A special dedication to my professors back in Palestine who motivate me always to take this step.

Contents

Declaration of Authorship	iii
Abstract	vii
Acknowledgements	ix
1 Introduction and motivation	1
1.1 Historical background of ROM	1
1.2 The full order problem: Flow past a circular cylinder	1
1.3 Thesis structure	2
1.3.1 Reduced Order Methods for circular cylinders	3
Semi-empirical methods	3
Simplified wake models	3
Reduced Basis Methods	3
2 Flow past a circular cylinder: Theory	5
2.1 Flow around a circular cylinder	5
2.1.1 Forces on a cylinder	5
2.2 Strouhal number	6
2.3 Vortex-induced vibration	8
2.4 Dynamics of cylinders	9
3 Flow past a circular cylinder: Simulations and Results	15
3.1 Problem setup	15
3.1.1 Computational domain	15
3.1.2 Fluid properties	15
3.1.3 Methodology	15
3.1.4 Boundary conditions	17
3.2 VIV analysis	17
Equation of motion	17
3.2.1 Main case analysis	19
Initial conditions	19
Data sampling	20
Data analysis	20
Analysis of results	21
4 Reduced order methods	31
4.1 Parameterized Variational Problems	31
4.1.1 Parametric Weak Formulation	31
4.1.2 Inner Products, Norms and Well-Posedness of the Parametric Weak Formulation	32
4.2 Discretization Techniques	33
4.3 The Solution Manifold and the Reduced Basis Approximation	34
4.4 Reduced Basis Space Generation	36

4.4.1	Proper Orthogonal Decomposition (POD)	37
4.5	POD-Galerkin projection with Finite Volume	38
5	Reduced order results for the flow past a cylinder	47
5.1	Numerical simulations results	47
5.2	Conclusions and future work	57
A	Simulation results for the full order problem	61

List of Figures

2.1	Drag coefficient for a smooth circular cylinder	6
2.2	Regimes of flow around a smooth circular cylinder	7
2.3	Relation between Strouhal and Reynolds numbers	8
2.4	Strouhal number in terms of Re in Transitional-Turbulent regime	9
2.5	Hysteresis captured by Khalak	10
2.6	differences between high- $m^*\zeta$ and low- $m^*\zeta$	11
2.7	The frequency response for different $m^*\zeta$	13
3.1	The Computational domain	16
3.2	The structure system for elastically mounted cylinder	18
3.3	Results for a cylinder immersed in horizontal stream at Re=2000	22
3.4	Results for a cylinder immersed in horizontal stream at Re=3000	25
3.5	Frequency spectrum	26
3.6	Results for a cylinder immersed in horizontal stream at Re=10000	27
3.7	Frequency spectrum	28
3.8	The curve of reduced frequency versus reduced velocity-The impulsive case and a comparison with Khalak experiments	28
3.9	The curve of reduced amplitude versus reduced velocity-The impulsive case, comparison between our results and Khalak experiments	29
4.1	Example of a control volume in FVD	40
4.2	Non-orthogonality treatment of the diffusive term	41
5.1	Lift Coefficient history for the cylinder case Re=100	48
5.2	Comparison between velocity fields for the case of the cylinder immersed in flow at Re=100 at time=2229.37 with the error being the magnitude of the difference divided by the L^2 -norm	50
5.3	Comparison between pressure fields for the case of the cylinder immersed in flow at Re=100 at time=2229.37 with the error being the absolute value of the difference divided by the L^2 -norm	51
5.4	High fidelity VS ROM lift coefficient for Re=100 with different number of snapshots	52
5.5	High fidelity VS ROM lift coefficient for Re=100 with different number of modes nPOD= 3 and 2	52
5.6	High fidelity VS ROM lift coefficient for Re=100 with different number of modes nPOD= 5 and 10	53
5.7	High fidelity VS ROM lift coefficient for Re=100 with different number of modes nPOD= 8 and 13	53

5.8	Comparison between velocity fields for the case of a fixed cylinder immersed in flow at $Re=6000$ at time=82 with the error being the magnitude of the difference divided by the L^2 -norm	54
5.9	Comparison between pressure fields for the case of the cylinder immersed in flow at $Re=100$ at time=2229.37 with the error being the absolute value of the difference divided by the L^2 -norm	55
5.10	Lift coefficient for a fixed cylinder at $Re=6000$	56
5.11	Lift coefficient for a fixed cylinder at $Re=6000$	56
5.12	Lift coefficient: Full order (OpenFOAM) VS Reduced order	58
5.13	Amplitude spectrum of the lift coefficient signal obtained by ROM when snapshots used from five different simulations, where in ROM a velocity corresponds to $Re=125$ has been sought	58
A.1	Results for a cylinder immeresed in horizontal stream at $Re=2000$	62
A.2	Results for a cylinder immeresed in horizontal stream at $Re=2500$	63
A.3	Results for a cylinder immeresed in horizontal stream at $Re=3000$	64
A.4	Results for a cylinder immeresed in horizontal stream at $Re=3500$	65
A.5	Results for a cylinder immeresed in horizontal stream at $Re=4000$	66
A.6	Results for a cylinder immeresed in horizontal stream at $Re=4500$	67
A.7	Results for a cylinder immeresed in horizontal stream at $Re=5000$	68
A.8	Results for a cylinder immeresed in horizontal stream at $Re=5500$	69
A.9	Results for a cylinder immeresed in horizontal stream at $Re=6000$	70
A.10	Results for a cylinder immeresed in horizontal stream at $Re=6500$	71
A.11	Results for a cylinder immeresed in horizontal stream at $Re=7000$	72
A.12	Results for a cylinder immeresed in horizontal stream at $Re=7500$	73
A.13	Results for a cylinder immeresed in horizontal stream at $Re=8000$	74
A.14	Results for a cylinder immeresed in horizontal stream at $Re=8500$	75
A.15	Results for a cylinder immeresed in horizontal stream at $Re=9000$	76
A.16	Results for a cylinder immeresed in horizontal stream at $Re=9500$	77
A.17	Results for a cylinder immeresed in horizontal stream at $Re=10000$	78
A.18	Results for a cylinder immeresed in horizontal stream at $Re=11000$	79
A.19	Results for a cylinder immeresed in horizontal stream at $Re=11500$	80
A.20	Results for a cylinder immeresed in horizontal stream at $Re=11600$	81
A.21	Results for a cylinder immeresed in horizontal stream at $Re=11620$	82
A.22	Results for a cylinder immeresed in horizontal stream at $Re=11630$	83
A.23	Results for a cylinder immeresed in horizontal stream at $Re=11640$	84
A.24	Results for a cylinder immeresed in horizontal stream at $Re=11650$	85
A.25	Results for a cylinder immeresed in horizontal stream at $Re=11700$	86
A.26	Results for a cylinder immeresed in horizontal stream at $Re=12000$	87
A.27	Results for a cylinder immeresed in horizontal stream at $Re=12000$	88

List of Tables

3.1	Results summary	24
5.1	The error in L^2 -norm for the ROM lift coefficient with varying the number of modes used	49

Dedicated to my parents and all my family

Chapter 1

Introduction and motivation

1.1 Historical background of ROM

The basic idea of ROM comes from the need of finding appropriate problem dependent bases which are able to represent parameterized solutions of PDES. There were many early works in this area by introducing some approaches which have been extended to general finite-dimensional systems as well as some classes of differential equations [4] and [45]. In those early works there were some aspects needed to be enhanced like the lack of a posteriori error estimators which arises some questions about how much accurate is the reduced order method since a posteriori error estimator is crucial for determining the reliability of the output. Through the time, different approaches have been created like the development of the effective sampling strategies, particularly the cases of many parameters like [10] and [34]. These sampling techniques are usually of greedy nature, they have similar goal but different approach with other well-known methods of Proper Orthogonal Decomposition (POD), while the former is directly applicable in the multi-dimensional parameter domain, the latter is most often applied only in the one-dimensional space. New techniques also have been utilized for determining the sought basis: here we refer to the greedy approach which has many advantages over the POD but with the constraint of having a posteriori error bounds. For the comparison between POD and greedy approach we refer to [21] and [48]. The ROM has been extended to different kind of problems which are more complicated like non coercive problems, non linear problems and time dependent problems. Also it is true that it has been forced initially to work with finite element discretizations but then it has been extended to other discretizations techniques, for example a systematic finite volume framework for reduced basis approximation and a posteriori error estimation has been developed in [12].

1.2 The full order problem: Flow past a circular cylinder

After we have just given a glimpse of what is ROM then we need to provide the reader an idea about our original high order problem (here it is referred always to the problem that we have initially, before applying ROM on it, as the high order problem, as matter of convention), our problem is really a general problem, which might occur in various fields of engineering and that was the motivation for going through it deeper and trying to figure out most the characteristics of this problem using reduced order modelling (ROM), by an efficient tool for reducing the computational costs and still

getting accurate and reliable results which keep important features of the output of the physical problem.

Flow around a circular cylinder is a fluid structure problem which has attracted many scientists from various fields like mathematics and engineering in order to study this problem and to analyze the behavior of the fluid in it, in this problem there is one important phenomena that can be observed which is Vortex Induced Vibrations (VIV). VIV generally are some kind of motions which are induced on bodies interacting with an external fluid flow. VIV phenomena takes place in many engineering situations like in bridges design, aircraft control surfaces, transmission lines, marine cables, offshore structures and raisers used to transport oil from underwater. If we want to illustrate VIV with one simple example we can just think about a cylinder placed underwater which is placed in a way allowing it to move through the water just in the direction perpendicular to its axis then the flow around the cylinder will be slowed down while in contact with its surface which forms the boundary layer which can separate from the body and then vortices are formed changing the pressure distribution along the surface. When the vortices are not formed symmetrically around the body (with respect to its midplane), different lift forces develop on each side of the body, thus leading to motion transverse to the flow. This motion changes the nature of the vortex formation in such a way as to lead to a limited motion amplitude (differently, than, from what would be expected in a typical case of resonance. So briefly we study VIV phenomena because it can be a source of fatigue damage for important engineering design structures, like bridges and offshore platforms. We will see more details of our problem later on in Chapter 2.

1.3 Thesis structure

This thesis is organized as follows:

Chapter 2 gives an overview of the theory behind flow over circular cylinders and Vortex Induced Vibration studies.

Chapter 3 shows the main case analysis for our problem, where we have shown the problem setup and we talked about the methodology of our work. We have presented our results for the simulations conducted with the main case, finally we tried to build comparisons with the experimental results.

Chapter 4 introduces the reduced order methods; we have started with a small introduction about the parameterized partial differential equations and then we introduce the notion of the solution manifold, truth problem and reduced order bases. Then, we describe the POD method and how it can be applied in finite volume discretization. After that, we have shown the procedure of applying POD for Navier Stokes equations and Reynolds Averaged Navier Stokes (RANS) equation for laminar and turbulent flows, respectively.

In **Chapter 5** Here we show our results for the reduced order solution of the lift coefficient in our cylinder problem. Also we presented some ideas about how to improve the results and what are the future goals and perspectives to further develop the methodology.

1.3.1 Reduced Order Methods for circular cylinders

In this subsection it is presented an overview regarding existing reduced order methods for the analysis of the fluid forces acting on circular cylinders subjected to VIV. Although a lot of research has been performed in this field, three basic different methods to reduce the computational complexity of the behavior of a cylinders subjected to VIV can be found:

- Semi-empirical methods.
- Simplified wake models.
- Reduced basis methods.

Semi-empirical methods

These methods are widely used by numerous authors and are nowadays the standard for many commercial codes used in offshore engineering such as VIVA [59, 67], VIVANA [28, 29], SHEAR7 [60, 61]. The instantaneous amplitude of oscillation is evaluated using appropriate force coefficients. These are evaluated on experimental tests on rigid cylinders undergoing free or forced vibrations. The assumption of only cross flow motion is made. In this approach the response of the structure is evaluated in frequency domain and it is normally assumed that the cylinder is oscillating only in cross-flow direction. Within this method, natural frequencies of the structure are evaluated and than the modes which are most likely to be excited by the vortex shedding are identified.

Simplified wake models

These models, instead of completely solving the flow field, model the flow forces using simplified models. The 3-dimensionality of the problem is reconstructed using a strip theory. Most of the simplified model present in literature are able to predict only the hydrodynamic forces for the cross-flow direction [33]. The fluctuating value of the drag is normally not considered and when taken into account is supposed to be independent from the lift coefficient [13]. Large parts of the proposed models are based on the idea of the wake oscillator [51]. In this approach, the dynamics of the wake behind the cylinder is modelled by one single variable which is supposed to satisfy a non-linear differential equation which is self-excited and self-limited. For this purpose, systems normally used to model vortex shedding on static cylinders, such as the Rayleigh [19] or the van der Pol equations, are extended [13, 55] with a forcing term depending on the motion of the cylinders. In the work proposed by Stabile a wake oscillator model is used to model forces along the cross-flow direction while the forces acting along the in-line direction are modelled using with a linear state space model [56].

Reduced Basis Methods

The idea of reduced basis methods is to replace a high dimensional full order problem with a low dimensional problem discretized on a reduced number of bases that consist of selected snapshots. Examples of such an approach on cylinders can be found in Akhtar [1] and Gallardo [17]. Here

the method is only introduced and since it is the method used through this thesis it will be deeply discussed in the following chapters.

Chapter 2

Flow past a circular cylinder: Theory

2.1 Flow around a circular cylinder

In this chapter we will give more details about the physical problem that we are considering and which will be studied later from reduced order modelling pointview. The problem which is flow past a circular symmetric cylinder is considered as a fluid structure interaction problem (FSI). We will present some theoretical aspects about the problem together with some results from experimental data and simulations. The description of problem is that we have a flow around a stationary cylinder or instead if we have a cylinder that moves in a fluid, in our case we consider the first option where we have water as fluid. In general what happens then is that a region of disturbed flow will be formed around the cylinder. The extent of the disturbed flow region is largely dependent on the shape, orientation, size of the body and the velocity and viscosity of the fluid. Reader can refer to [65, 66, 35]

2.1.1 Forces on a cylinder

Whenever an object is placed in a moving fluid (or moves through a stationary fluid) it will experience a force in the direction of the motion of the fluid relative to the object (drag force D) and it may experience a force normal to the flow direction (lift force L). Total drag force is the sum of projected tangential and normal forces at the surface of the body. Drag due to tangential stresses is called friction drag, skin friction drag, or viscous drag and drag due to normal stress is called form or pressure drag. It worths noting that pressure drag is an important contributor to total drag and often it is dominant in case of bluff bodies. It is defined by the following expression:

$$D = C_D \left(\frac{\rho V^2}{2} \right) A$$

Where A is the projected area normal to the flow direction and ρ is the density of the fluid This equation defines the drag coefficient C_D . Which generally depends on the Reynolds number. The drag coefficient for a circular cylinder is shown in 2.1. The different flow regimes are shown in figure 2.2. For cases of low Reynolds numbers (laminar flows), we don't have separation space, as the Reynolds number further increase, the flow will tend to separate. The separation takes place in a periodic way, forming the so called Von-Karman vortices. An increase in Reynolds number will result in a fully separated turbulent flow.

The Lift force L is a force normal to the flow direction. This force may be expressed as:

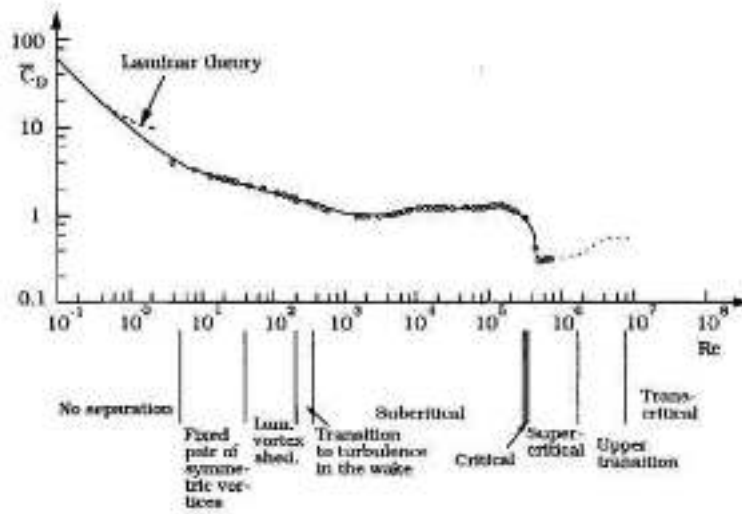


FIGURE 2.1: Drag coefficient for a smooth circular cylinder as a function of the Reynolds number, experimental data by Wieselsberger and Schewe [58]

$$L = C_L \left(\frac{\rho V^2}{2} \right) A$$

with C_L is the lift coefficient. This lift force is caused by the normal forces at the surface of the body

2.2 Strouhal number

The Strouhal number is a dimensionless number describing oscillating flow behavior. The parameter is named after Vincent Strouhal [57], a Czech physicist who first measured in 1878 the frequency of audible tone produced by wires and rods whirled through the air. The dimensionless parameter is:

$$St = \frac{fD}{U} \quad (2.1)$$

where f is the frequency of vortex shedding, D is the characteristic length (in our case the diameter of the cylinder) and U is the velocity of the fluid flow at the inlet. The variation of St in terms of Re depends on the regime of the flow. In the laminar periodic regime the relationship is not linear [31]. St - Re relationship can be seen in 2.3

Roshko [46] repeated the experiments made by Strouhal (1858) of shedding frequencies and in a large low-turbulence wind tunnel using hot-wire signals, and suggested the following ranges: (i) Stable range $40 < Re < 150$, regular velocity fluctuations and rising St (ii) Unstable range $150 < Re < 300$, irregular bursts in velocity fluctuations, St unstable (iii) Irregular range $Re > 300$, irregular and periodic, St is constant.

For the turbulent regime Roshko's (1953) hot-wire measurements shown that above the value of $Re = 3.5 \times 10^6$ a strong spectral peak appears, well above the turbulence level. This is shown in 2.4. So for a rigid and fixed circular cylinder the Strouhal number, over a certain range of the Reynolds







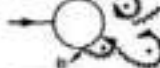
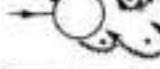

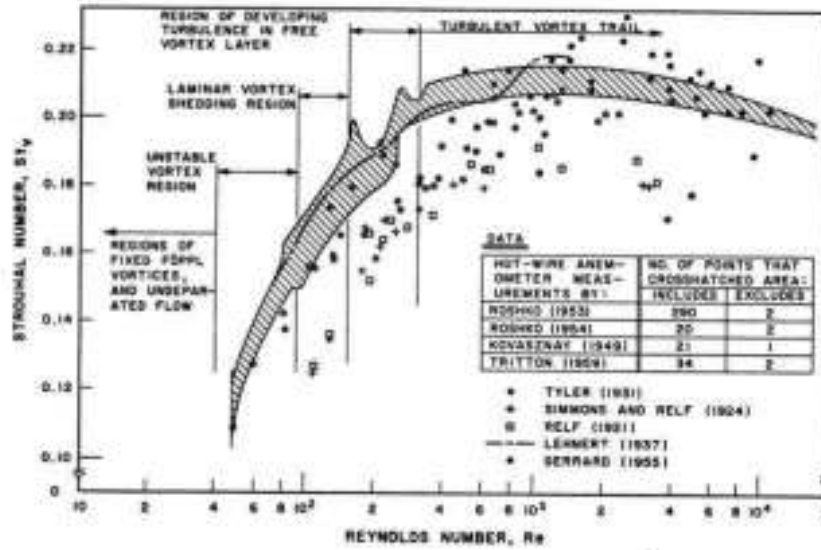
a)		No separation. Creeping flow	$Re < 5$
b)		A fixed pair of symmetric vortices	$5 < Re < 40$
c)		Laminar vortex street	$40 < Re < 300$
d)		Transition to turbulence in the wake	$300 < Re < 3000$
e)		Wake completely turbulent. A: Laminar boundary layer separation	$300 < Re < 3 \times 10^3$ Subcritical
f)		A: Laminar boundary layer separation B: Turbulent boundary layer separation, but boundary layer laminar	$3 \times 10^3 < Re < 3.5 \times 10^5$ Critical (Lower transition)
g)		B: Turbulent boundary layer separation; the boundary layer partly laminar partly turbulent	$3.5 \times 10^5 < Re < 1.5 \times 10^6$ Supercritical
h)		C: Boundary layer com- pletely turbulent at one side	$1.5 \times 10^6 < Re < 4 \times 10^6$ Upper transition
i)		C: Boundary layer com- pletely turbulent at two sides	$4 \times 10^6 < Re$ Transcritical

FIGURE 2.2: Regimes of flow around a smooth circular cylinder in steady current [58]

FIGURE 2.3: Change of St in terms of Re [31]

number, assumes a constant value approximately equal to 0.2 which can be seen from 2.4.

2.3 Vortex-induced vibration

Vortex-induced vibration (VIV) occurs when shedding vortices (a von Kármán vortex street) exert oscillatory forces on a cylinder in the direction perpendicular to both the flow and the structure [39]. If the structure is not fixed it begins to oscillate due to these forces. As previously explained, for a fixed cylinder the vortex-shedding frequency is related to the non dimensional Strouhal number and as we have mentioned in the range of Reynolds numbers from 300 to 3×10^5 we have a constant value for Strouhal number that is 0.2. When we consider cylinders which are free to vibrate then we observe a lock-in regime where the frequency of vibration of the cylinder will be locked to the natural frequency of the structure for some period before that it comes back to follow Strouhal relationship. So for low flow speeds, the vortex-shedding frequency f will be the same as that of a fixed cylinder. This frequency is fixed by the Strouhal number and then increasing the flow speed the shedding frequency will go closer to the natural frequency of the structure and so the vortex shedding frequency is no more following the Strouhal relationship instead the shedding frequency will be locked-in with the frequency of vibration of the cylinder. If the vortex-shedding frequency is close to the natural frequency of the cylinder f_0 ; as is often the case, large body motions are observed within the lock-in regime (the structure undergoes near-resonance vibration). Now we will introduce some variables which will be used in this thesis. With D we call the outer diameter of a circular cylinder, L is the length of cylinder, U is the free stream velocity of the flow and the fluid density is defined by ρ . In addition there are a number of dimensionless parameters. The reduced velocity is defined as $U^* = \frac{U}{f_0 D}$ where f_0 is the natural frequency of the cylinder. The mass

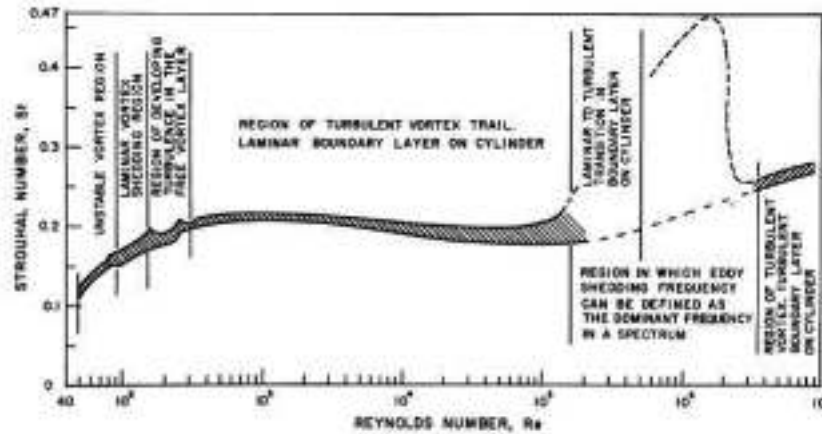


FIGURE 2.4: St trend in terms of Re - Transitional-Turbulent regime [31]

ratio m^* is defined as $m^* = \frac{m}{m_d}$ where m_d is the displaced mass defined by $m_d = \pi \rho D^2 L / 4$. Different phenomena are seen in structures with high and low structure-fluid mass-ratios m^* . For system with high m^* , the vortex shedding frequency is entrained by the structural frequency. For systems with low m^* , it is the fluid oscillation which sets the frequency and the entrainment frequency instead tends towards the shedding frequency f_v . The normalized damping is defined as $\zeta = c / 2 \sqrt{k(m + m_A)}$ where c is the system damping and m_A is the added mass given by $m_A = C_A \times m_d$. The coefficient C_A is the potential added-mass coefficient, for a circular cylinder, it can be considered equal to 1 [27]. The mass damping parameter $m^* \zeta$ express the ratio of the damping force to the excitation force. This parameter, which is proportional to the often used Scruton number ($S_c = \pi / 2 (m^* \zeta)$) [52], has a strongly dependence on amplitude of the response during lock-in and the band of fluid velocity over which the lock-in phenomenon exists. As the reduced damping parameter increases, lock-in becomes characterized by a decreasing peak structural amplitude and occurs over a decreasing band of velocities. Finally in the graphical representation of the oscillation amplitude and frequency are made using two dimensionless values, respectively the amplitude ratio $A^* = \frac{A}{D}$ where A is the amplitude response of the cylinder and the frequency ratio $f^* = \frac{f}{f_0}$ where f is the oscillation frequency.

2.4 Dynamics of cylinders

Numerous experiments were conducted by Khalak and Williamson (discussed in [25];[27]) which analyzed the effects of the variation of the mass ratio m^* and the normalized damping ζ on the amplitude ratio and frequency ratio of the response.

The experiments were conducted in water and were characterized by having very low mass ratio m^* and very low normalized damping ratio ζ . The added mass m_A is taken to be equal to the displaced mass of the

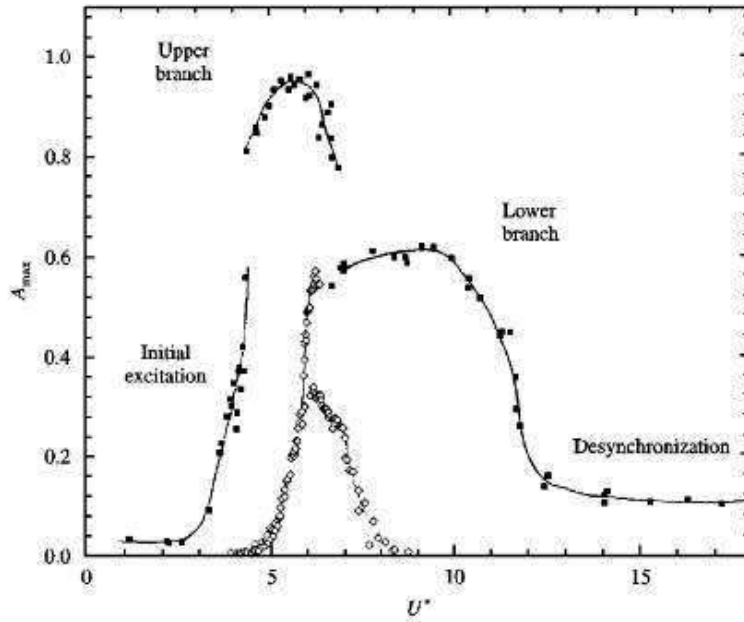


FIGURE 2.5: Maximum response amplitudes A_{max} as functions of the reduced velocity U^* for $m^* = 2.4$ (■) Khalak and Williamson and for Feng $m^* = 248$ (◇) [26]

fluid (the potential added mass coefficient C_A is assumed to have a value of unity). The combined mass-damping parameter $m^*\zeta$ has a value of 0.013, a value smaller than the data presented by Feng [14] by a factor of roughly 30. The response of the cylinder are characterized by four regimes: i) the initial excitation regime, ii) the "upper" branch of response (very high amplitude response), iii) the "lower" branch of response (moderate amplitude response), iv) the desynchronization regime. As we can be seen in 2.5 hysteresis results from moving between these branches and the jump between the branches can be interpreted as a change in the vortex-shedding mode. Note that the reduced velocity is formed using the natural frequency in still water f_0 , $U^* = \frac{U}{f_0 D}$. In the same figure we can see the data from Feng [14] also, which is obtained for the mass-damping parameter equal to $m^*\zeta = 0.36$. For lower values of mass damping, we can observe a substantial increase in both amplitude and range of the response. The mass ratio m^* and the normalized damping ζ are found to independently affect the response of the system. By maintaining the value of $m^*\zeta$ constant, the value of m^* was independently adjusted. Lower values of m^* are manifested in the form of higher response amplitudes and a larger range of response in the lower resonance branch. However, changes to m^* do not significantly alter the characteristics of the upper branch. The level of maximum excitation in the upper branch is found to be well characterized by the combined mass-damping parameter $m^*\zeta$ [16].

In a subsequent paper Khalak and Williamson [27] show that as the normalized velocity is increased, the transition from the initial excitation region to the upper branch is hysteretic (H). The transition from the upper branch to the lower branch also involves a jump, but is followed by intermittent switching (I). This intermittence is clearly seen in the instantaneous phase

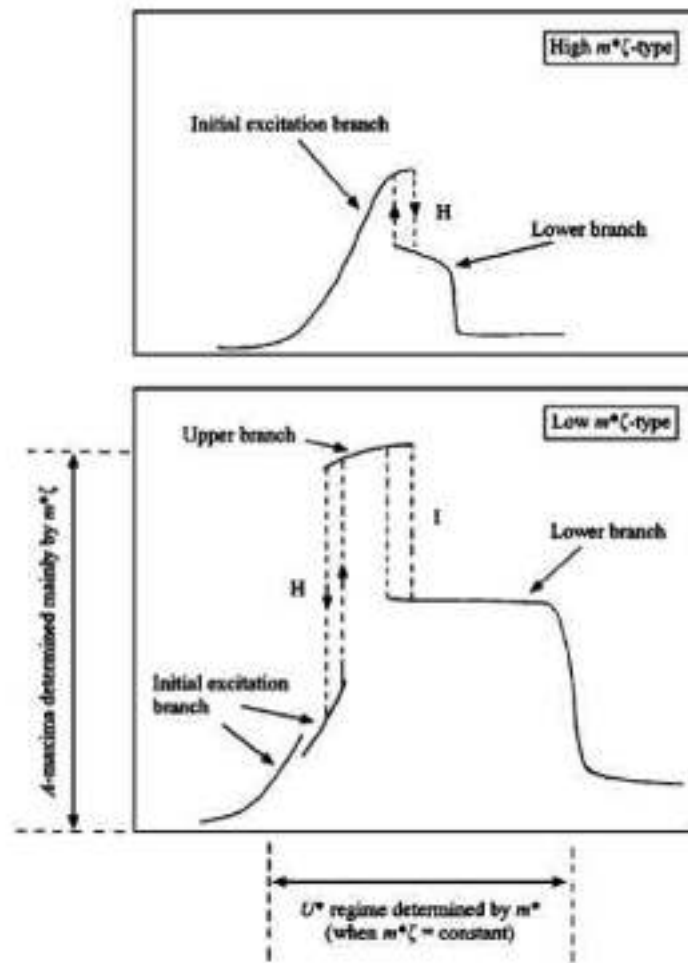


FIGURE 2.6: Schematic plot of the differences between high- $m^*\zeta$ and low- $m^*\zeta$ amplitude response [27]

measurements between the lift force and the displacement in the transition region. Both of the transitions are associated with jumps in response amplitude and frequency, but only the transition from the upper to the lower branch is associated with a 180 degree jump in the phase angle. The two different types of amplitude response: high- $m^*\zeta$ and low- $m^*\zeta$ was presented in 2.6 where we can see the two mode of transition hysteric (H) or intermittently switching (I).

The most interesting result is that, in the synchronization regime, the frequency of cylinder oscillation is significantly higher than the structural natural frequency. In other word in the synchronization regime the frequency ratio f^* is greater than one. From figure 2.7 we can clearly observe the apparently "non classical" behavior of f^* , through the synchronization regime, resulting from low mass ratio system. The lock-in is defined as the matching of the frequency of the periodic wake vortex mode with the cylinder oscillation frequency. Therefore the departure of f^* from unity is not what we would expect from classical lock-in behavior. Although it is convenient to define synchronization as the matching (or more correctly, near matching) of the frequency of the periodic wake vortex mode with the

body oscillation frequency $f^* \approx 1$.

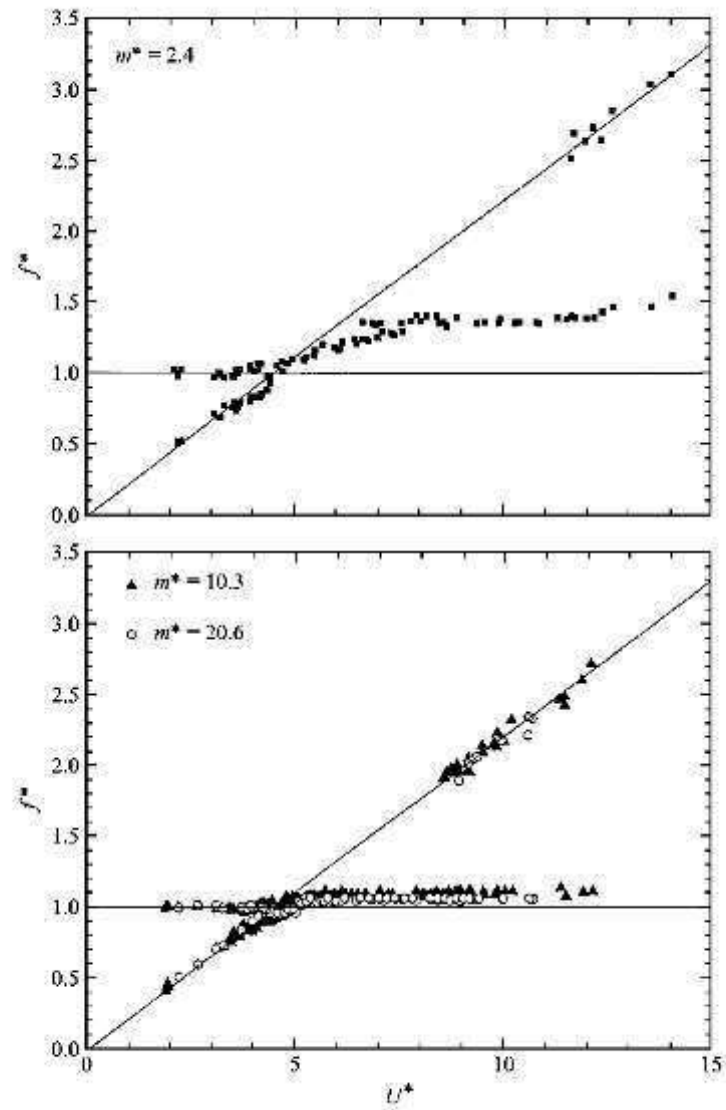


FIGURE 2.7: Frequency response for a range of mass ratios, m^* , through the synchronization regime [27]

Chapter 3

Flow past a circular cylinder: Simulations and Results

In this chapter we will introduce the simulation and the results which we have obtained in our work for the problem of the flow past around a circular cylinder. We will start by the providing an idea about the problem setup and then we go into more details regarding the analysis of the results.

3.1 Problem setup

3.1.1 Computational domain

Our case contains a cylinder having its center placed at the origin of our reference system. The region used for the analysis of the fluid flow passing the cylinder extends $5D$ forward (opposite direction of the flow) and $15D$ backwards, laterally it extends $10D$ in every direction (up and down), see figure 3.1 Hence our goal is to investigate the fluid flow around a cylinder, three regimes will be analyzed, but maintaining one single domain throughout the entire process. This choice can be not very convenient especially when dealing with low Reynolds flows, which clearly will have a symmetrical flow respect to the horizontal centerline, in those cases a smaller domain (upper or lower half) with a symmetry condition could be more appropriate, halving the number of cells to be taken into account. [25]

3.1.2 Fluid properties

Density and kinematic viscosity of the fluid (water) used in the computation are obtained using regression equations, given by [53], where secondary required water properties are indicated by [20].

3.1.3 Methodology

The OpenFOAM-v3.0+ [24] code was used for numerical simulations. The predictor-corrector PISO algorithm [23] implemented on pisoFOAM standard solver was employed. Given the unsteady flow generated by the vortex shedding it is necessary to use this transient incompressible solver. For the turbulent cases unsteady Reynolds-Averaged Navier-Stokes equations (URANS) modelling based on the finite-volume method (FVM) [62] are used. For the PISO loop two corrector iterations and no non-orthogonal corrections were set. Regarding time integration, first order Euler implicit

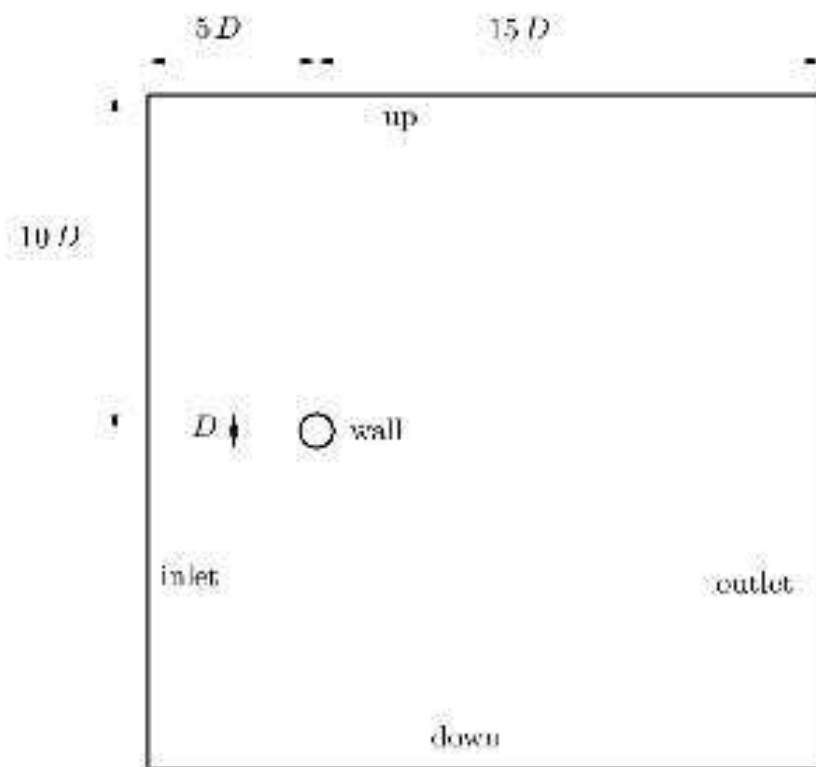


FIGURE 3.1: Computational domain

method was applied. Linear (CDS) and linearupwind (SOUDS) spatial discretization schemes were set as gradient and divergence terms, respectively. Preconditioned conjugate gradient (PCG) with diagonal incomplete Cholesky (DIC) was used for solving linear systems of pressure term with tolerance of 10^{-6} , preconditioned biconjugate gradient (PBiCG) with diagonal incomplete LU (DILU) were used for the pressure term linear system instead, setting the tolerance to 10^{-7} . For low Reynolds number cases, the $k - \omega SST$ and Spalart-Allamaras turbulence models were chosen [36], while high Reynolds cases were treated using $k - \omega$ and Spalart-Allamaras turbulence models [37], combined with wall-functions.

3.1.4 Boundary conditions

Velocity

For velocity, we have two different boundary settings, the first is just a Free-stream velocity is defined at the inlet boundary where a uniform velocity profile has been used. The outlet boundary is a patch where the fully developed fluid flow can pass through without variations ($\frac{\partial U}{\partial n} = 0$), known as zero-gradient boundary condition or Neumann boundary conditions, where the normal component of the velocity is zero. The cylinder is characterized by a wall-type boundary condition, where no-slip condition is applied. While second kind of boundary conditions for velocity has just one difference which is that the field is chosen to be varying with time so for example at time zero we will have a uniform field $\mathbf{U}_0^1 = (U_0^1, 0, 0)$ and then we will change linearly in a period of 10 seconds to another velocity $\mathbf{U}_0^2 = (U_0^2, 0, 0)$ (by either increasing or decreasing ramp depending on the new value of magnitude of the velocity) and afterwards the velocity will be fixed to that new field \mathbf{U}_0^2

Pressure

For what concerns the pressure boundary conditions, zero gradient is applied on every boundary patch and at the outlet we have zero pressure. The pressure at the reference point of the domain was set to zero.

3.2 VIV analysis

In this section we will concern ourselves with the case of low Re range (2000-13000) and we will compare our results with the one obtained from Khalak and Williamson [25] and with other numerical simulations results in 2D. We will go through the definition of the equation of motion and then to the main case analysis where we will mention the values of all parameters which were set for the simulations. After that we will discuss the data sampling and analysis, then we introduce our results and how we analyze them with some postprocessing codes.

Equation of motion

We have a structure system which is the one - degree of freedom (dof) dynamical system that can be modeled as the two dimensional cylinder with mass m supported by a spring with a stiffness k and a damper c , as show in 3.2. So we can write the following equation of motion that describes the

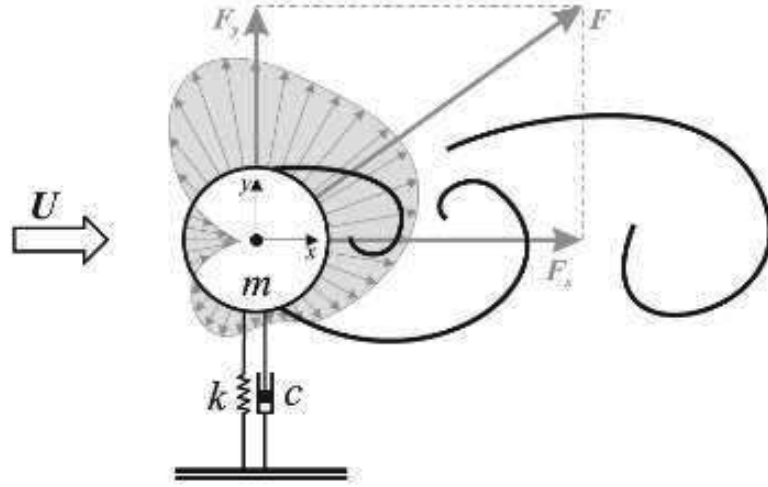


FIGURE 3.2: Harmonic oscillator model representing an elastically mounted cylinder

dynamics of the problem for this mass-spring-damper system:

$$m\ddot{y} + c\dot{y} + ky = F_y(t) \quad (3.1)$$

where $F_y(t)$ is the time dependent fluid force acting on the cylinder body in the cross flow direction. Which is obtained by integrating the pressure and viscous friction on the cylinder surface resulting from the resolution of the Navier-Stokes equation. The terms y , \dot{y} and \ddot{y} are respectively the displacement, velocity and acceleration of the body.

Now the natural frequency of the system is determined by

$$f_0 = \frac{1}{2\pi} \sqrt{\frac{k}{m}} \quad (3.2)$$

The structural damping is generally expressed by a damping ratio

$$\zeta = \frac{c}{2\sqrt{km}} \quad (3.3)$$

If the structural damping is kept sufficiently low, then the damped natural frequency $f_{0_d} = f_0 \sqrt{1 - \zeta^2}$ can be considered approximately equal to f_0 .

The fluctuating fluid force on the body can be expressed in terms of the lift coefficient C_L , where

$$C_L(t) = \frac{F_y(t)}{\frac{1}{2}\rho U^2 D} \quad (3.4)$$

3.2.1 Main case analysis

One main aim in our simulations is to recover similar results to the experimental benchmark which have been done by Khalak and Williamson [25]. So for this reason we have setup the same configuration of the experimental procedure, with the same mass ratio $m^* = 2.4$, mass-damping parameter of $m^*\zeta = 0.013$, while we have Reynolds number ranges from 2000 to 13000 so correspondingly the reduced velocity U^* will vary from 2 to 15.5. For the initial conditions, it should be stressed that in the experiments of Khalak, the velocity was being increased in steps, while for us we have done two different configurations, in the first one we start always with the cylinder in the zero position and from zero initial velocity and in the other configuration we consider the same thing that Khalak has carried out by doing steps in both directions up and down.

In Table 2.1, they are mentioned all the non dimensionalized parameters which are used in our simulations and the values of the parameters are shown in Table 2.2.

Initial conditions

Fluid properties

For the sake of having same reduced velocity or Reynolds number ratio of the one in Khalak and Williamson experiments, fluid density and kinematic viscosity have been set to 999.1026 kg/m^3 and $1.1386 \times 10^{-6} \text{ m}^2/\text{s}$ respectively.

Pressure

Boundary condition "zero gradient" has been applied on the boundaries of the domain and cylinder surface. Reference pressure has been set to 0.

Velocity

Free-stream velocity is defined at the inlet boundary, where two different kind of initial velocity fields have been used as we have already mentioned, which are either a uniform velocity profile or the velocity that results from another simulation at the final time. "InletOutlet" boundary condition has been applied on outlet boundary patch. This boundary conditions apply zero gradient if the flux (through the specified patch) is positive, otherwise, internal field value is applied. At top and bottom patches, zero gradient condition has been set. Concerning boundary condition on the cylinder, since it is a moving patch, "MovingWallVelocity" which a kind of boundary condition used with moving walls boundaries and in contrast to the fixed value boundary condition, velocity value is defined relative to the boundary it is applied to. has to be applied in order to ensure no-slip condition while moving.

Turbulence properties

Considering the $k - \omega SST$ we followed Menter (1994) [36] approach:

$$\omega_{wall} = \frac{60\nu}{\beta_1 y_1^2} \quad \omega_{farfield} = 10 \frac{U_\infty}{L}$$

$$k_{wall} = 0 \quad k_{farfield} = 0.1 \frac{U_\infty^2}{ReL}$$

Dynamic mesh settings

The spring parameters in OpenFoam are fixed in the 'dict' file named dynamicMeshDict inside the constant folder. In this file we have set the mass of the cylinder and also the damping c and the stiffness k . The value of the stiffness was found from the value of the frequency in the air

$$f_{0,a} = \frac{1}{2\pi} \sqrt{\frac{k}{m}}$$

While for the frequency in water it is given by

$$f_{0,w} = \frac{1}{2\pi} \sqrt{\frac{k}{m+m_A}}$$

Here m_A is the added mass that is given by $m_A = C_A m_d$ and so the reduced velocity in water will be given by $U_w^* = \frac{U}{f_{0,w} D}$

Data sampling

After doing the simulations, the data that are coming from them mainly they are the motion history of the cylinder (position of the center of mass of the cylinder) and the forces coefficients, for the motion history we used a script that extracts motion data directly from a log file, the "grep" function is used in order to extract the cylinder center of mass coordinates that are printed each timestep then the values which are extracted will be space delimited to two column data file that will be used for post processing in MATLAB.

For the forces coefficient data they will be calculated using OpenFOAM built in utility which is called forceCoeffs, the utility computes the coefficients by integrating and projecting pressure distribution on the cylinder patch, relative coefficients are then computed using user defined free-stream velocity and patch projected area in the dedicated dictionary file.

Data analysis

Now talking about the data analysis procedure we have used MATLAB code for processing the data that we have got as result of our simulations, so our code will read the two column data file that contains the times series and the y-coordinate of the center of mass of the cylinder and then we will compute the peaks of the time signal that describes the motion of the cylinder so that we can cut the transient part of the signal from an appropriate point notice that we will cut the transient part no matter how long it takes. Finally we will take the final developed regime and we will calculate the reduced amplitude which is the ratio between the maximum amplitude of vibration and the diameter of the cylinder and after that we take the final signal and we perform fast Fourier transform on it. So then we get the single-sided amplitude spectra of frequencies contained in the data and looking at the spectrum, we can see the first peak of the frequency and the second one if it exists (basically we set up a threshold of how to define the existence of that second peak). At the end we will have the frequency of vibration, dividing it by the natural frequency of the structure under water will give us the reduced frequency.

Since the PIMPLE algorithm (that we have used to simulate using OpenFOAM) uses variable timesteps, time series of the cylinder motion has to be interpolated in order to use FFT, the interpolation has been made in order to match the sampling frequency.

If we do the procedure for another different case (different Reynolds numbers or different reduced velocities) then we will plot the amplitude ratio A/D versus the reduced velocity and also the reduced frequency versus the amplitude ratio so that we can compare our results with the experimental results.

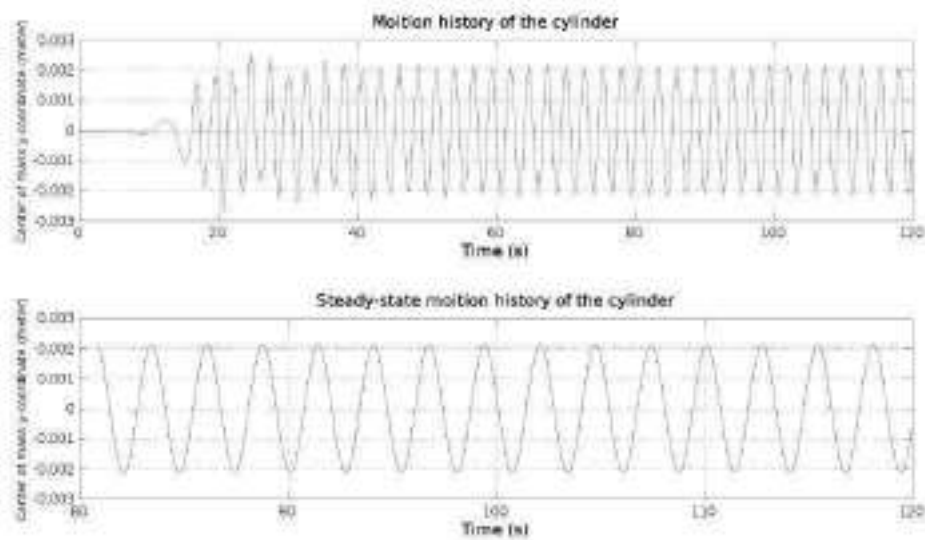
Analysis of results

In this section we will show and discuss the results of our simulations. First we can see in table 3.1 the results of the simulations which we have conducted. In our simulations, we were interested in assessing the cylinder vibrations under different stream velocities. A typical output of our simulation is presented in figure 3.3a. Where we have two plots, the top one is for the time history of the vertical displacement of a cylinder immersed in an horizontal flow of velocity of 0.0597 m/s . Such a velocity corresponds to Reynolds number equal to 2000, and the bottom plot is showing the final regime that was used later to perform the Fourier analysis. It can be seen from figure 3.3a that after an initial build up phase, the cylinder starts vibrating at non negligible amplitudes and eventually the motion settles to a final regime solution for which it takes in this case around 20 seconds. In figure 3.3b we can see the amplitude spectrum of the vertical displacement signal (the one which has been trimmed) and we can see that the frequency of vibration is manifested by the peak in figure 3.3b. In this case $Re=2000$, the frequency is about 0.381470 Hz which corresponds to Strouhal number of 0.24317 , so in this case the cylinder oscillates close to the theoretical vortex shedding frequency. Also, we can notice from figure 3.3a that the maximum amplitude of vibration is about 0.0021297 meters .

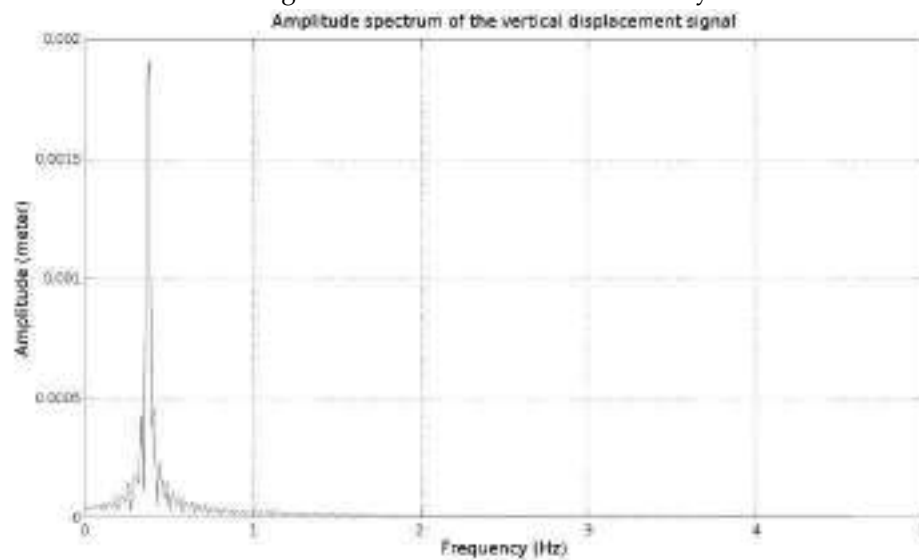
Now if we look on the same type of graphs but for the case of $Re = 3000$, see figures 3.4, we can see that in this case instead we have clearly two different peaks in the amplitude spectrum. The first one is located at frequency equal to 0.656128 Hz and by first we will refer to the dominant one, while the second peak is located at frequency of 0.488281 Hz . These two values correspond to Strouhal numbers 0.207505 and 0.278834 respectively, now recalling the natural frequency in water which is defined as

$$f_{0,w} = \frac{1}{2\pi} \sqrt{\frac{k}{m+m_A}}$$

where k is the stiffness of the spring, and m_A is the added mass given by $m_A = C_A \times m_d$. The coefficient C_A is the potential added-mass coefficient, for a circular cylinder, it can be considered equal to 1. In our case the natural frequency in water has a value of 0.659 Hz . Now we see that in this case the first peak occurs very closely to the natural frequency in water and the ratio between them is about 0.99 . While we can see that the second peak corresponds to Strouhal number which is very close to the theoretical vortex shedding one that is 0.22 . So it can be seen that the dominant peak



(A) The top plot represent the time history of a vertical displacement of a cylinder immersed in a horizontal stream with $Re=2000$. In the bottom plot we report the final regime solution used for Fourier analysis.



(B) Amplitude spectrum of the vertical displacement signal (see figure A) for a cylinder immersed in horizontal stream at $Re=2000$.

FIGURE 3.3: Results for a cylinder immersed in horizontal stream at $Re=2000$

corresponds to the natural frequency while the second one corresponds to the vortex shedding frequency which is determined by Strouhal law. So the fact is that a second frequency close to the structural natural frequency is appearing which suggests that we are approaching the lock-in regime.

Moving to the case where $Re = 9000$, see figure 3.5 where it is depicted the amplitude spectrum for the final regime signal. We can see this time that we have just one peak at frequency of $0.86975Hz$ which gives a ratio of 1.3 to the natural frequency of water while the theoretical vortex shedding frequency is about $1.5531Hz$. This tells us that we are completely in the lock-in regime.

Increasing the velocity of the stream in the inlet more by reaching a value give Reynolds number equal to 10000, see figure 3.6 for the results. It is easily observed in this case that there are two peaks and the first one takes place at frequency of $0.86975Hz$ and the second one happens at $1.55640Hz$, these values give Strouhal number of 0.11089 and 0.19843 respectively. This time we see that the dominant (first) peak is closer to the natural frequency of the cylinder in water while the new frequency is close to the theoretical vortex shedding frequency — is indicating that we are about to abandon the lock-in regime —.

If we look further on higher inlet velocities by considering the case of $Re = 13000$, see figure 3.7, we see that in this case we have one frequency in our amplitude spectrum that occurs at $2.0370Hz$ which is close to the value of vortex shedding frequency calculate by Strouhal law that is $2.2433Hz$. So this gives a sign that the cylinder is not anymore in the lock-in regime, and the vibrations follow Strouhal law.

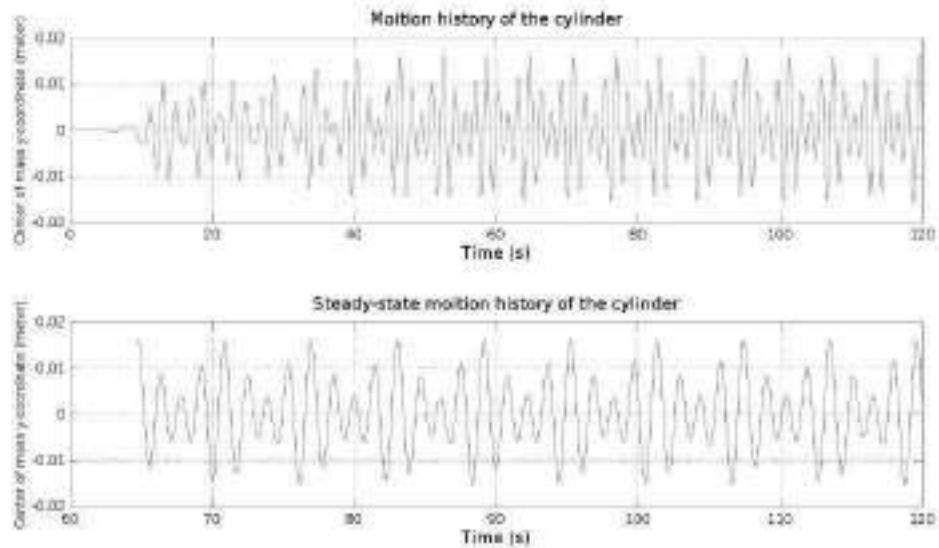
The procedure that we have discussed for five different inlet velocities above can be extended to more Reynolds number. Results for different cases are reported in the appendix A. At the end of this procedure we can have a better understanding of the problem by looking on how the frequency ratio and the amplitude ratio change with respect to the reduced velocity. This is depicted in figures 3.9 and 3.8

Now we can reproduce the similar figures to 2.5 and 2.7. Figure 3.9 shows the reduced amplitude versus the reduced velocity and 3.8 shows the reduced frequency versus the reduced velocity. We can see that we have two frequencies or two modes of vibration and it is obvious that we have captured the lock-in phenomena that happens between the values of $U_1^* = 4.7596$ and $U_1^* = 13.779$

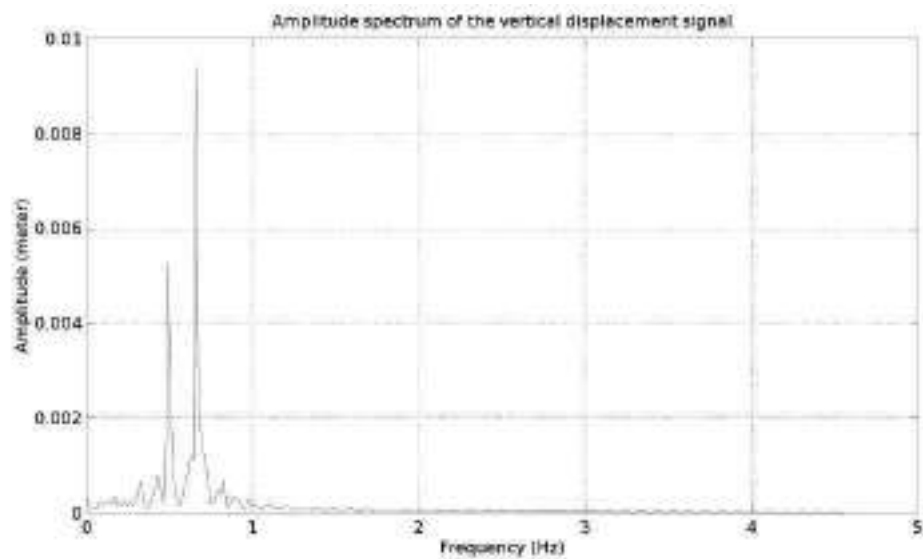
Now talking about the oscillation frequency ratio which can be seen in figure 3.8, we have plotted in grey a line which corresponds to $f_{red} = f_0$ which represents the lock-in region and the oblique line represents the Strouhal law line, in the figure 3.8 the first dot in red represent the first peak dominant frequency and the green circle represents the second peak if it exists, for some values in the low range of reduced velocities we got two frequencies, in particular for $U^* < 4.9975$ and this just happens before the jump from the initial excitation branch to the upper branch as observed in Khalak experiments. Afterwards from $U^* = 5.0570$ to $U^* = 11.542$ we have

TABLE 3.1: Results summary

Reynolds Number	U_w^*	A/d	f_1/f_0	f_2/f_0
2000	2.37978	0.0558988	0.57869	-
2500	2.97472	0.251811	0.624985	0.995346
3000	3.56967	0.42556	0.740723	0.995346
3500	4.16461	0.341897	0.821739	-
3750	4.46209	0.459802	0.844887	-
3850	4.58108	0.725385	0.914329	-
3900	4.64057	0.752657	0.925903	-
3950	4.70006	0.780893	0.914329	1.00692
4000	4.75956	0.804915	0.914329	1.03007
4100	4.87855	0.83023	0.868034	0.972198
4150	4.93804	0.84253	0.879608	0.960625
4175	4.96779	0.84808	0.983772	-
4200	4.99754	0.700949	0.972198	-
4250	5.05703	0.616374	1.08794	-
4300	5.11653	0.621874	1.08794	-
4400	5.23552	0.698402	1.09951	-
4500	5.3545	0.661163	1.11687	-
4600	5.47349	0.617762	1.15738	-
4700	5.59248	0.546918	1.24997	-
4800	5.71147	0.541937	1.27312	-
4900	5.83046	0.525674	1.29626	-
5000	5.94945	0.503883	1.31941	-
5100	6.06844	0.485735	1.36571	-
5200	6.18743	0.488948	1.36571	-
5300	6.30642	0.494053	1.36571	-
5400	6.42541	0.49767	1.36571	-
5500	6.54439	0.500026	1.36571	-
5600	6.66338	0.499136	1.36571	-
5700	6.78237	0.501544	1.37728	-
5800	6.90136	0.495723	1.37728	-
5900	7.02035	0.488683	1.37728	-
6000	7.13934	0.484925	1.37728	-
6100	7.25833	0.481357	1.38885	-
6200	7.37732	0.480974	1.37728	-
6300	7.49631	0.480813	1.37728	-
6400	7.6153	0.482605	1.37728	-
6500	7.73428	0.486099	1.36571	-
6600	7.85327	0.49424	1.36571	-
6700	7.97226	0.50862	1.35413	-
6800	8.09125	0.525933	1.35413	-
6900	8.21024	0.547963	1.34256	-
7000	8.32923	0.573628	1.33677	-
7100	8.44822	0.593369	1.34256	-
7500	8.92417	0.595673	1.31941	-
8000	9.51912	0.587713	1.31363	-
8500	10.1141	0.58944	1.31363	-
9000	10.709	0.578024	1.31941	-
9500	11.304	0.544042	1.33099	-
9600	11.4229	0.536956	1.34256	-
9650	11.4824	0.532843	1.33099	-
9675	11.5122	0.530938	1.34256	-
9685	11.5241	0.532604	1.33099	-
9700	11.5419	0.372586	2.24532	-
9800	11.6609	0.31307	2.28582	-
10000	11.8989	0.261934	1.31941	2.36105
10500	12.4938	0.23389	1.33099	2.49994
11000	13.0888	0.215882	1.35413	2.62725
11200	13.3268	0.209515	1.35413	2.68512
11500	13.6837	0.127729	1.38885	2.77771
11510	13.6956	0.185934	1.38885	2.77771
11525	13.7135	0.178656	1.37728	2.76614
11530	13.7194	0.129536	1.37728	2.76614
11535	13.7254	0.128872	1.38885	2.77771
11540	13.7313	0.177487	1.38885	2.76614
11545	13.7373	0.175335	1.38885	2.77771
11550	13.7432	0.129032	1.38885	2.77771
11575	13.773	0.172064	1.38885	2.77771
11580	13.7789	0.173136	1.38885	2.77771
11583	13.7825	0.130825	2.77771	-
11585	13.7849	0.130959	1.38885	2.77771
11600	13.8027	0.0563288	2.76614	-
11620	13.8265	0.165984	1.39175	2.78639
11630	13.8384	0.164319	1.39464	2.78928
11640	13.8503	0.162661	1.39464	2.78928
11650	13.8622	0.0505754	2.77482	-
11700	13.9217	0.0511273	2.78928	-
12000	14.2787	0.0495084	2.85873	-
12500	14.8736	0.0495077	2.97446	-
13000	15.4686	0.0494982	3.0902	-



(A) The top plot represent the time history of a vertical displacement of a cylinder immersed in a horizontal stream with $Re=3000$. In the bottom plot we report the final regime solution used for Fourier analysis.



(B) Amplitude spectrum of the vertical displacement signal (see figure A) for a cylinder immersed in horizontal stream at $Re=3000$.

FIGURE 3.4: Results for a cylinder immersed in horizontal stream at $Re=3000$

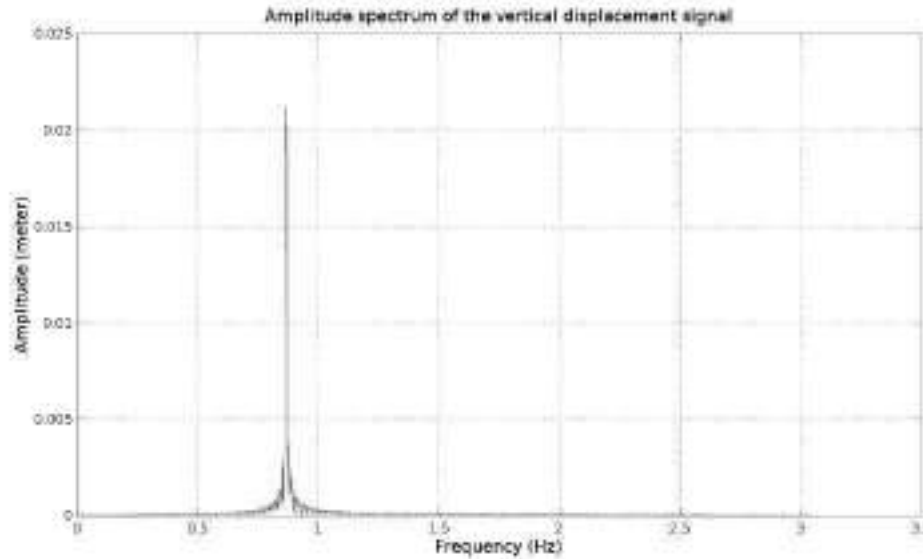
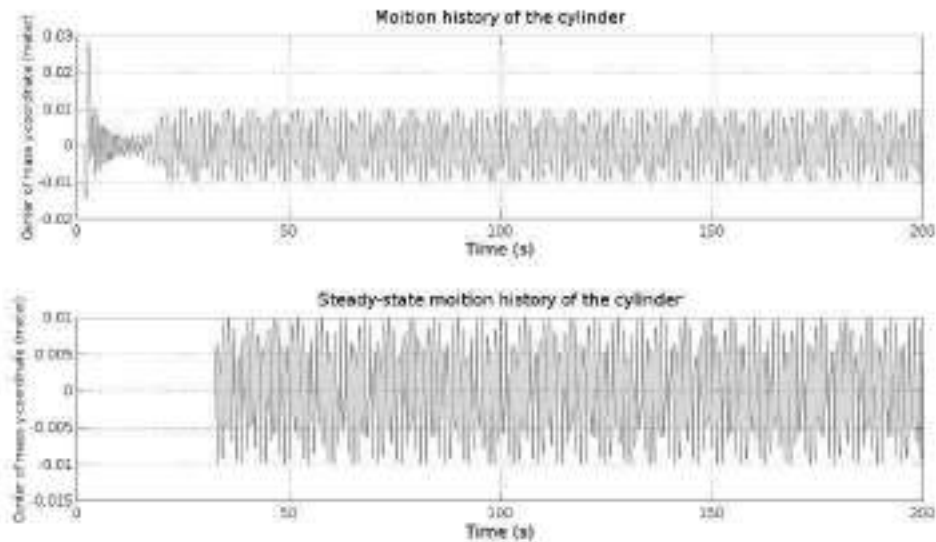


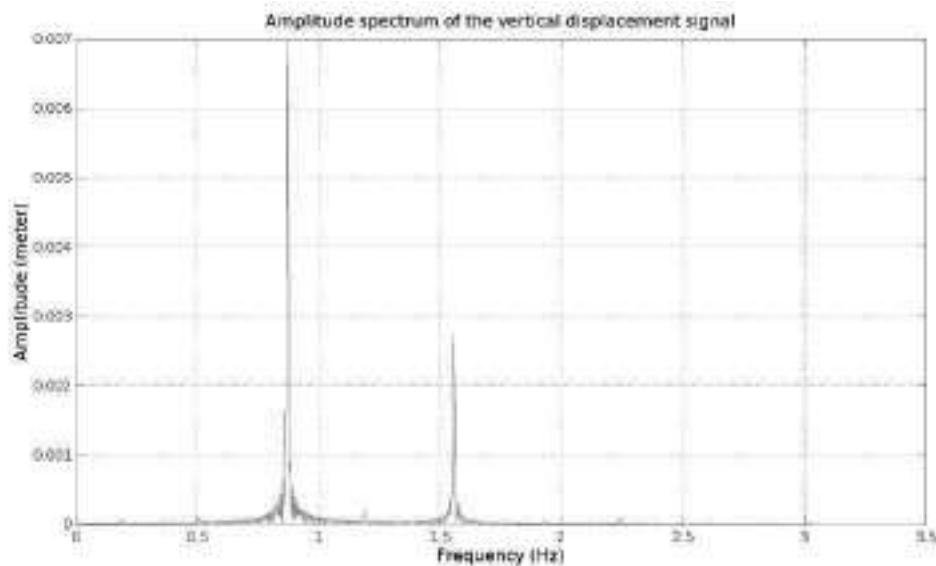
FIGURE 3.5: Amplitude spectrum of the vertical displacement signal (see figure A.9a) for a cylinder immersed in horizontal stream at $Re=9000$.

just one peak which corresponds to the natural frequency of the structure and in that period we observe the lock in regime. Qualitatively speaking we can say that we have captured the main features of the relation between the frequency of oscillations of the cylinder and the inlet velocities. Basically, we have five different regions, in the first we observe the vortex shedding frequency that can be computed theoretically, and then we have a region of two frequencies of vibrations one still is the vortex shedding one and the other is close to the natural frequency of the cylinder in water. Afterwards we have pure lock-in regime where the oscillations are characterized by the structural frequency, then we start observing second peak that corresponds to the vortex shedding frequency. Finally, the cylinder comes back to vibrate at only one frequency equal to the vortex shedding frequency. Talking about the accuracy of our results compared to Khalak's data, we see that we have not captured the second peak for inlet velocities near of $U^* = 2$ while inside the lock-in region we obtained much accurate results. Some error is observed in the region correspond to higher Reynolds number from 9000 – 13000 where we have the relation of Strouhal being followed.

For the amplitude we notice that the maximum value from our simulations was 0.84808 while in Khalak experiments it was a little bit higher. We have been able to reproduce the same shape with the jumps from the initial excitation branch to the upper branch and then the jump down to the lower branch. The highest level of vibration occurs at a reduced velocity of $U^* = 4.9678$. In the beginning we observe that the reduced amplitude increases as we increase U^* till we reach the mentioned value. Above this value a drop happens till $U^* = 7.4963$ in which we have amplitude ratio of 0.48081 that is slightly lower from the experimental value. We also can see from figure 3.9 that the region of velocities for which we have observed the highest value of vibration amplitude is narrower in our results than in the experimental results from Khalak. This might be justified by the fact that in practice we have larger band of velocities for which the cylinder will stay in



(A) The top plot represent the time history of a vertical displacement of a cylinder immersed in a horizontal stream with $Re=10000$. In the bottom plot we report the final regime solution used for Fourier analysis.



(B) Amplitude spectrum of the vertical displacement signal (see figure A) for a cylinder immersed in horizontal stream at $Re=10000$.

FIGURE 3.6: Results for a cylinder immersed in horizontal stream at $Re=10000$

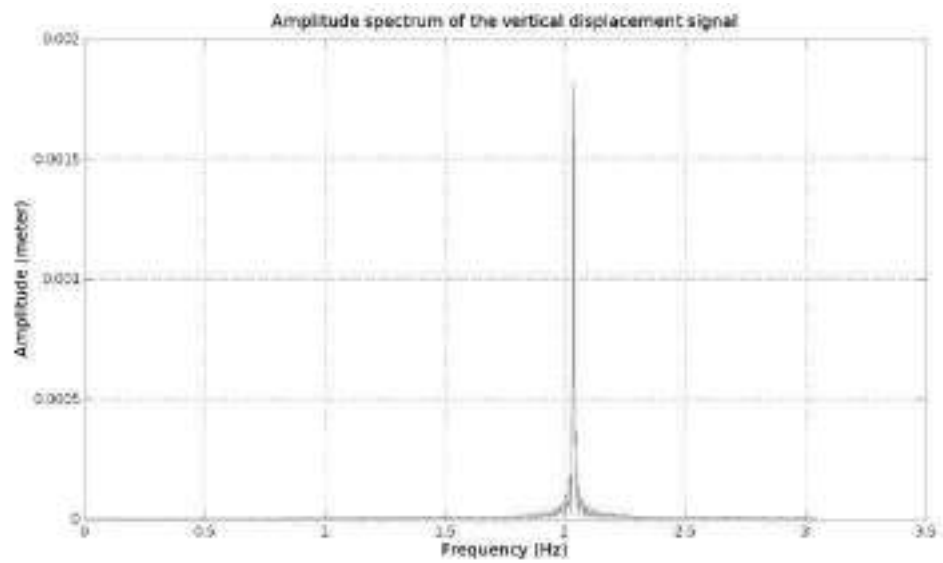


FIGURE 3.7: Amplitude spectrum of the vertical displacement signal (see figure A.27a) for a cylinder immersed in horizontal stream at $Re=13000$.

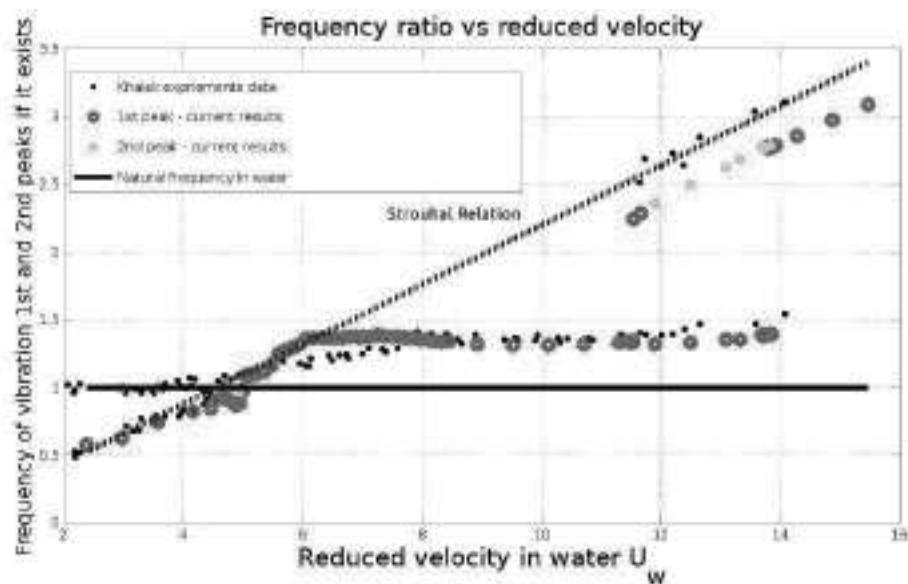


FIGURE 3.8: Reduced frequency in water which is defined as $f_w^* = \frac{f}{f_{0,w}}$ versus the reduced velocity in water defined

$$\text{as } U_w^* = \frac{U}{f_{0,w}D}$$

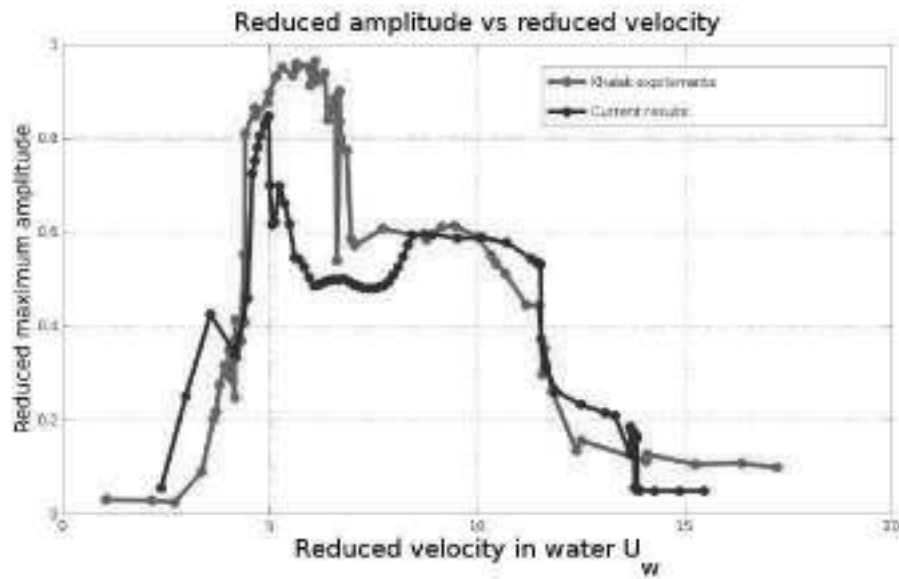


FIGURE 3.9: Reduced amplitude (which is defined as maximum amplitude of vibration divided by the diameter of the cylinder) versus the reduced velocity in water defined as $U_w^* = \frac{U}{f_{0,w}D}$, we have here a comparison between our results and Khalak experiments

the synchronization mode and this has to do with the three dimensionality of the experiments.

Chapter 4

Reduced order methods

4.1 Parameterized Variational Problems

In this section we will give a quick overview about parameterized variational differential equations, where details are available in many resources like [41, 47, 15, 7, 40, 11, 45, 4, 48, 21, 12, 34, 10, 8, 18, 30, 6] first we assume that we have $\Omega \in \mathbb{R}^d$ suitably regular domain with boundary $\partial\Omega$, where $d = 1, 2$ or 3 its spatial dimension, in the formulation of the parameterized variational problem we will deal with both scalar and vector fields so field variables $w : \Omega \mapsto \mathbb{R}_v^d$ may be considered, where d_v is the dimension of the field variable so for scalar fields we have it equal to one and for vector fields it will be same as d , also we call the parts of the boundary where Dirichlet boundary conditions are imposed as $\Gamma_i^D, 1 \leq i \leq d_v$

Now we introduce the scalar field spaces $\mathbb{V}_i, 1 \leq i \leq d_v$,

$\mathbb{V}_i = \mathbb{V}_i(\Omega) = \{v \in H^1(\Omega), v|_{\Gamma_i^D} = 0\}, 1 \leq i \leq d_v$. In general $H_0^1(\Omega) \subset \mathbb{V}(\Omega) \subset H^1(\Omega)$, and so the space where our vector valued field variable will lie would be the following Cartesian vector product $\mathbb{V} = V_1 \times \dots \times V_{d_v}$, an element of \mathbb{V} will be denoted as $w = (w_1, \dots, w_{d_v})$, we equip \mathbb{V} with an inner product $(w, v)_{\mathbb{V}}$ and the induced norm is $\|w\|_{\mathbb{V}} = \sqrt{(w, w)_{\mathbb{V}}}, \forall w \in \mathbb{V}$, and we can see that the space \mathbb{V} is a Hilbert space since any inner product which induces a norm equivalent to the $(H^1(\Omega))_v^d$ norm is admissible. At last, we introduced the closed parameter domain $\mathbb{P} \in \mathbb{R}^P$, a typical parameter point or vector will be denoted as $\mu = (\mu_{[1]}, \mu_{[2]}, \dots, \mu_{[p]})$, we may thus define our parametric field variable as $u = (u_{[1]}, u_{[2]}, \dots, u_{[d_v]}) : P \mapsto \mathbb{V}$ which denotes the field for parameter value $u(\mu)$.

4.1.1 Parametric Weak Formulation

Now in this part we will introduce a general stationary problem where we are given parameterized linear forms $f : \mathbb{V} \times P \mapsto \mathbb{R}$ and $l : \mathbb{V} \times P \mapsto \mathbb{R}$, where the linearity is with respect to the first variable, and a parameterized bilinear form $a : \mathbb{V} \times \mathbb{V} \times P \mapsto \mathbb{R}$, where the bilinearity is with respect to the first two variables. The abstract formulation reads: given $\mu \in P$, we seek $u(\mu) \in \mathbb{V}$ such that

$$a(u(\mu), v; \mu) = f(v; \mu) \quad \forall v \in \mathbb{V} \quad (4.1)$$

and evaluate $s(u) = l()$

$$s(\mu) = l(u(\mu); \mu) \quad (4.2)$$

Here s is an output of interest, $s : P \mapsto \mathbb{R}$ is the input (parameter)-output relationship, and l takes the role of a linear “output” functional which links the input to the output through the field variable $u(\mu)$.

We assume for the moment that we have complaint problems, where the following conditions are satisfied

(i) $l(\cdot; \mu) = f(\cdot; \mu), \forall \mu \in P$ the output functional and load/source functional are identical.

(ii) The bilinear form $a(\cdot, \cdot; \mu)$ is symmetric for any parameter value $\mu \in P$

Though they are quite restrictive, there are many interesting problems fulfilling these requirement across mechanics and physics, e.g., material properties, geometrical parameterization, etc.

4.1.2 Inner Products, Norms and Well-Posedness of the Parametric Weak Formulation

The Hilbert space \mathbb{V} is equipped with an intrinsic norm $\|\cdot\|_{\mathbb{V}}$. In many cases this norm coincides with, or is equivalent to, the norm induced by the bilinear form a for a fixed parameter $\mu \in P$:

$$(w, v)_{\mathbb{V}} = a(w, v; \mu) \quad \forall w, v \in \mathbb{V} \quad (4.3)$$

$$\|v\|_{\mathbb{V}} = \sqrt{a(v, v; \mu)} \quad \forall v \in \mathbb{V}$$

The well-posedness of the abstract problem formulation 4.2 can be established by the Lax-Milgram theorem [7]. In order to state a well-posed problem for all parameter values $\mu \in P$, we assume in addition to the bilinearity and the linearity of the parameterized forms $a(\cdot, \cdot; \mu)$ and $f(\cdot; \mu)$, that

(i) $a(\cdot, \cdot; \mu)$ is coercive and continuous for all $\mu \in P$ with respect to the norm $\|\cdot\|_{\mathbb{V}}$, i.e., for every $\mu \in P$, there exists a positive constant $\alpha(\mu) \geq \alpha > 0$ and a finite constant $\gamma(\mu) \leq \gamma < \infty$ such that

$$a(v, v; \mu) \geq \alpha(\mu) \|v\|_{\mathbb{V}}^2 \quad \text{and} \quad a(w, v; \mu) \leq \gamma(\mu) \|w\|_{\mathbb{V}} \|v\|_{\mathbb{V}} \quad (4.4)$$

$\forall w, v \in \mathbb{V}$

(ii) $f(\cdot; \mu)$ is continuous for all $\mu \in P$ with respect to the norm $\|\cdot\|_{\mathbb{V}}$, i.e., for every $\mu \in P$, there exists a constant $\delta(\mu) \leq \delta < \infty$ such that

$$f(v; \mu) \leq \delta(\mu) \|v\|_{\mathbb{V}}, \quad \forall v \in \mathbb{V}$$

The coercivity and continuity constants of $a(\cdot, \cdot; \mu)$ over \mathbb{V} are, respectively, defined as

$$\alpha(\mu) = \inf_{v \in \mathbb{V}} \frac{a(v, v; \mu)}{\|v\|_{\mathbb{V}}^2}, \quad \text{and} \quad \gamma(\mu) = \sup_{w \in \mathbb{V}} \sup_{v \in \mathbb{V}} \frac{a(w, v; \mu)}{\|w\|_{\mathbb{V}} \|v\|_{\mathbb{V}}} \quad (4.5)$$

$\forall \mu \in P$ Now we introduce the energy inner product and the induced energy norm as

$$(w, v)_{\mu} = a(w, v; \mu) \quad \forall w, v \in \mathbb{V} \quad (4.6)$$

$$\|v\|_{\mu} = \sqrt{a(v, v; \mu)} \quad \forall v \in \mathbb{V} \quad (4.7)$$

we note that the previous quantities are parameter dependent and by the mentioned assumptions of coercivity and continuity

4.2 Discretization Techniques

In this section we will introduce discrete approximations of the parametric weak formulation. So considering conforming approximation, i.e. there exists a space \mathbb{V}_δ which is a subset of \mathbb{V} , i.e. $\mathbb{V}_\delta \subset \mathbb{V}$ and the approximating solution is sought in \mathbb{V}_δ . This conforming nature of the space \mathbb{V}_δ would be very important in our reduction treatment.

For example the approximation space \mathbb{V}_δ can be constructed as a standard finite element method based on a triangulation and using piece-wise linear basis functions. Other examples include spectral methods or higher order finite elements, provided only that the formulation is based on a variational approach.

Now we can discretize our problem by denoting the dimension of \mathbb{V}_δ by N_δ and we equip \mathbb{V}_δ with the basis $\{\phi_i\}_{i=1}^{N_\delta}$. Then the discrete problem will read, for each $\mu \in \mathbb{P}$ find $u_\delta(\mu) \in \mathbb{V}_\delta$ such that

$$a(u_\delta(\mu), v_\delta; \mu) = f(v_\delta; \mu), \quad \forall v_\delta \in \mathbb{V}_\delta \quad (4.8)$$

and then evaluate the output

$$s_\delta(\mu) = l(u_\delta(\mu); \mu)$$

The previous problem is called the truth problem and its solution is called the truth solution and it is assumed that it can be computed for as much as high accuracy needed. However, the computation of the truth solution can be very expensive in terms of computational cost since the space \mathbb{V}_δ could have many degrees of freedom so that the desired accuracy level can be guaranteed, while it provides an accurate approximation ($u_\delta(\mu)$) in the sense that the error $\|u(\mu) - u_\delta(\mu)\|_{\mathbb{V}}$ is small enough and this model will be referred as the high fidelity model.

Thanks to the coercivity and continuity of the bilinear form, and the conformity of the approximation space, we have the Galerkin orthogonality

$$a(u(\mu) - u_\delta(\mu), v_\delta; \mu) = 0 \quad \forall v_\delta \in \mathbb{V}_\delta$$

and we can recover Cea's lemma, by letting $v_\delta \in \mathbb{V}_\delta$, then we observe that

$$\|u(\mu) - u_\delta(\mu)\|_{\mathbb{V}} \leq \|u(\mu) - v_\delta\|_{\mathbb{V}} + \|v_\delta - u_\delta(\mu)\|_{\mathbb{V}}$$

then by triangle inequality we can see that,

$$\begin{aligned} \alpha(\mu) \|v_\delta - u_\delta(\mu)\|_{\mathbb{V}}^2 &\leq a(v_\delta - u_\delta(\mu), v_\delta - u_\delta(\mu); \mu) = \\ a(v_\delta - u(\mu), v_\delta - u_\delta(\mu); \mu) &\leq \gamma(\mu) \|v_\delta - u(\mu)\|_{\mathbb{V}} \|v_\delta - u_\delta(\mu)\|_{\mathbb{V}} \end{aligned}$$

in the last step we have used both coercivity and continuity properties of the bilinear form $a(\cdot, \cdot, \mu)$, now we have proven the following:

$$\|u(\mu) - u_\delta(\mu)\|_{\mathbb{V}} \leq \left(1 + \frac{\gamma(\mu)}{\alpha(\mu)}\right) \inf_{v \in \mathbb{V}_\delta} \|u(\mu) - v\|_{\mathbb{V}}$$

This means that the approximation error $\|u(\mu) - u_\delta(\mu)\|_{\mathbb{V}}$ is closely related to the best approximation of $u_\delta(\mu)$ in the approximation space \mathbb{V}_δ through the constants $\gamma(\mu), \alpha(\mu)$

The following truth solver shows how we can compute the truth solution on the level of linear algebra:

Truth Solver

We denote the stiffness matrix and the right hand side of the truth problem 4.8 by $\mathbf{A}_\delta^\mu \in \mathbb{R}^{N_\delta \times N_\delta}$ and $f_\delta^\mu \in \mathbb{R}^{N_\delta}$, respectively, also we denote by $\mathbf{M}_\delta \in \mathbb{R}^{N_\delta \times N_\delta}$ the matrix associated with the inner product $(\cdot, \cdot)_{\mathbb{V}}$ of \mathbb{V}_δ , defined as:

$$(\mathbf{M}_\delta)_{ij} = (\phi_i, \phi_j)_{\mathbb{V}}, \quad (\mathbf{A}_\delta^\mu)_{ij} = a(\phi_i, \phi_j; \mu) \quad (f_\delta^\mu)_i = f(\phi_i; \mu)$$

for all $1 \leq i, j \leq N_\delta$ and recalling that $\{\phi_i\}_{i=1}^{N_\delta}$ are the basis for \mathbb{V}_δ then the truth problem yields:

for each $\mu \in \mathbb{P}$ find $u_\delta^\mu \in \mathbb{R}^{N_\delta}$ such that:

$$\mathbf{A}_\delta^\mu u_\delta^\mu = f_\delta^\mu$$

and as we can see from the linear system obtained above, the size of the unknown vector is N_δ and the size of the stiffness matrix is $N_\delta \times N_\delta$. So it depends on the properties of the stiffness matrix and the method used to invert the linear system, the operation count on the map $\mu \mapsto s_\delta(\mu)$ is $\mathcal{O}(N_\delta^\alpha)$ where $\alpha \geq 1$. Generally speaking it depends on N_δ .

4.3 The Solution Manifold and the Reduced Basis Approximation

As we have mentioned earlier in the introduction, reduced order methods have developed with the aim of using them in the high computationally expensive problems where we have parameters to be studied in terms of their effect on the output of interest of our problems and for this goal many methods have been created for dealing with parameterized problems, in this chapter we will give an introduction for the reduced order methods and we will consider the method called proper orthogonal decomposition (POD) which is the method that we will use for studying our high order problem.

In reduced order methods there are two main phases which are called offline and online phases, in the offline phase we explore the solution manifold in order to construct a reduced basis that will be able to approximate any member of the solution manifold, this procedure might be very expensive in terms of computational cost since it consists of solving N truth problems which have N_δ degrees of freedom and at the end we will get the N -dimensional reduced basis space. Then in the online phase we will do Galerkin projection using the bilinear form $a(\cdot, \cdot; \mu)$ with the parameter

value $\mu \in \mathbb{P}$ onto the space spanned by the reduced basis, then we can explore the parameter space at a substantially reduced cost, ideally at a cost independent of N_δ

Our main interest is to obtain the solution of the parameterized exact problem 4.2 given as:
find $u(\mu) \in \mathbb{V}$ such that

$$a(u(\mu), v; \mu) = f(v; \mu) \quad \forall v \in \mathbb{V}$$

That we refer to it as the exact solution, now we introduce the notion of solution manifold, that consists the solution of the problem under changing the parameter,i.e.

$$\mathcal{M} = \{u(\mu)|\mu \in \mathbb{P}\} \subset \mathbb{V}$$

where each $u(\mu) \in \mathbb{V}$ is the exact solution, since in many application it is hard to find the analytical exact solution then we introduce the finite subspace of \mathbb{V} which is called \mathbb{V}_δ and then we formulate the truth problem which is find $u_\delta(\mu) \in \mathbb{V}_\delta$ such that

$$a(u_\delta(\mu), v_\delta; \mu) = f(v_\delta; \mu), \quad \forall v_\delta \in \mathbb{V}_\delta \tag{4.9}$$

which we called the truth problem and we have assumed that $\|u(\mu) - u_\delta(\mu)\|_{\mathbb{V}}$ can be made arbitrarily small for any given parameter value and this basically says that we assume that a computational model is available to solve the truth problem, thus approximate the exact solution at any required accuracy, in general the cost of computations might be very high and it depends on N_δ .

Now defining the discrete version of the solution manifold we will have:

$$\mathcal{M}_\delta = \{u_\delta(\mu)|\mu \in \mathbb{P}\} \subset \mathbb{V}_\delta$$

where each $u_\delta(\mu)$ corresponds to the solution of the parametric truth problem4.9. An important assumption in the construction of any reduced model is that the solution manifold has low dimensionality, i.e., that the span of a low number of appropriately chosen basis functions represents the solution manifold with a small error. We should call these basis functions the reduced basis and it will allow us to represent the truth solution efficiently, based on N -dimensional subspace \mathbb{V}_{rb} of \mathbb{V}_δ . First of all, we assume that we have a set of reduced basis and we call them $\{\zeta_i\}_{i=1}^N \subset \mathbb{V}_\delta$ then the corresponding reduced basis space is given by

$$\mathbb{V}_{rb} = span\{\zeta_1 \dots, \zeta_N\} \subset \mathbb{V}_\delta$$

So now we are in good shape to formulate our reduced basis approximation problem which reads, for any $\mu \in \mathbb{P}$ find $u_{rb}(\mu) \in \mathbb{V}_{rb}$ such that

$$a(u_{rb}(\mu), v_{rb}; \mu) = f(v_{rb}; \mu), \quad \forall v_{rb} \in \mathbb{V}_{rb} \tag{4.10}$$

and evaluate

$$s_{rb}(\mu) = f(u_{rb}(\mu); \mu) \tag{4.11}$$

based on the assumption that we are in the complaint case, otherwise it would be $s_{rb}(\mu) = l(u_{rb}(\mu); \mu)$, the basis functions of \mathbb{V}_{rb} are given by ζ_1, \dots, ζ_N then we can represent the solution for 4.10 by $u_{rb}(\mu) = \sum_{n=1}^N (u_{rb}^\mu)_n \zeta_n$ where $\{(u_{rb}^\mu)_n\}_{n=1}^N$ are the coefficients of the reduced basis approximation.

The following reduced approximation solver shows how we can compute the reduced approximation solution on the level of linear algebra:

The reduced basis approximation

let us denote by $\{\zeta_i\}_{i=1}^N$ the reduced basis and we define the matrix $\mathbf{B} \in \mathbb{R}^{N_\delta \times N}$ such that

$$\zeta_n = \sum_{i=1}^{N_\delta} \mathbf{B}_{in} \Phi_i$$

where the \times -th column of the matrix \mathbf{B} represents the coefficients of the \times -th basis ζ_n in terms of the basis functions $\{\Phi_i\}_{i=1}^{N_\delta}$. Then the reduced basis solution matrix $\mathbf{A}_{rb}^\mu \in \mathbb{R}^{N \times N}$ and the right hand side $f_{rb}^\mu \in \mathbb{R}^N$ they will be defined by

$$(\mathbf{A}_{rb}^\mu)_{ij} = a(\zeta_i, \zeta_j; \mu) \quad (f_{rb}^\mu)_i = f(\zeta_i; \mu)$$

for all $1 \leq i, j \leq N$ and which can be computed by

$$\mathbf{A}_{rb}^\mu = \mathbf{B}^T \mathbf{A}_\delta^\mu \mathbf{B} \quad f_{rb}^\mu = \mathbf{B}^T f_\delta^\mu$$

The reduced basis approximation $u_{rb}(\mu) = \sum_{n=1}^N (u_{rb}^\mu)_n \zeta_n$ can be determined by solving the following linear system:

$$\mathbf{A}_{rb}^\mu u_{rb}^\mu = f_{rb}^\mu$$

and the output of interest will be given by $s_{rb}(\mu) = (u_{rb}^\mu)^T f_{rb}^\mu$ one main assumption in our work is that \mathcal{M}_δ approximates \mathcal{M} arbitrarily well. So now we can consider the following

$$\|u(\mu) - u_{rb}(\mu)\|_{\mathbb{V}} \leq \|u(\mu) - u_\delta(\mu)\|_{\mathbb{V}} + \|u_\delta(\mu) - u_{rb}(\mu)\|_{\mathbb{V}}$$

for the first term on the right hand side we have assumed that we can make it as arbitrarily small as possible, then the question of how much the reduced basis approximation is close to the exact solution is left to how well we can estimate the accuracy by which the reduced basis approximation approximates the truth for a given parameter value. In general the answer to the last question is problem dependent where sometimes we could have a very efficient approximation and in some problems this could not be the case.

4.4 Reduced Basis Space Generation

Now we should ask two main questions, first how we can generate accurate reduced basis spaces during the offline stage? and secondly How do we recover the reduced basis solution efficiently during the online stage?.

In general, there are many reduce order basis generation methods but in our case we will restrict ourselves to the proper orthogonal decomposition (POD) technique[42, 11, 41, 47, 15, 7, 40, 11, 45, 4, 48, 21, 12, 34, 10, 8, 18, 30, 50, 6, 9, 22, 64]. First, we begin by introducing a discrete and finite-dimensional point-set $\mathbb{P}_h \subset \mathbb{P}$ in parameter domain, it can consist of a regular lattice or a randomly generated point-set intersecting with \mathbb{P} then we can introduce the following set

$$\mathcal{M}_\delta(\mathbb{P}_h) = \{u_\delta(\mu) | \mu \in \mathbb{P}_h\}$$

of cardinality $M = |\mathbb{P}_h|$. Of course it holds that $\mathcal{M}_\delta(\mathbb{P}_h) \subset \mathcal{M}_\delta$ since $\mathbb{P}_h \subset \mathbb{P}$ but if \mathbb{P}_h is fine enough then $\mathcal{M}_\delta(\mathbb{P}_h)$ well represents \mathcal{M}_δ

4.4.1 Proper Orthogonal Decomposition (POD)

Now we will introduce the POD method, POD is a method in which we sample the parameter space and we then calculate the truth solutions for these parameter values then comes one important ingredient of POD which is compression and it is done by retaining the important informations. The N -dimensional POD-space is the space that minimizes the following quantity

$$\sqrt{\frac{1}{M} \sum_{\mu \in \mathbb{P}_h} \inf_{v_{rb} \in \mathbb{V}_{rb}} \|u_\delta(\mu) - v_{rb}\|_{\mathbb{V}}^2} \quad (4.12)$$

over all N -dimensional subspaces \mathbb{V}_{rb} of the span $\mathbb{V}_{\mathcal{M}} = \text{span}\{u_\delta(\mu) | \mu \in \mathbb{P}_h\}$ of the elements of $\mathcal{M}_\delta(\mathbb{P}_h)$, now if we introduce the ordering μ_1, \dots, μ_M of the values in \mathbb{P}_h then we have the ordering of the corresponding truth solutions $u_\delta(\mu_1), \dots, u_\delta(\mu_M)$ which are all elements of $\mathcal{M}_\delta(\mathbb{P}_h)$. For the sake of short notation we let $\psi_m = u_\delta(\mu_m)$ for all $m = 1, \dots, M$. Now in order to build our POD space, we define the following symmetric and linear operator $C : \mathbb{V}_{\mathcal{M}} \mapsto \mathbb{V}_{\mathcal{M}}$

$$C(v_\delta) = \frac{1}{M} \sum_{m=1}^M (v_\delta, \psi_m)_{\mathbb{V}} \psi_m, \quad v_\delta \in \mathbb{V}_{\mathcal{M}},$$

Now we consider the eigenvalue-eigenfunction pairs $(\lambda_n, \zeta_n) \in \mathbb{R} \times \mathbb{V}_{\mathcal{M}}$ of the operator C with the normalization constraint $\|\zeta_n\|_{\mathbb{V}} = 1$ which satisfy the following:

$$(C(\zeta_n), \psi_m)_{\mathbb{V}} = \lambda_n (\zeta_n, \psi_m)_{\mathbb{V}}, \quad 1 \leq m \leq M. \quad (4.13)$$

Here we assume that the eigenvalues are sorted in descending order $\lambda_1 \geq \lambda_2 \geq \dots \geq \lambda_M$. Then the POD basis functions are given by ζ_1, \dots, ζ_M which span $\mathbb{V}_{\mathcal{M}}$. Then we can truncate the basis by taking first N functions ζ_1, \dots, ζ_N and they span the N -dimensional space \mathbb{V}_{POD} and here these basis functions retain the most energy and this an important concept in POD, \mathbb{V}_{POD} will be the minimizer of the quantity 4.12 .

Proper Orthogonal Decomposition (POD)

Now we will address the POD approach on the linear algebra level:

Let $\psi_m = u_\delta(\mu_m)$ for $m = 1, \dots, M$, then we construct the correlation matrix $\mathbf{C} \in \mathbb{R}^{N \times N}$ by:

$$\mathbf{C}_{mq} = \frac{1}{M}(\psi_m, \psi_q)_{\mathbb{V}}, \quad 1 \leq m, q \leq M$$

Then we find the N largest eigenvalue-eigenvector pairs (λ_n, v_n) of the matrix \mathbf{C} with $\|v_n\|_{l^2(\mathbb{R}^M)}^2 = 1$ such that

$$\mathbf{C}v_n = \lambda_n v_n, \quad 1 \leq n \leq N$$

which is equivalent to 4.13. with the eigenvalues sorted in descending order $\lambda_1 \geq \lambda_2 \geq \dots \geq \lambda_M$ the orthogonal POD basis functions ζ_1, \dots, ζ_N span the reduced order space $\mathbb{V}_{rb} = \text{span}\{\zeta_1, \dots, \zeta_N\}$ and are given by the following linear combination

$$\zeta_n(x) = \frac{1}{\sqrt{M}} \sum_{m=1}^M (v_n)_m \psi_m(x), \quad 1 \leq n \leq N$$

where $(v_n)_m$ denotes the m -th coefficient of the eigenvector $v_n \in \mathbb{R}^M$

4.5 POD-Galerkin projection with Finite Volume

Now in this section we will address the POD-Galerkin projection procedure for finite volume discretization (FVD) since as we have mentioned earlier we are using OpenFOAM as our solver which is an open source solver based on FVD and thus we have to develop the procedure of applying POD in this framework. In this section we will introduce the POD-ROM method in FVD for both Navier-Stokes equations and Reynolds averaged Navier-Stokes equations for laminar and turbulent respectively, this what can be found in [32] and we will adopt that formulation in our work.

So now will start with treatment of Navier-Stokes equations where we don't have any turbulence modelling. The equations read

$$\begin{cases} \frac{\partial \mathbf{u}}{\partial t} + (\mathbf{u} \cdot \nabla) \mathbf{u} - \nu \Delta \mathbf{u} = -\nabla p \\ \nabla \cdot \mathbf{u} = 0 \end{cases} \quad (4.14)$$

where \mathbf{u} is the field velocity of the flow, p is the normalized pressure, and ν is the kinematic viscosity. The equations are given in a domain Ω with proper boundary and initial conditions.

Now it is important to notice that we have time evolution in the N-S equations so we need to deal a little bit differently with the POD procedure so first we assume that the reduced order solution for the velocity is given by a linear combination of the basis functions (which depends only on space) multiplied by a temporal coefficients $a_i(t)$. So this assumption gives:

$$\mathbf{u}(\mathbf{x}, t) \approx \mathbf{u}_r(\mathbf{x}, t) = \sum_{i=1}^{N_r} a_i(t) \Phi_i(\mathbf{x}) \quad (4.15)$$

As we have mentioned before the POD modes are chosen such that they are the most energetic ones, so the POD space will be

$$\mathbb{V}_{POD} := \text{span}\{\Phi_i\}, \quad i = 1, \dots, N_r \quad (4.16)$$

where N_r is the number of modes that we have to truncate from the eigenvectors of the correlation matrix. The next step is the start from a set of velocities which are sampled at different times which we will call the snapshots.

$$\mathbf{u}_n(\mathbf{x}) := \mathbf{u}(\mathbf{x}, t_n), \quad n = 1, \dots, N_s \quad (4.17)$$

where here N_s is the number of total snapshots, in our case the snapshots will be simply the numerical solutions that OpenFOAM computes and we will refer to them as the high fidelity solutions, the POD space in our settings will be the minimizer of the difference between the snapshots and the projection of the snapshots on the spatial modes (the basis) in the L^2 -norm, that is:

$$V_{POD} = \operatorname{argmin} \frac{1}{N_s} \sum_{n=1}^{N_s} \left\| \mathbf{u}_n(\mathbf{x}) - \sum_{i=1}^{N_r} (\mathbf{u}_n(\mathbf{x}), \Phi_i(\mathbf{x}))_{L^2} \Phi_i(\mathbf{x}) \right\|_{L^2}^2 \quad (4.18)$$

with

$(\Phi_i, \Phi_j)_{L^2} = \delta_{ij}$ where δ_{ij} is the Kronecker delta function, and to solve 4.18 we have to build the correlation matrix of the velocity snapshots and considering then the eigenvalue problem so we have:

$$\mathbf{C}\zeta_i = \lambda_i\zeta_i, \quad 1 \leq i \leq N_s \quad (4.19)$$

where $\mathbf{C} \in \mathbb{R}^{N_s \times N_s}$ is the correlation matrix with components computed as follows:

$$C_{ij} = \frac{1}{N_r} (\mathbf{u}_i(\mathbf{x}), \mathbf{u}_j(\mathbf{x}))_{L^2}, \quad \text{for } i, j = 1, \dots, N_s \quad (4.20)$$

then the basis are given by

$$\Phi_i(\mathbf{x}) = \frac{1}{\sqrt{\lambda_i}} \sum_{n=1}^{N_s} \zeta_{i,n} \mathbf{u}_n(\mathbf{x}), \quad i = 1, \dots, N_r \quad (4.21)$$

and here we underline again that the first modes have the property of retaining the most of the energy present in the original solutions [6].

Now inserting eq 4.15 in eq 4.14 and employing Galerkin method gives:

$$\frac{da_i(t)}{dt} = \nu \sum_{i=1}^{N_r} B_{ji} a_i(t) - \sum_{k=1}^{N_r} \sum_{i=1}^{N_r} C_{jki} a_k(t) a_i(t), \quad j = 1, \dots, N_r \quad (4.22)$$

where

$$B_{ji} = (\nabla \Phi_j, \nabla \Phi_i)_{L^2} \quad (4.23)$$

$$C_{jki} = (\Phi_j, (\Phi_k \cdot \nabla) \Phi_i)_{L^2} \quad (4.24)$$

$$a_j(0) = (\Phi_j, \mathbf{u}_1(\mathbf{x}))_{L^2} \quad (4.25)$$

Eq. 4.22 can be written as an autonomous dynamical system in which the unknowns are the time dependent coefficients $a_i(t)$:

$$\dot{\mathbf{a}} = \nu \mathbf{B}\mathbf{a} - \mathbf{a}^T \mathbf{C}\mathbf{a} \quad (4.26)$$

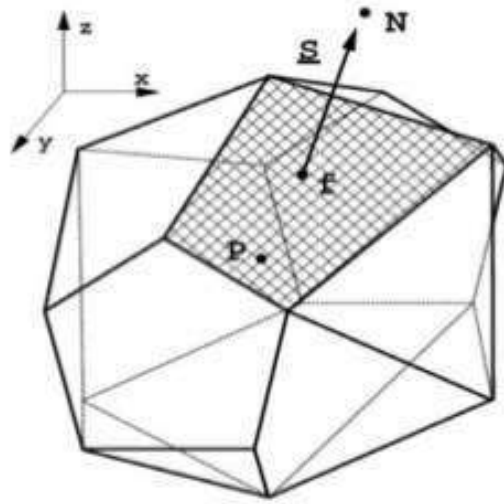


FIGURE 4.1: Example of a control volume [24]

Here in the previous derivation there are two important assumptions we have made: (i) The lack of the pressure in eq 4.22 which can be justified by the fact that POD modes are linear combinations of the snapshots which are divergence-free fields because they satisfy the continuity equation. So in fact the Galerkin projection of the pressure terms gives:

$$(\Phi_i, \nabla p)_{L^2} = \int_{\Omega} \Phi_i \cdot \nabla p d\mathbf{x} = - \int_{\Omega} p \cdot (\nabla \cdot \Phi_i) d\mathbf{x} + \int_{\partial\Omega} p \cdot (\Phi_i \cdot \mathbf{n}) d\mathbf{x} \quad (4.27)$$

Where here first term is zero because of the continuity equation and second in also zero for enclosed flows [30]. In general pressure term can be neglected but in some other case they should be taken into account and here we will have some additional terms [38], [5]. (ii) The second thing to be remarked here is that the term \mathbf{B}_{ji} in eq 4.22 which represents the diffusive term is derived keeping in mind that $\Delta u = \text{div}(\nabla u)$ and so Green formula has been used which is common in usual weak formulation of differential problem in finite element (FE).

Now we will address some important considerations about FVD which have to be taken into account before setting the final model for POD-G-ROM for FVD, now if we consider the 4.14 and we take the momentum balance, then the integral form on a generic control volume V_P gives

$$\int_t^{t+\Delta t} \left[\frac{\partial}{\partial t} \int_{V_P} \mathbf{u}_t dV + \int_{V_P} (\mathbf{u} \cdot \nabla) \mathbf{u} dV - \nu \int_{V_P} \Delta \mathbf{u} dV + \int_{V_P} \nabla p dV \right] dt = 0 \quad (4.28)$$

Now to obtain proper POD-FV-ROM, we need to account for the following issues in the discretization of N-S equations: (i) The convective non linear term will be discretized as follows by applying the generalized form

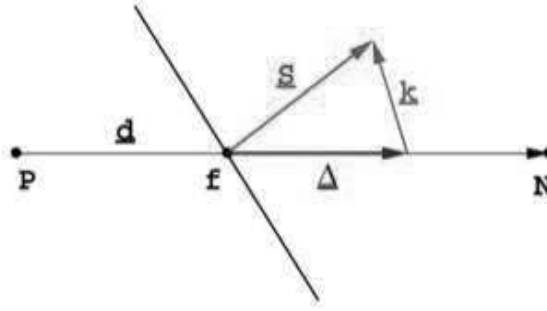


FIGURE 4.2: Non-orthogonality treatment of the diffusive term [24]

of Gauss theorem as [24] :

$$\int_{V_P} (\mathbf{u} \cdot \nabla) \mathbf{u} dV = \int_{V_P} \nabla \cdot (\mathbf{u}\mathbf{u}) dV \approx \sum_f \mathbf{S}_f \cdot \mathbf{u}_f \mathbf{u}_f = \sum_f F \mathbf{u}_f \quad (4.29)$$

where S_f is the face area vector of the face see 4.1 and F is the face flux. This tells us that we have to take flux field into consideration when we do POD-FV-ROM procedure so that we keep consistency with respect to the high order model.

(ii) The continuity equation is discretized as follows

$$\int_{V_P} \nabla \cdot \mathbf{u} dV = \sum_f \mathbf{S}_f \cdot \mathbf{u}_f = \sum_f F = 0 \quad (4.30)$$

So here the divergence free constraint is applied not to the cell center value but to the face flux so we can not neglect the pressure term since the snapshots are calculated in the center cell value are not divergence free.

(iii) The diffusive term is discretized as

$$\nu \int_{V_P} \Delta \mathbf{u} dV = \nu \sum_f \mathbf{S}_f \cdot \nabla \mathbf{u}_f = \nu \sum_f |\Delta| \frac{\mathbf{u}_N - \mathbf{u}_P}{|\mathbf{d}|} + \mathbf{k} \cdot (\nabla \mathbf{u})_f \quad (4.31)$$

The first term is the orthogonal part and the second one is the non-orthogonal one see 4.2.

Another way of discretizing the latter term is by observing that $\Delta u = \text{div}(\nabla u)$ and then applying Green formula for the divergence operator, that yields

$$\nu \int_{V_P} \nabla \cdot \nabla \mathbf{u} dV = \nu \sum_f \mathbf{S}_f \cdot \nabla \mathbf{u}_f = \nu \sum_f \mathbf{S}_f \cdot \left[f_x \left(\frac{1}{V} \sum_f \mathbf{S}_f \mathbf{u}_f \right)_P + (1-f_x) \left(\frac{1}{V} \sum_f \mathbf{S}_f \mathbf{u}_f \right)_N \right] \quad (4.32)$$

It can be noticed that the Green formula leads to a different discretization of the diffusive term, eq 4.31 is usually preferred to eq 4.32. Both are second order accurate, but the second one involves a larger computational molecule. So Green formula could not be used in POD-FV-ROM since it would introduce discretization discrepancies between the high order model and the reduced order one.

So now we can go a head to the POD-FV-ROM procedure accounting the issues (i-iii) mentioned above, and doing the relevant modifications on the form of POD-G-ROM that we obtained for the dynamical system 4.26.

Taking into account the remarks that we have just mentioned, we conclude that we need to have calculate the face flux and to take into account the pressure terms and finally to include the boundary conditions in the formulations since we cannot use Green formula in dealing with the diffusive term.

The first thing can be solved just by constructing the face flux and the pressure by using the N_r – modes as we have done with velocity using the same coefficients that we used for velocity:

$$F(\mathbf{x}, t) \approx F_r(\mathbf{x}, t) = \sum_{i=1}^{N_r} a_i(t) \psi_i(\mathbf{x}) \quad (4.33)$$

$$p(\mathbf{x}, t) \approx p_r(\mathbf{x}, t) = \sum_{i=1}^{N_r} a_i(t) \chi(\mathbf{x}) \quad (4.34)$$

where $\psi_i(\mathbf{x})$ and $\chi(\mathbf{x})$ are the spatial modes for the flux and the pressure respectively, these modes are calculated using the correlation matrix of the velocity in eq. 4.13, while the snapshots for flux and pressure $F_n(\mathbf{x})$ $p_n(\mathbf{x})$ are the high order ones (in our case the OpenFOAM numerical solutions):

$$\psi_i(\mathbf{x}) = \frac{1}{\sqrt{\lambda_i}} \sum_{n=1}^{N_s} \zeta_{i,n} F_n(\mathbf{x}), \quad i = 1, \dots, N_r \quad (4.35)$$

$$F_n(\mathbf{x}) := F(\mathbf{x}, t_n), \quad n = 1, \dots, N_s \quad (4.36)$$

$$\chi_i(\mathbf{x}) = \frac{1}{\sqrt{\lambda_i}} \sum_{n=1}^{N_s} \zeta_{i,n} p_n(\mathbf{x}), \quad i = 1, \dots, N_r \quad (4.37)$$

$$p_n(\mathbf{x}) := p(\mathbf{x}, t_n), \quad n = 1, \dots, N_s \quad (4.38)$$

it should be noted that in our approach we are using the same time dependent coefficients in the construction of the reduced order velocity, flux and pressure, also we have used velocity correlation matrix for finding the spatial modes for flux and pressure while in other approaches a combination of pressure and velocity snapshots has been used to find the modes like [5].

This approach can be interpreted as if the state vector of the variables of interest was expanded as linear combination of state vector spatial modes:

$$\begin{pmatrix} \mathbf{u}(\mathbf{x}, t) \\ F(\mathbf{x}, t) \\ p(\mathbf{x}, t) \end{pmatrix} \approx \begin{pmatrix} \mathbf{u}_r(\mathbf{x}, t) \\ F_r(\mathbf{x}, t) \\ p_r(\mathbf{x}, t) \end{pmatrix} = \sum_{i=1}^{N_r} a_i(t) \begin{pmatrix} \Phi_i(\mathbf{x}) \\ \psi_i(\mathbf{x}) \\ \chi_i(\mathbf{x}) \end{pmatrix} \quad (4.39)$$

Now inserting 4.39 into 4.14 gives the following POD-Galerkin ROM for Finite Volume discretization (POD-FV-ROM)

$$\frac{da_i(t)}{dt} = \nu \sum_{i=1}^{N_r} B_{ji} a_i(t) - \sum_{k=1}^{N_r} \sum_{i=1}^{N_r} C_{jki} a_k(t) a_i(t) - \sum_{i=1}^{N_r} A_{ji} a_i(t), \quad j = 1, \dots, N_r \quad (4.40)$$

where

$$B_{ji} = (\Phi_j, \Delta \Phi_i)_{L^2} \quad (4.41)$$

$$C_{jki} = (\Phi_j, \nabla \cdot (\psi_k \Phi_i))_{L^2} \quad (4.42)$$

$$A_{ji} = (\Phi_j, \nabla \chi_i)_{L^2} \quad (4.43)$$

Finally the dynamical system can be written as

$$\dot{\mathbf{a}} = \nu \mathbf{B} \mathbf{a} - \mathbf{a}^T \mathbf{C} \mathbf{a} - \mathbf{A} \mathbf{a} \quad (4.44)$$

Here we remind that we have not applied Green formula for the terms B_{ji} for the reasons that we have mentioned previously regarding the discretization of the diffusive term, and this has very important impact on our work since it means that the boundary conditions are embedded in the terms B_{ji} and they don't appear directly in the formulation of POD-FV-ROM and this affects us since in our case and even in most of the parameterized ROM procedures, we use the boundary velocity as the parameter in our model. So we have to parameterize the velocity at the BC in the reduced order model which is something can be taken into account by introducing a method called the POD penalty method [54] in which the BCs can be enforced. As in spectral methods [18], we put Dirichlet boundary condition as constraints in N-S equations.

$$(\Phi_j, \mathbf{u}_t + (\mathbf{u} \cdot \nabla) \mathbf{u} - \nu \Delta \mathbf{u} + \nabla p + \tau \Gamma (\mathbf{u} - \mathbf{u}_{\text{BC}}))_{L^2} = 0 \quad (4.45)$$

where \mathbf{u}_{BC} is the Dirichlet boundary condition, τ is the penalty factor and Γ is a null function everywhere except on the boundary where the condition is imposed [54]. There are two main advantages of this method, first, this procedure enforces the approximated velocity \mathbf{u}_r to respect the BC of the problem. This should not be taken for granted since the approximated velocity is a linear combination of spatial functions. which in general do not respect the Dirichlet BC. The second advantage in using the POD penalty method lays in the fact that now the model is not autonomous anymore. In this way, some wrong long-time integration behavior and the initial condition issue are less troublesome [54]. Regarding the penalty factor τ , there is no general way of setting it and so a sensitivity analysis can be used to set it [8], [24]. What we can say is if τ tends to zero then this means that we are not enforcing the BC's while if it tends to infinity then the ROM becomes ill-conditioned [54].

The POD-FV-ROM system will be changed to:

$$\frac{da_i(t)}{dt} = \nu \sum_{i=1}^{N_r} B_{ji} a_i(t) - \sum_{k=1}^{N_r} \sum_{i=1}^{N_r} C_{jki} a_k(t) a_i(t) - \sum_{i=1}^{N_r} A_{ji} a_i(t) + \tau \left(\mathbf{u}_{BC} \cdot \mathbf{D}_j - \sum_{i=1}^{N_r} E_{ji} a_i(t) \right) \quad (4.46)$$

where here with have two additional terms with respect to eq.4.26:

$$\mathbf{D}_j = (\Phi_j, \Phi_j)_{L^2, \partial\Omega} \quad (4.47)$$

$$E_{ji} = (\Phi_j, \Phi_i)_{L^2, \partial\Omega} \quad (4.48)$$

The POD-FV-ROM dynamical system for incompressible laminar N-S equations reads as

$$\dot{\mathbf{a}} = \nu \mathbf{B} \mathbf{a} - \mathbf{a}^T \mathbf{C} \mathbf{a} - \mathbf{A} \mathbf{a} + \tau (\mathbf{u}_{BC} \mathbf{D} - \mathbf{E} \mathbf{a}) \quad (4.49)$$

After we have discussed the POD-FV-ROM procedure for N-S equations for laminar fluids, now it is the time to move for RANS equations where turbulence modelling takes place for turbulence fluids, see [43], [44], [62], [2] and [63] doing the first POD-Galerkin-ROM procedure but now for the case of turbulent flows gives the following:

$$\frac{da_i(t)}{dt} = \nu \sum_{i=1}^{N_r} B_{ji} a_i(t) - \sum_{i=1}^{N_r} H_{ji} a_i(t) - \sum_{k=1}^{N_r} \sum_{i=1}^{N_r} C_{jki} a_k(t) a_i(t) - \sum_{i=1}^{N_r} A_{ji} a_i(t), \quad j = 1, \dots, N_r \quad (4.50)$$

where

$$H_{ji} = (\nabla \Phi_j, \nu_{EV} \nabla \Phi_i)_{L^2} \quad (4.51)$$

and ν_{EV} is the eddy viscosity for which there are many models in the literature, one may refer to [63]. RANS equations read:

$$\begin{cases} \frac{\partial \mathbf{u}}{\partial t} + (\mathbf{u} \cdot \nabla) \mathbf{u} = \nabla \cdot -p \mathbf{I} + (\nu + \nu_t) (\nabla \mathbf{u} + \nabla \mathbf{u}^T) - 2/3 k \mathbf{I} \\ \nabla \cdot \mathbf{u} = 0 \end{cases} \quad (4.52)$$

where ν_t is the turbulent viscosity which will be taken into account in our ROM formulation as another variable to be expanded in the same way we have done with flux, velocity and pressure in the laminar case that is:

$$\nu_t(\mathbf{x}, t) \approx \nu_{t,r}(\mathbf{x}, t) = \sum_{i=1}^{N_r} a_i(t) \phi_i(\mathbf{x}) \quad (4.53)$$

where $\phi_i(\mathbf{x})$ are the spatial modes for the eddy viscosity, and building the snapshots for the eddy viscosity will give

$$\phi_i(\mathbf{x}) = \frac{1}{\sqrt{\lambda_i}} \sum_{n=1}^{N_s} \zeta_{i,n} \nu_{t,n}(\mathbf{x}), \quad i = 1, \dots, N_r \quad (4.54)$$

$$\nu_{t,n}(\mathbf{x}) := \nu_t(\mathbf{x}, t_n), \quad n = 1, \dots, N_s \quad (4.55)$$

Also here will assume to have the same time coefficients like the laminar case for the variables so we will have

$$\begin{pmatrix} \mathbf{u}(\mathbf{x}, t) \\ F(\mathbf{x}, t) \\ p(\mathbf{x}, t) \\ \nu_t(\mathbf{x}, t) \end{pmatrix} \approx \begin{pmatrix} \mathbf{u}_r(\mathbf{x}, t) \\ F_r(\mathbf{x}, t) \\ p_r(\mathbf{x}, t) \\ \nu_{t,r}(\mathbf{x}, t) \end{pmatrix} = \sum_{i=1}^{N_r} a_i(t) \begin{pmatrix} \Phi_i(\mathbf{x}) \\ \psi_i(\mathbf{x}) \\ \chi_i(\mathbf{x}) \\ \phi_i(\mathbf{x}) \end{pmatrix} \quad (4.56)$$

Then the POD-FV-ROM for the RANS eddy viscosity model reads:

$$\begin{aligned} \frac{da_i(t)}{dt} = & \nu \sum_{i=1}^{N_r} B_{ji} a_i(t) + \nu \sum_{i=1}^{N_r} BT_{ji} a_i(t) \\ & - \sum_{k=1}^{N_r} \sum_{i=1}^{N_r} C_{jki} a_k(t) a_i(t) + \\ & \sum_{k=1}^{N_r} \sum_{i=1}^{N_r} CT1_{jki} a_k(t) a_i(t) + \sum_{k=1}^{N_r} \sum_{i=1}^{N_r} CT2_{jki} a_k(t) a_i(t) + \\ & \sum_{i=1}^{N_r} A_{ji} a_i(t) - \tau \left(\mathbf{u}_{\mathbf{BC}} \cdot \mathbf{D}_j - \sum_{i=1}^{N_r} E_{ji} a_i(t) \right) \end{aligned} \quad (4.57)$$

where the additional terms with respect to Eq.4.46 are:

$$BT_{ji} = (\Phi_j, \nabla \cdot (\nabla \Phi_j^T))_{L^2} \quad (4.58)$$

$$CT1_{jki} = (\Phi_j, \phi_k \Delta \Phi_i)_{L^2} \quad (4.59)$$

$$CT2_{jki} = (\Phi_j, \nabla \cdot \phi_k (\nabla \Phi_i^T))_{L^2} \quad (4.60)$$

Then the dynamical system can be written as

$$\dot{\mathbf{a}} = \nu(\mathbf{B} + \mathbf{BT})\mathbf{a} - \mathbf{a}^T(\mathbf{C} - \mathbf{CT1} - \mathbf{CT2})\mathbf{a} - \mathbf{Aa} + \tau(\mathbf{u}_{\mathbf{BC}}\mathbf{D} - \mathbf{Ea}) \quad (4.61)$$

Chapter 5

Reduced order results for the flow past a cylinder

5.1 Numerical simulations results

In this section we will present and discuss our simulations results for both laminar and turbulent flows reduced order model. We would like to remind the reader that we have applied the procedure of POD-FV-ROM introduced in [32] and which has been discussed in the previous section. The study case that we have considered is that of the flow past a circular cylinder which is our main full order problem, and that has been investigated in its full order settings in Chapter 2.

First we have studied the case of laminar flow with very low Reynolds number ($Re \approx 100 - 200$). If we go more into the details of the POD procedure we start the by computing the spatial modes for velocity, flux and pressure. After that we do singular value decomposition for the correlation matrix of the velocity. Thus, the first question was how to choose a suitable set of snapshots.

In this work, we took a number of Snapshots covering one small window which corresponds to two time periods of the high order time history for the lift coefficient (in fact we verified that taking snapshots with the same density over 4 or 5 periods was not affecting the results of analysis). We have studied the results by comparing velocity and pressure fields between the high fidelity and the ROM simulations. We also considered one important output of interest in our case, which is the lift coefficient. Its importance comes from the fact that it is needed to solve the structural equation in order to obtain the motion of the cylinder.

We have used first the high fidelity lift coefficient time history to calculate the lift period so that we can set a time step for taking the snapshots. As we can see in figure 5.1 the final regime of the laminar simulation at $Re = 100$ has been reached after 1500 seconds and the period is about 76 seconds. Thus, we tested two different schemes for taking the snapshots. In both cases we tried to cover almost three periods (from time = 2000 s till 2229.37). In one case, we have taken just 60 snapshots (20/period) and in the other case we have taken 120 snapshots (40/period). We have set $\tau = 0.1$ and we have used MATLAB to solve the ODE system 4.49, typically the ROM time integration required about 60 seconds which corresponds to a speed up of 60 times of the high fidelity solver. Of course in this case we

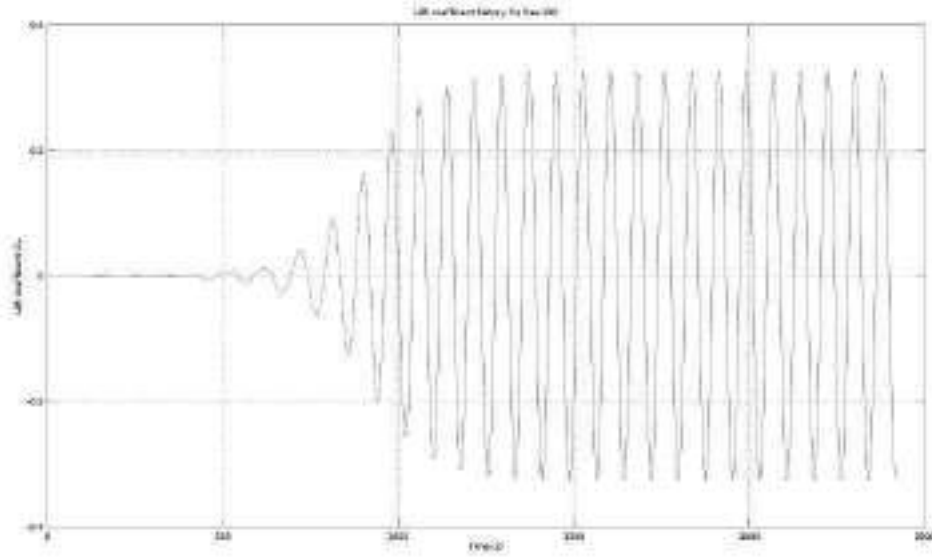


FIGURE 5.1: Lift Coefficient history for the cylinder case
Re=100

have set \mathbf{u}_{BC} to be the velocity corresponding to $Re = 100$ so that we can recover the reduced order solution for flux, pressure and velocity of that case to be able to compare with the high fidelity one computed by OpenFOAM.

In figure 5.2, we can see the velocity fields both the high fidelity one and the reduced order one and also the error. Notice that the error is computed as follows:

$$err_U = |mag(\mathbf{U}_{L,HF} - \mathbf{U}_{L,ROM})|$$

the same comparison for pressure is presented in figure 5.3, with the error defined as

$$err_p = |p_{L,HF} - p_{L,ROM}|$$

In figure 5.4, we can see the lift coefficient recovered from the process of ROM that we have done on the case of the cylinder for $Re=100$. In the plot, we compared POD solutions obtained starting from 60 and 120 snapshots respectively. The plots show that the reduced order model solution reproduces qualitatively well the solution obtained with the high fidelity model. Both pressure and velocity fields cannot in fact be distinguished at a glance from the high fidelity ones. By quantitative standpoint, the relative error value for U amounts to 1.6% in L_∞ -norm and to 0.3% in L_2 -norm as for pressure we have relative error of 0.95% in L_∞ -norm and 0,92% in L_2 -norm. It is obvious that only with 120 snapshots it was possible to recover the lift coefficient very accurately defining the error as

$$err = \frac{\|C_{L,HF} - C_{L,ROM}\|_{L^2[2000,2229.37]}}{\|C_{L,HF}\|_{L^2[2000,2229.37]}}$$

Notice that in both case in figure 5.4 we use the same number of modes which is 10. The value of the error that is defined above which is the relative one in L^2 is about 12.144% and 0.44544% and this gives an idea that with 120 snapshots we were able to get better results.

TABLE 5.1: The error in L^2 -norm for the ROM lift coefficient with varying the number of modes used

Number of modes	Relative Error
2	1.0014363
3	0.0685620
5	0.0886061
8	0.0660731
10	0.0054784
13	0.0040657

In figures 5.5;5.6 and 5.7 we can see the effect of changing the number of modes and we can see that with just 2 modes it was clearly insufficient for recovering at least the general shape and so the frequency of the vortex shedding while for number of modes more than or equal three we start getting decent results in terms of shape, periodicity of the lift coefficient and in general relative error as defined in the previous case. Values of the error are reported in table 5.1.

Now we move to study ROM for turbulent flows, where we have considered the case of cylinder subjected to flow but fixed with out being able to vibrate, and we have studied the case of $Re=6000$, and we have considered around four periods of the lift coefficient.

In figure 5.8, we can see the velocity fields both the high fidelity one and the reduced order one and also the error which is computed in the same way as in the laminar case.

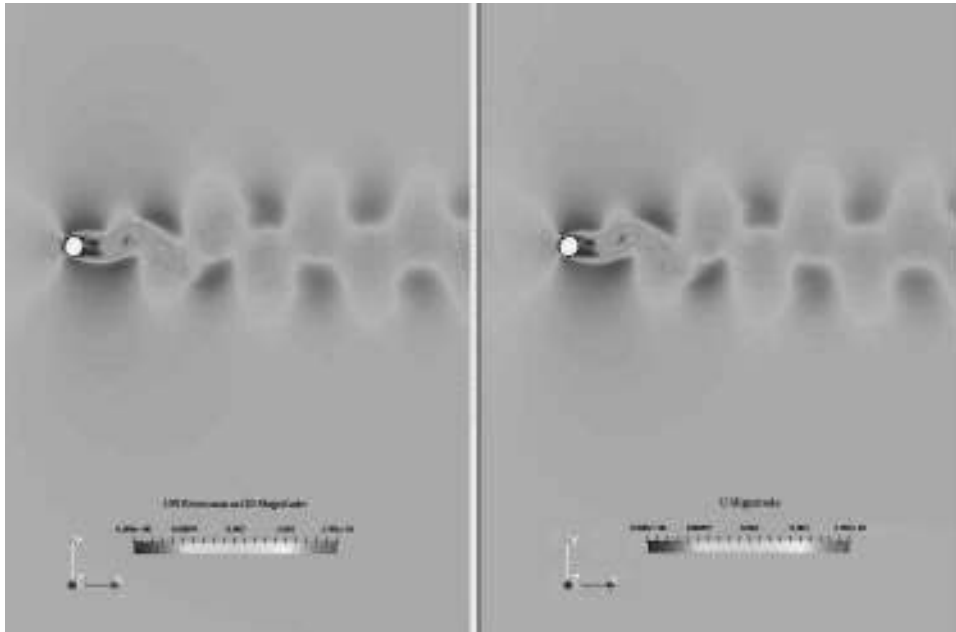
also we can see both ROM and HF pressure in 5.3, with the error defined as in the laminar case

In figure 5.10 we can see the computed high fidelity lift coefficient for the fixed cylinder that is subjected to an inlet velocity that corresponds to $Re=6000$. As in the laminar case we are interested in reproducing such output by means of reduced order model time integration.

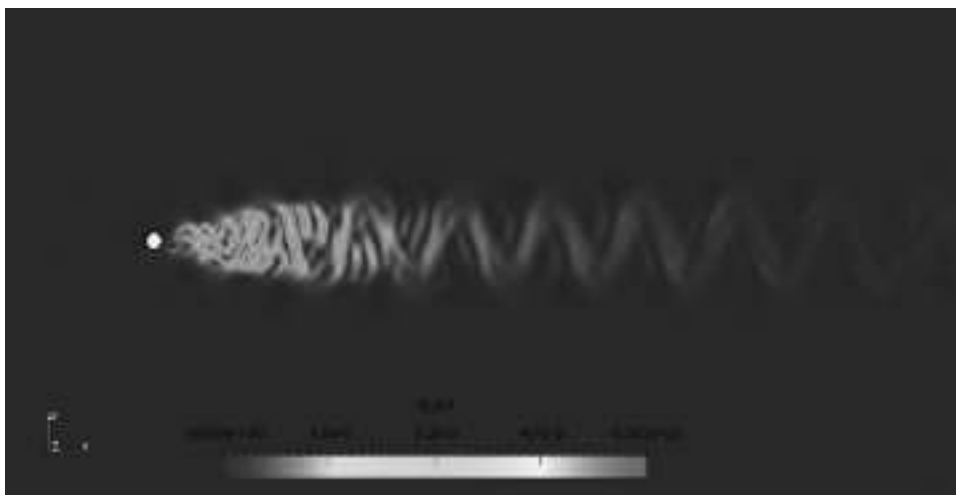
In figure 5.11 we can see the result of our ROM procedure applied to the case of $Re=6000$ for the fixed cylinder. The ROM has been done for time window $t = 81$ and $t = 85$ where we have four periods of the high fidelity solution. We can see that in the first period we have good approximation of the HF lift coefficient but then the ROM-CL started to diverge and getting bigger in absolute maximum peaks.

Now repeating the same error analysis as we have done in the laminar case for both velocity and pressure fields, we get these values for velocity $err = 0.0066220\%$ in L^2 -norm and $err = 29.307\%$ in L^∞ -norm. While for pressure we have $err = 4.9135\%$ in L^2 -norm.

We were obviously not successful in recovering the lift coefficient with the same accuracy as we did in the laminar case. We here recall that in this we followed the strategy proposed in [32], which avoided taking snapshots

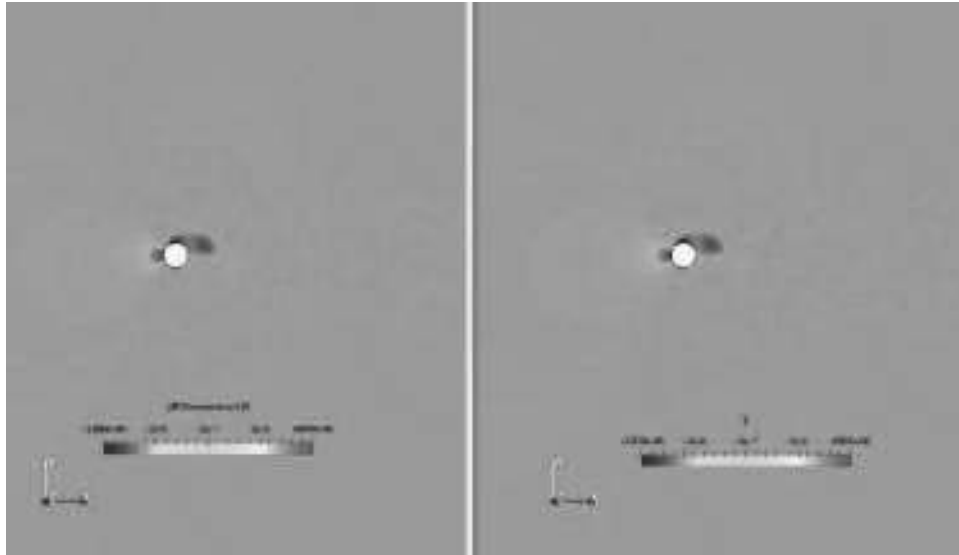


(A) Comparison between velocity fields for the case of the cylinder immersed in flow at $Re=100$ at time=2229.37, on the right it is the high fidelity one and on the left it is the ROM one

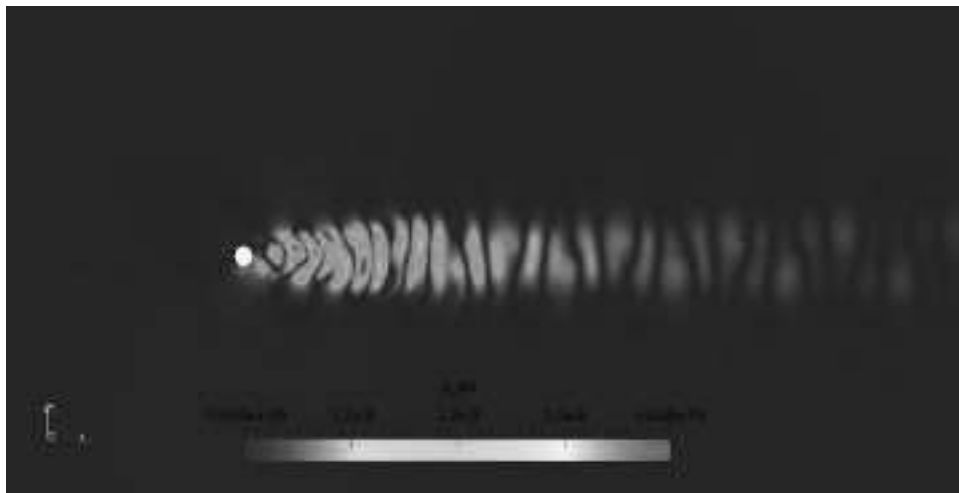


(B) The error difference between HF and ROM velocity for the case of the cylinder immersed in flow at $Re=100$ at time=2229.37

FIGURE 5.2: Comparison between velocity fields for the case of the cylinder immersed in flow at $Re=100$ at time=2229.37 with the error being the magnitude of the difference divided by the L^2 -norm



(A) Comparison between pressure fields for the case of the cylinder immersed in flow at $Re=100$ at time=2229.37, on the right it is the high fidelity one and on the left it is the ROM one



(B) The error difference between HF and ROM pressure for the case of the cylinder immersed in flow at $Re=100$ at time=2229.37

FIGURE 5.3: Comparison between pressure fields for the case of the cylinder immersed in flow at $Re=100$ at time=2229.37 with the error being the absolute value of the difference divided by the L^2 -norm

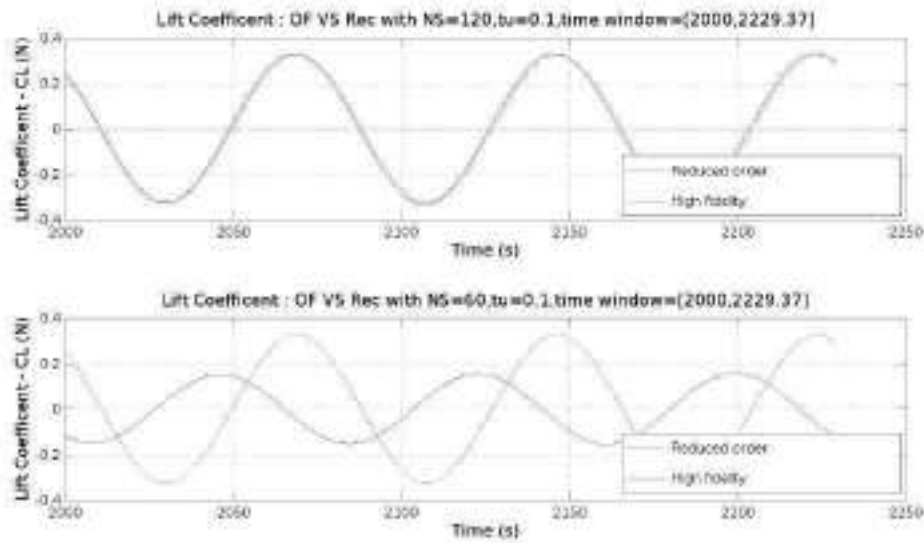


FIGURE 5.4: High fidelity VS ROM lift coefficient for $Re=100$ with different number of snapshots (120 in the one in the top and 60 in the one in the bottom) with same value of penalty factor $\tau = 0.1$, in red it is the high fidelity solution and in blue it is the ROM solution

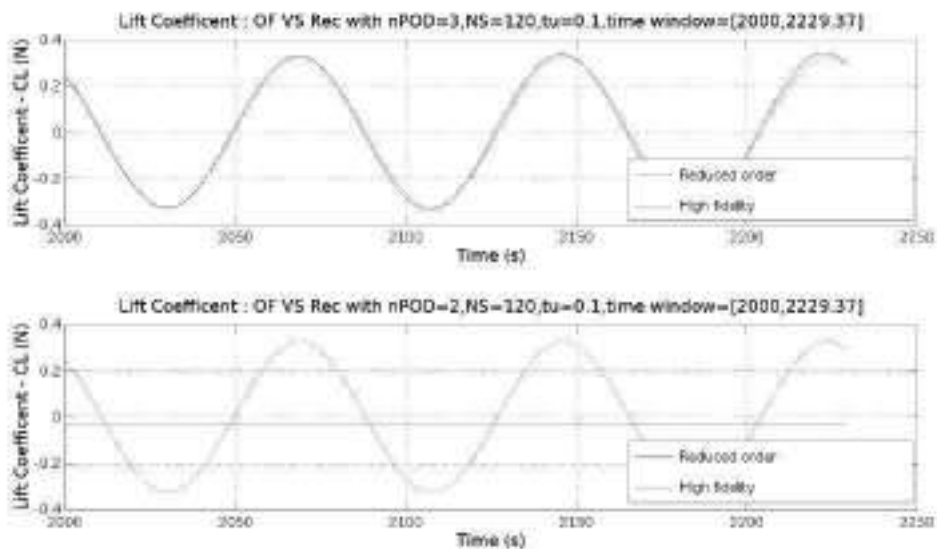


FIGURE 5.5: High fidelity VS ROM lift coefficient for $Re=100$ with different number of modes with same value of penalty factor $\tau = 0.1$ and same number of snapshots which is 120, in red it is the high fidelity solution and in blue it is the ROM solution

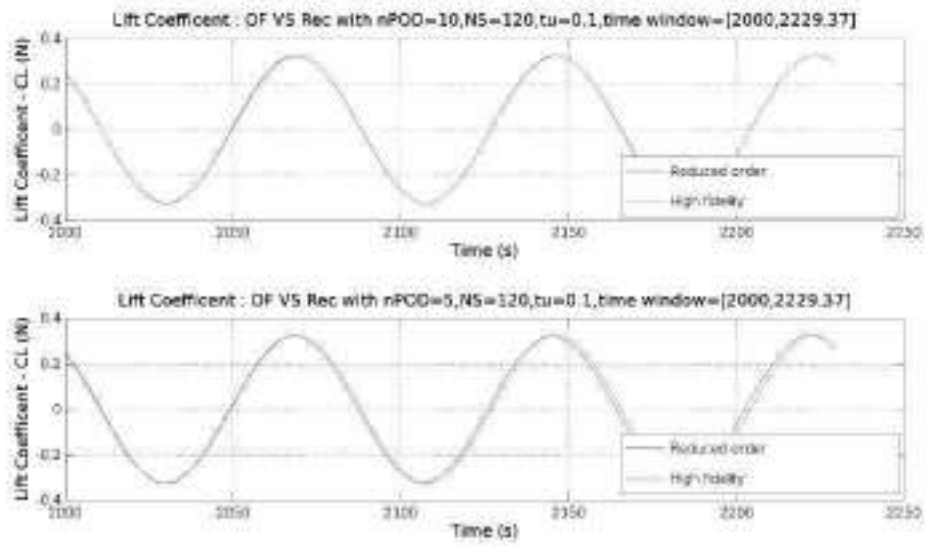


FIGURE 5.6: High fidelity VS ROM lift coefficient for $Re=100$ with different number of modes with same value of penalty factor $\tau = 0.1$ and same number of snapshots which is 120, in red it is the high fidelity solution and in blue it is the ROM solution

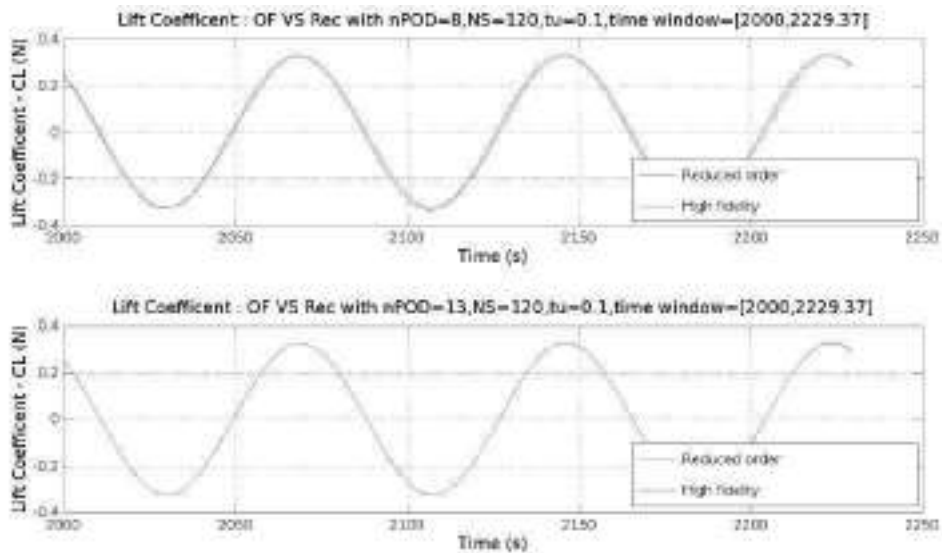
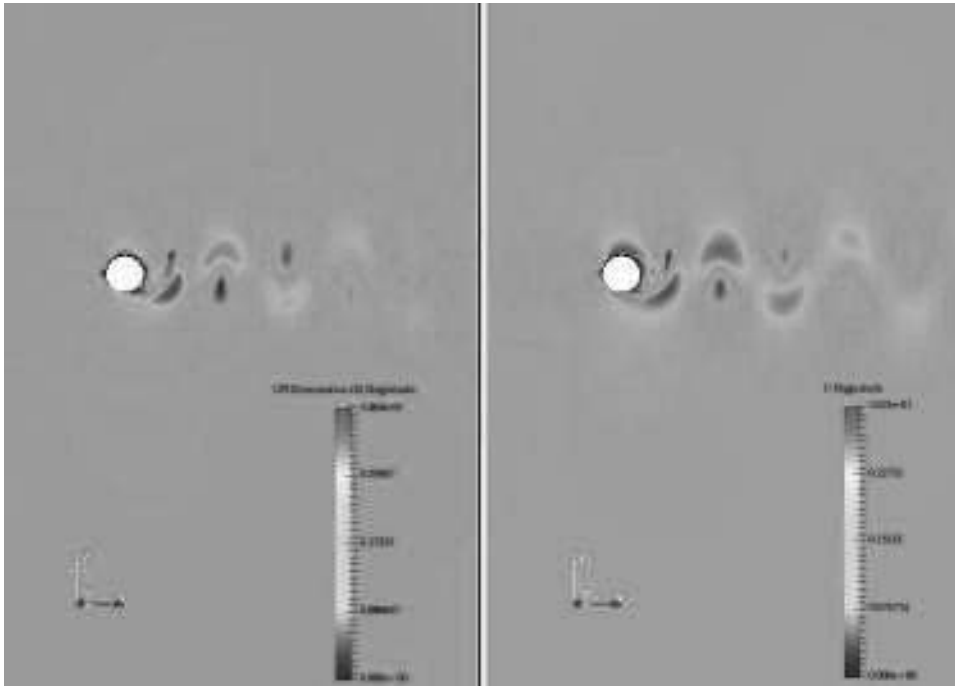


FIGURE 5.7: High fidelity VS ROM lift coefficient for $Re=100$ with different number of modes with same value of penalty factor $\tau = 0.1$ and same number of snapshots which is 120, in red it is the high fidelity solution and in blue it is the ROM solution

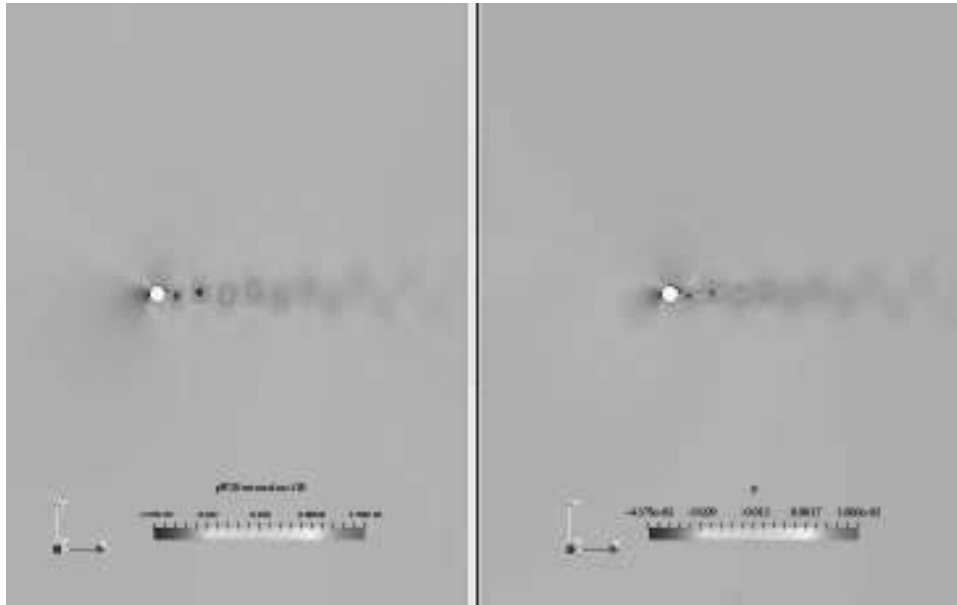


(A) Comparison between velocity fields for the case of a fixed cylinder immersed in flow at $Re=60000$ at time=82, on the right it is the high fidelity one and on the left it is the ROM one

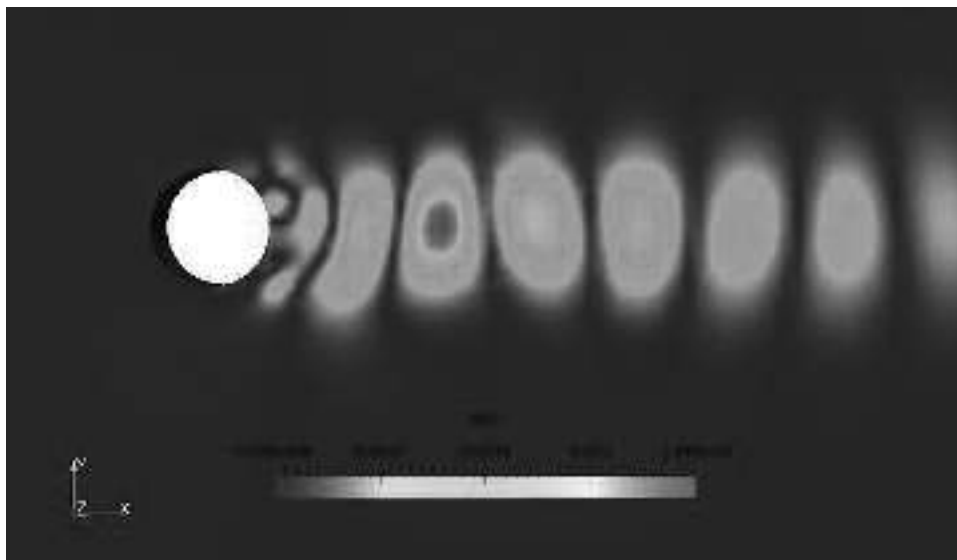


(B) The error difference between HF and ROM velocity for the case of a fixed cylinder immersed in flow at $Re=6000$ at time=82

FIGURE 5.8: Comparison between velocity fields for the case of a fixed cylinder immersed in flow at $Re=6000$ at time=82 with the error being the magnitude of the difference divided by the L^2 -norm



(A) Comparison between pressure fields for the case of the cylinder immersed in flow at $Re=100$ at time=2229.37, on the right it is the high fidelity one and on the left it is the ROM one



(B) The error difference between HF and ROM pressure for the case of the cylinder immersed in flow at $Re=100$ at time=2229.37

FIGURE 5.9: Comparison between pressure fields for the case of the cylinder immersed in flow at $Re=100$ at time=2229.37 with the error being the absolute value of the difference divided by the L^2 -norm

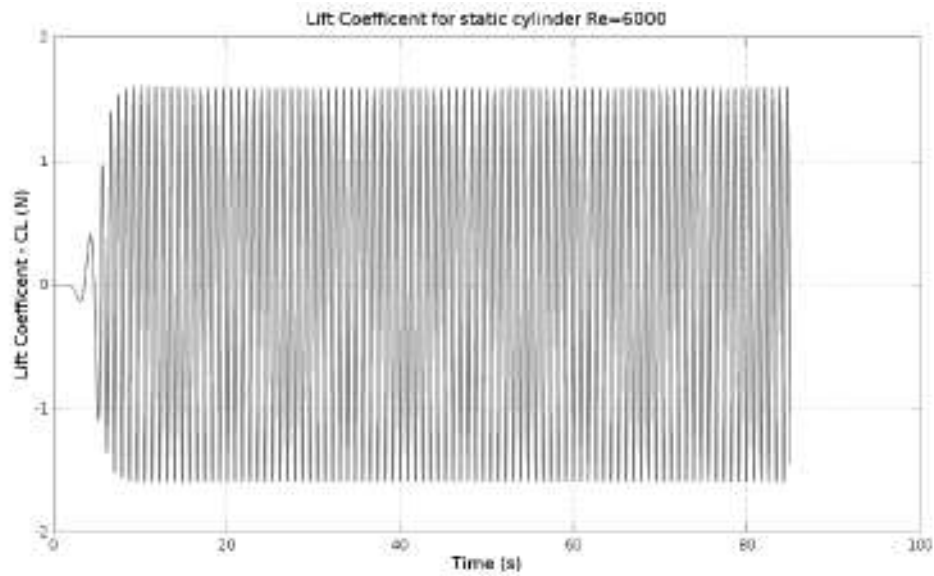


FIGURE 5.10: Lift coefficient for a fixed cylinder immersed in a horizontal stream with $Re=6000$.

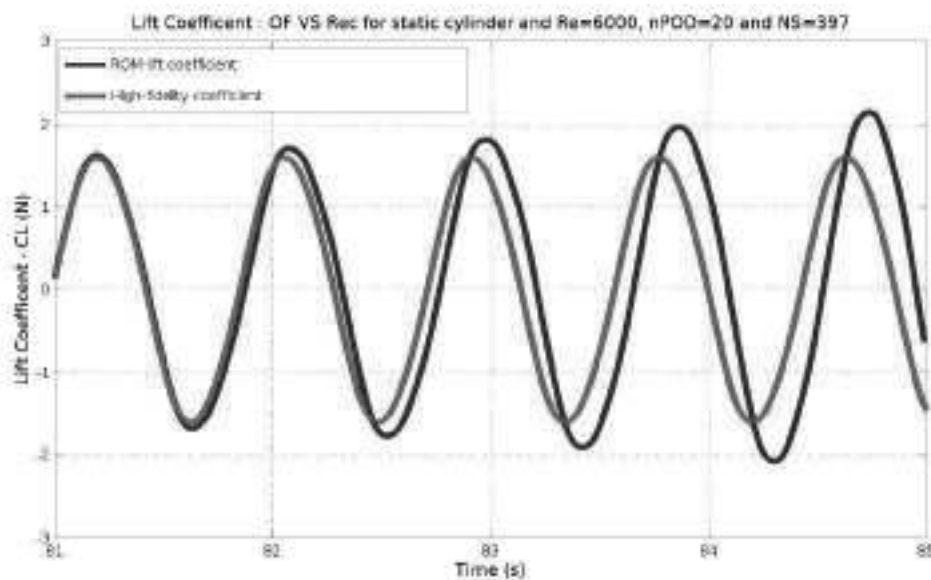


FIGURE 5.11: High fidelity VS ROM lift coefficient for a fixed cylinder immersed in a horizontal stream with $Re=6000$. ROM has been done with 20 modes with penalty factor $\tau = 0$ and number of snapshots of 397 taken in four periods.

of the turbulence variable model parameters k and ω and the solution of the corresponding reduced version of the transport-diffusion equations. If this proved effective in the Lid-Driven Cavity case, presented in such work, it might not be effective in our cylinder case. Thus, we will further investigate if a proper set up of the procedure (in terms of snapshots and mode numbers) will improve the results. In addition, we will test a more conventional procedure in which we take snapshots for both turbulence variables.

Now we have proceed with our ROM methodology applied to the case of cylinder immersed in flow. Yet so far here we were only able to reconstruct the results of the high fidelity simulations. Ideally, we would like to use our numerical machinery to gather information from few high fidelity simulations, and use such information to predict the system behavior for other simulations on different test cases. Thus, we want to combine snapshots from simulations having different inlet velocities. We have considered the laminar case and we combined the snapshots from inlet flow velocities corresponding to Reynolds numbers 100, 125, 150, 175 and 200. In this case we have collected 160 snapshots from each simulation, taking into account that those snapshots cover at least two periods so around 80 snapshots/period. Snapshots have been collected from different time windows, and they have been put together as an input for the POD-FV-ROM procedure previously discussed. The initial conditions used for the inlet velocity corresponds to $Re = 125$, and we aimed to recover the lift coefficient for the same case. So we set $\tau = 0.1$ and $\mathbf{u}_{BC} = 0.0037$ in 4.49 and we solved the dynamical system to obtain ROM velocity and pressure, then we got the reconstructed lift coefficient from the ROM procedure that is depicted in 5.12. As you can see we have data for the full order lift coefficient in the period from $t = 1400$ to $t = 1382.89$ and in that period the recovered solution from ROM is close to the OpenFOAM one but then we simulated for later time and we see that the solution has been damped. Now if we looked to the amplitude spectrum of the ROM lift coefficient we see from figure 5.13 that the the maximum peak occurs at frequency of 0.018311 Hz which correspond to period of 54.613 seconds while the high order solution has period of 58 seconds. In general, we can say that we have to treat the initial conditions in different way and it is also important to think about another way of formulating the boundary conditions in the POD-FV-ROM 4.49.

5.2 Conclusions and future work

With high fidelity simulations, we have been able to partially capture hysteresis phenomenons that occur in the flow past a circular cylinder, for which we have been able to reproduce the benchmark results for Khalak and Williamson. For our work in ROM, we could obtain good results for recovering the original numerical full order solution by applying FV-ROM procedure in the case of laminar flows. Regarding turbulent flows, we have good results in the first period of the lift coefficient but then the our solution has started to diverge. When we mixed more than one velocity together to obtain the model shape, we could not obtain suitable results for the lift coefficient. Probably the reason is related to the way of formulating the boundary conditions in our FV-ROM approach, and to the procedure

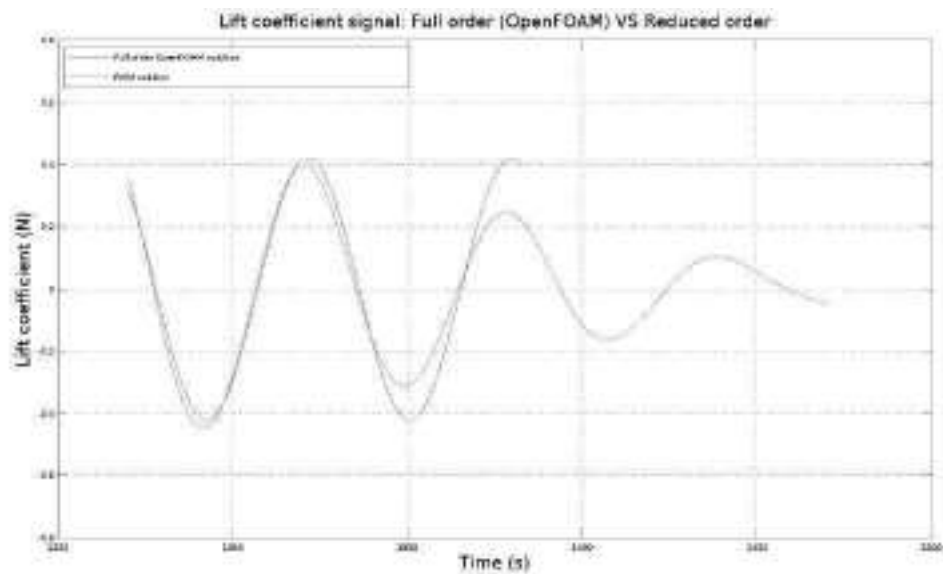


FIGURE 5.12: Lift coefficient for a cylinder immersed in a horizontal stream with $Re=125$ (in blue) VS the reduced order lift coefficient (in red) for the same horizontal stream reconstructed from a mix of simulation data from five different velocities correspond to $Re=100,125,150,175$ and 200

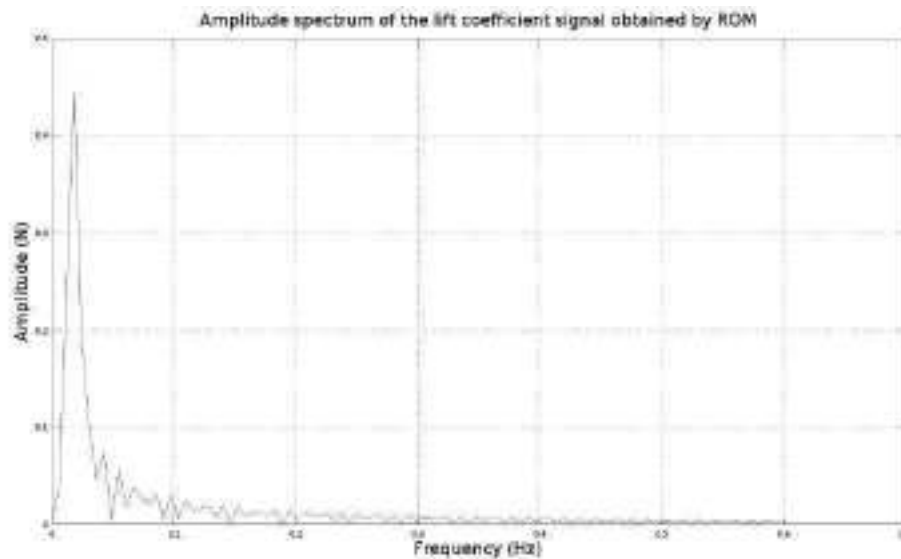


FIGURE 5.13: Amplitude spectrum of the lift coefficient signal obtained by ROM when snapshots used from five different simulations, where in ROM a velocity corresponds to $Re=125$ has been sought

used to set the initial conditions in the ROM dynamical system for the time dependent coefficients.

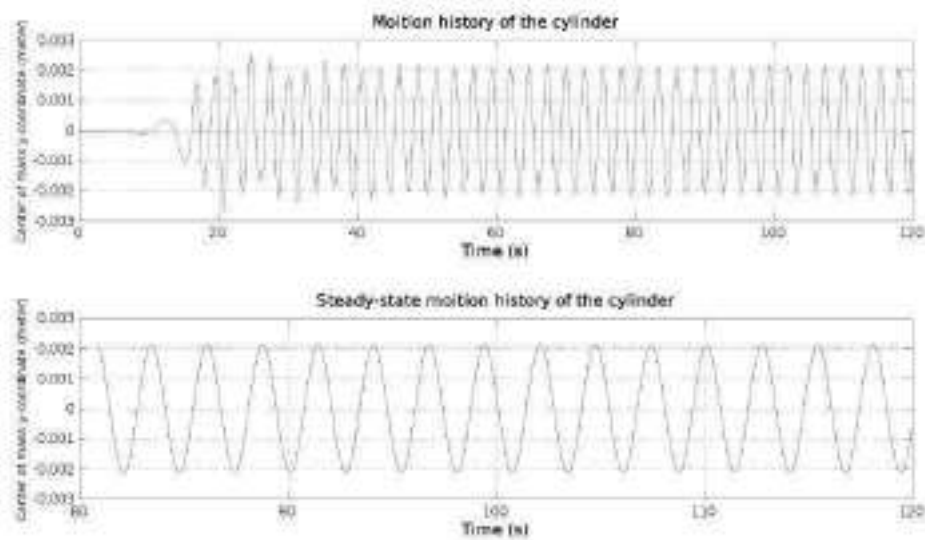
We think that it would be possible to improve our implementation of the FV-ROM in order to build more accurate reduced order model. To do so, a possibility is to resort to a different way of formulating the boundary conditions with respect to the current penalizing strategy which requires sensitivity analysis to determine a suitable value of τ . Also, we could think about describing the reduced order solution for pressure with different time dependent coefficients instead of using the same one for the velocity. Another improvement could come from using the procedure of [5] where the approach includes merging the continuity equation with momentum equation in one equation with a scaling factor for the divergence operator of the velocity. In addition, we recommend adopting procedure of supermizer pressure stabilization so that we can get better results for pressure for details [3, 49].

Our goal for future studies of ROM applied to FSI problems is to be able to catch the hysteresis using the reduced order modelling. We think that this would be possible after taking into consideration the aforementioned improvements to our POD-FV-ROM approach.

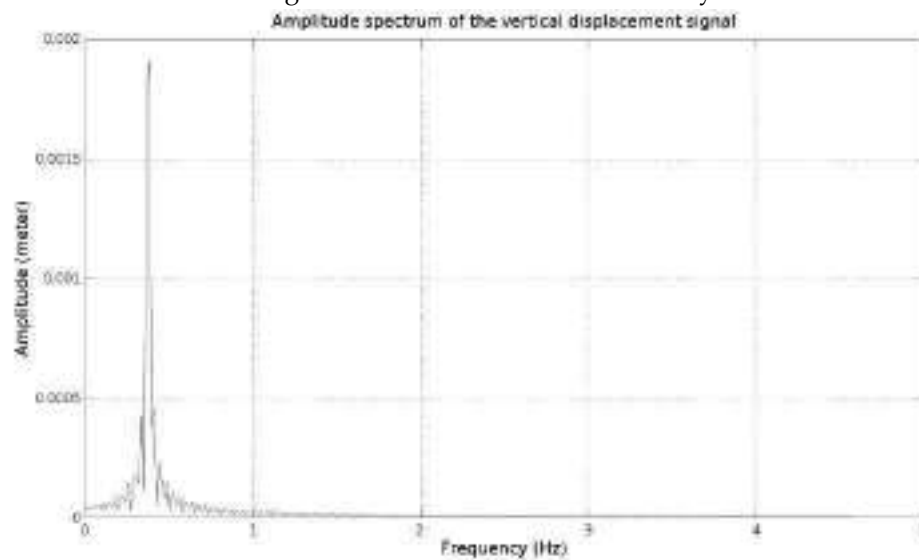
Appendix A

Simulation results for the full order problem

Here we present all the high fidelity test cases used to produce plots 3.8 and 3.9.

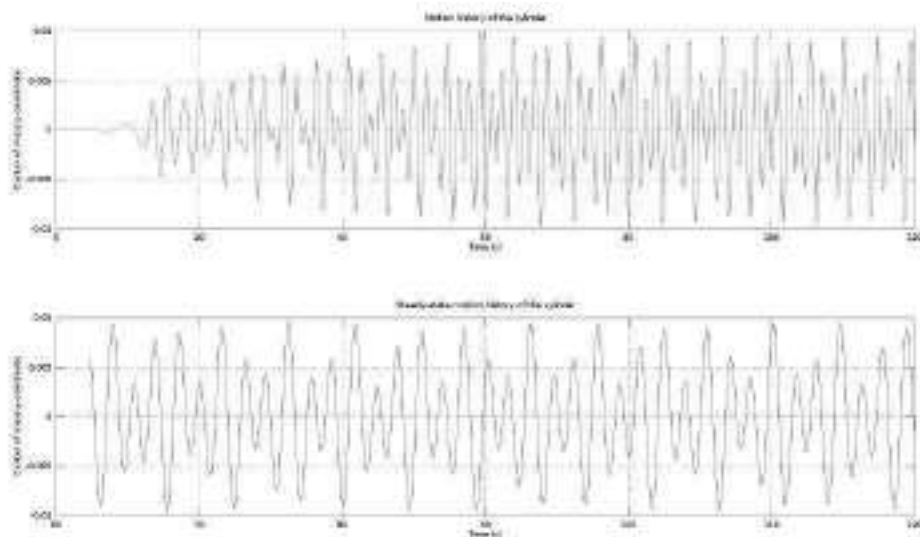


(A) The top plot represent the time history of a vertical displacement of a cylinder immersed in a horizontal stream with $Re=2000$. In the bottom plot we report the final regime solution used for Fourier analysis

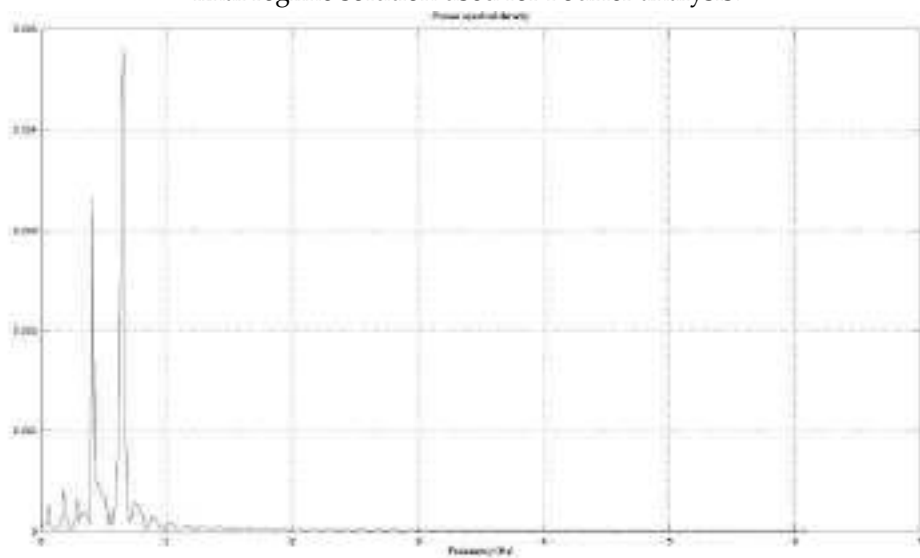


(B) Amplitude spectrum of the vertical displacement signal (see figure A) for a cylinder immersed in horizontal stream at $Re=2000$.

FIGURE A.1: Results for a cylinder immersed in horizontal stream at $Re=2000$

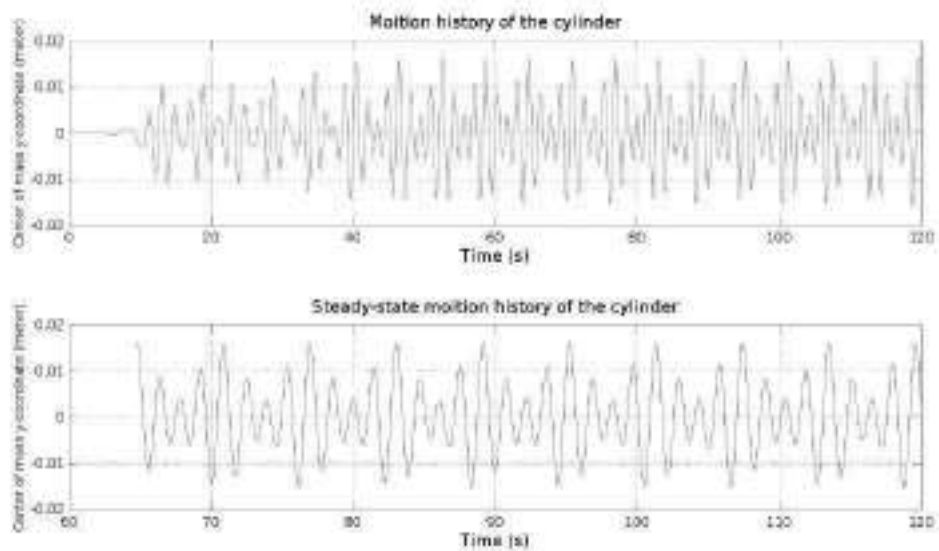


(A) The top plot represent the time history of a vertical displacement of a cylinder immersed in a horizontal stream with $Re=2500$. In the bottom plot we report the final regime solution used for Fourier analysis.

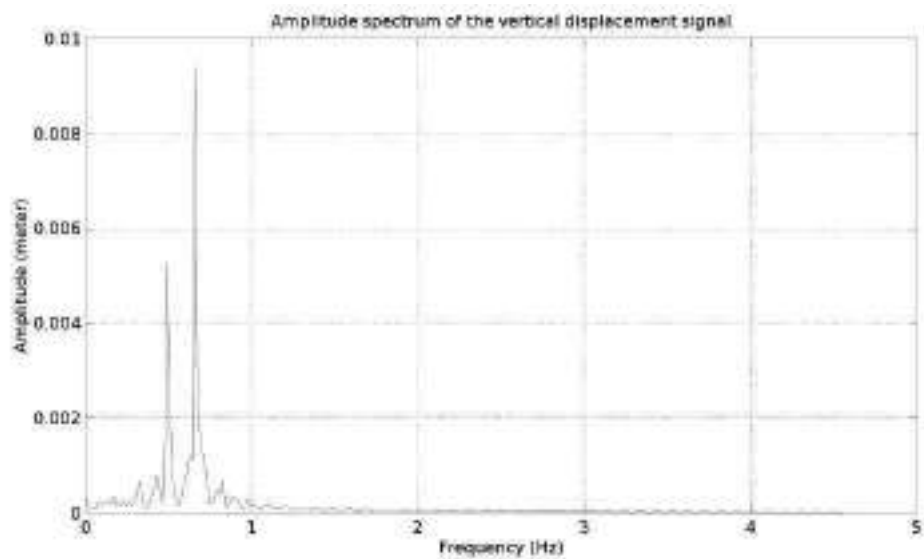


(B) Amplitude spectrum of the vertical displacement signal (see figure A) for a cylinder immersed in horizontal stream at $Re=2500$.

FIGURE A.2: Results for a cylinder immersed in horizontal stream at $Re=2500$

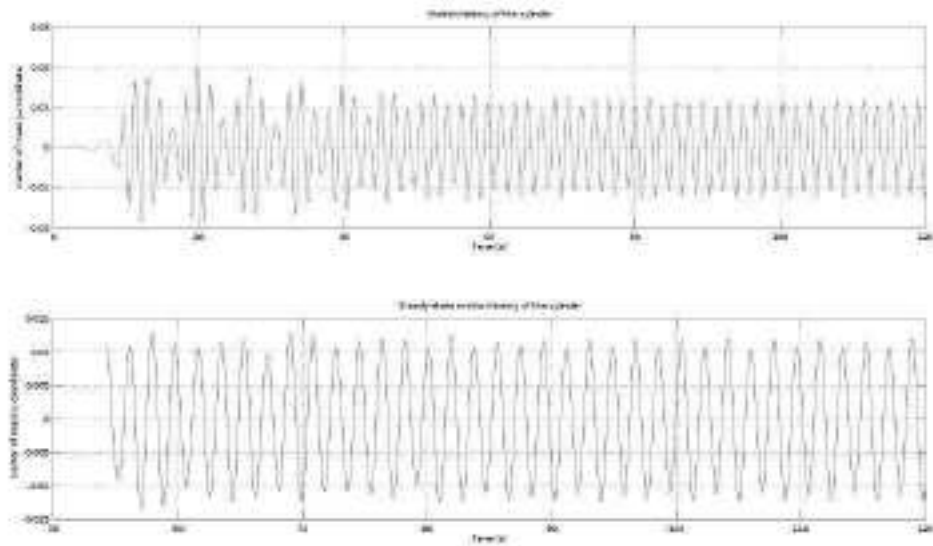


(A) The top plot represent the time history of a vertical displacement of a cylinder immersed in a horizontal stream with $Re=3000$. In the bottom plot we report the final regime solution used for Fourier analysis.

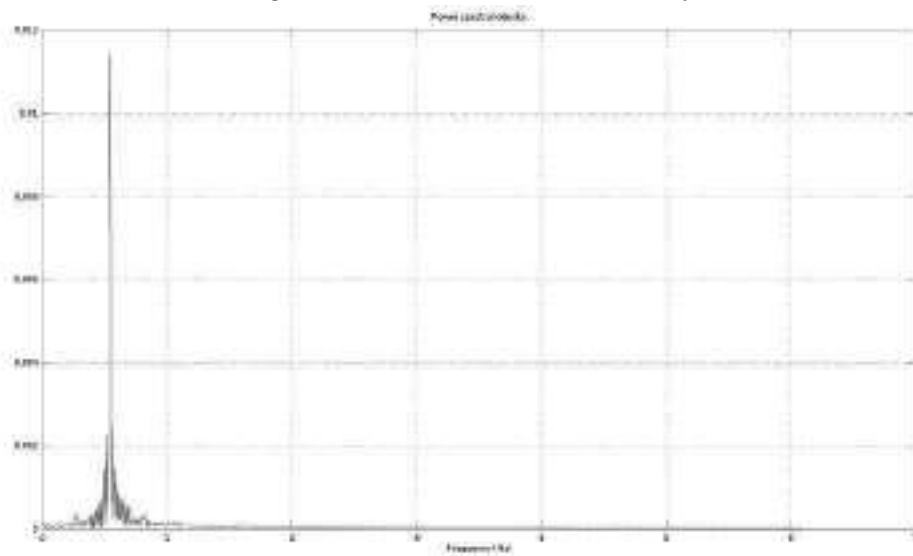


(B) Amplitude spectrum of the vertical displacement signal (see figure A) for a cylinder immersed in horizontal stream at $Re=3000$.

FIGURE A.3: Results for a cylinder immersed in horizontal stream at $Re=3000$

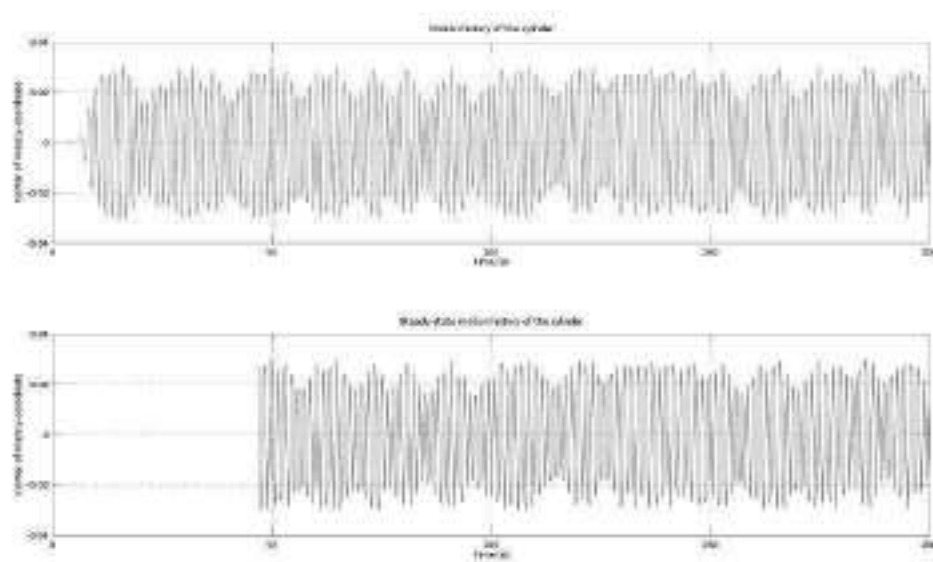


(A) The top plot represent the time history of a vertical displacement of a cylinder immersed in a horizontal stream with $Re=3500$. In the bottom plot we report the final regime solution used for Fourier analysis.

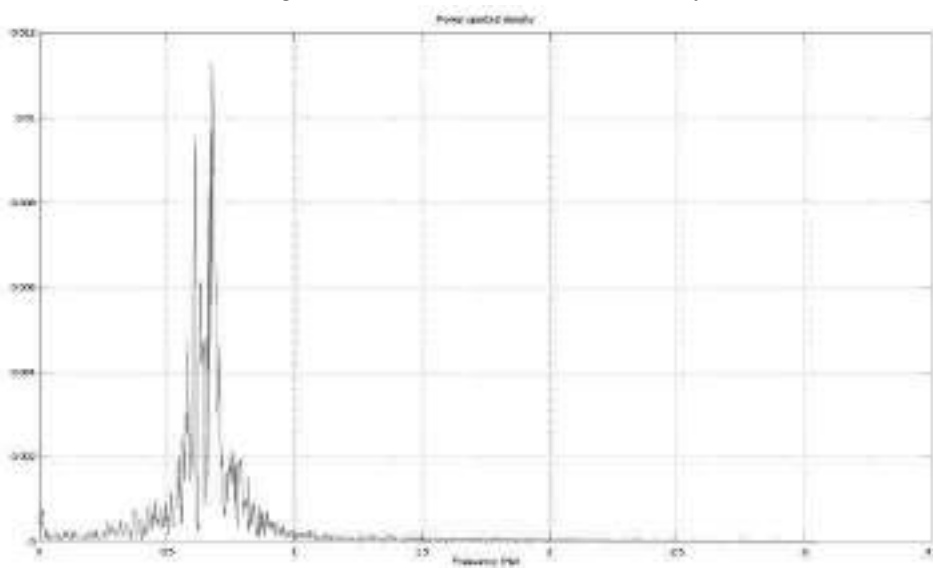


(B) Amplitude spectrum of the vertical displacement signal (see figure A) for a cylinder immersed in horizontal stream at $Re=3500$.

FIGURE A.4: Results for a cylinder immersed in horizontal stream at $Re=3500$

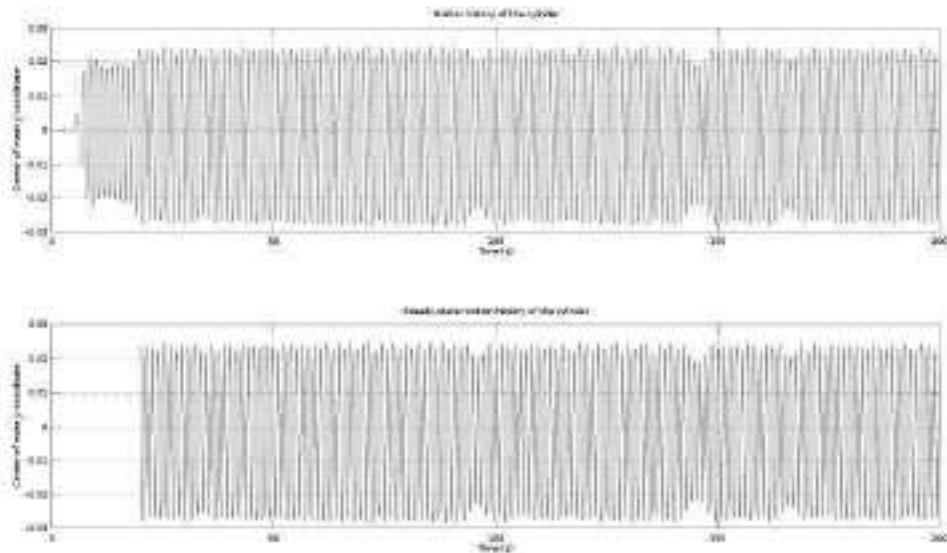


(A) The top plot represent the time history of a vertical displacement of a cylinder immersed in a horizontal stream with $Re=4000$. In the bottom plot we report the final regime solution used for Fourier analysis.

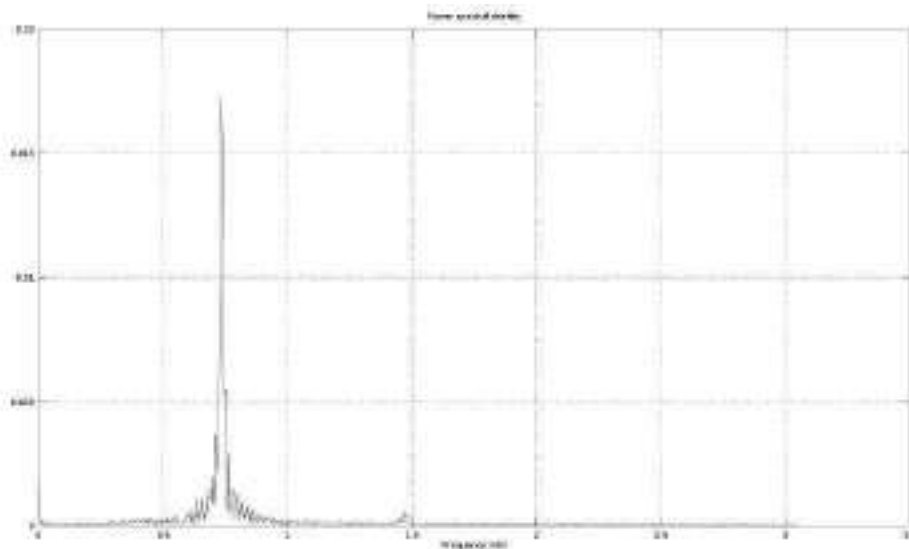


(B) Amplitude spectrum of the vertical displacement signal (see figure A) for a cylinder immersed in horizontal stream at $Re=4000$.

FIGURE A.5: Results for a cylinder immersed in horizontal stream at $Re=4000$

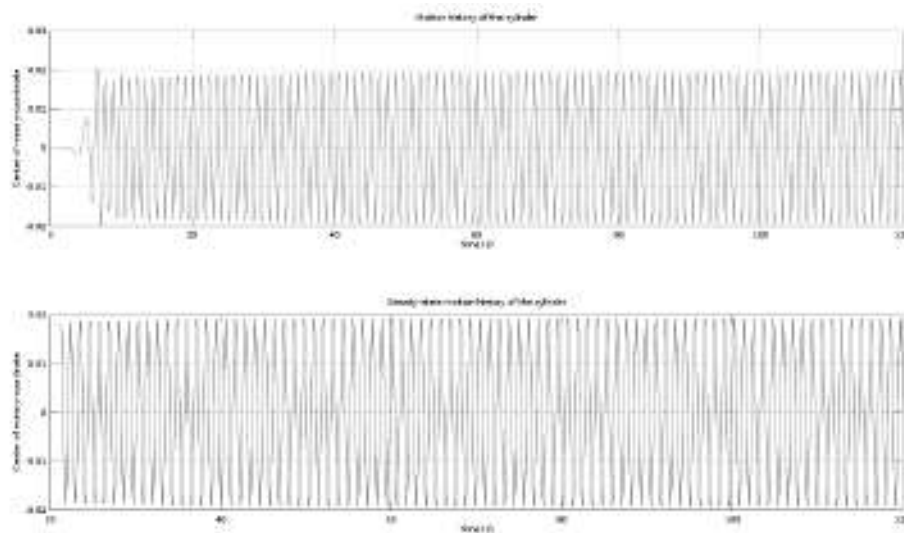


(A) The top plot represent the time history of a vertical displacement of a cylinder immersed in a horizontal stream with $Re=4500$. In the bottom plot we report the final regime solution used for Fourier analysis.

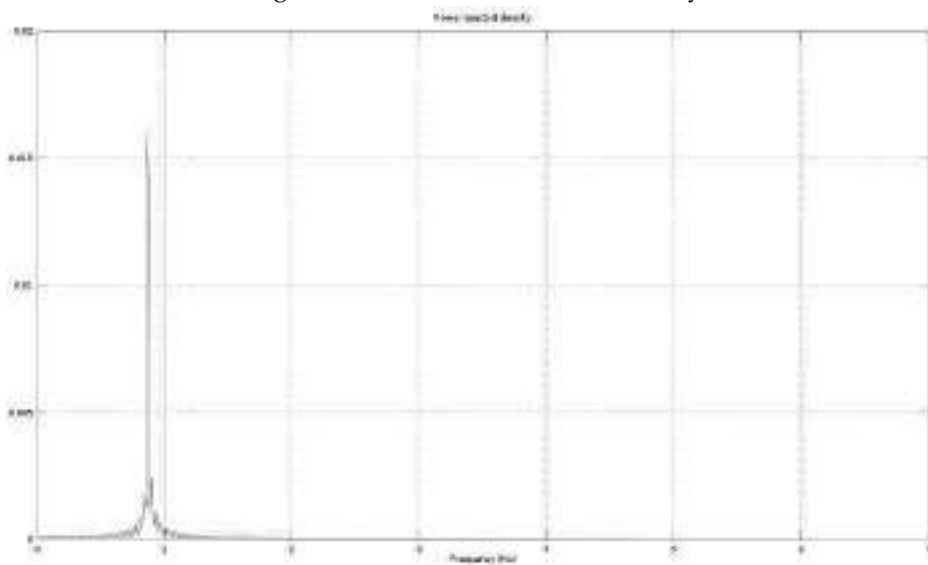


(B) Amplitude spectrum of the vertical displacement signal (see figure A) for a cylinder immersed in horizontal stream at $Re=4500$.

FIGURE A.6: Results for a cylinder immersed in horizontal stream at $Re=4500$

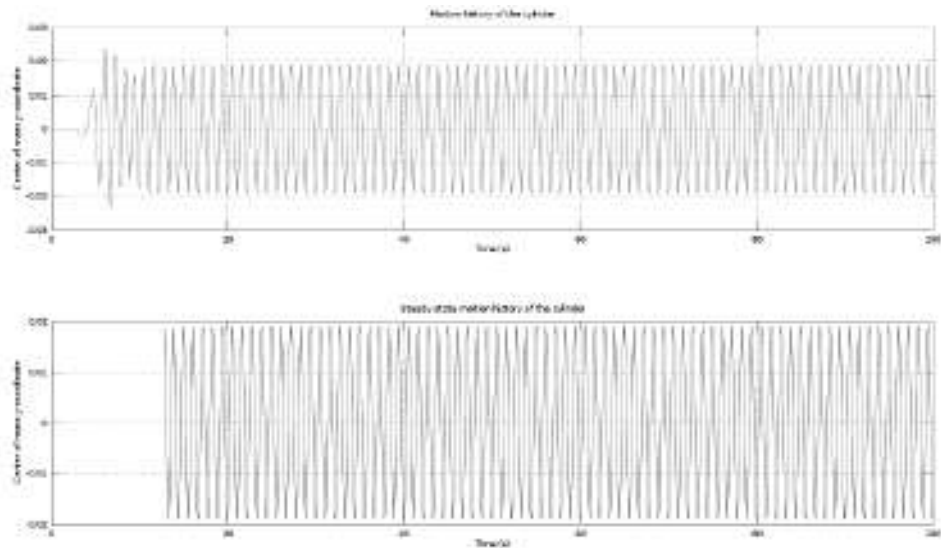


(A) The top plot represent the time history of a vertical displacement of a cylinder immersed in a horizontal stream with $Re=5000$. In the bottom plot we report the final regime solution used for Fourier analysis.

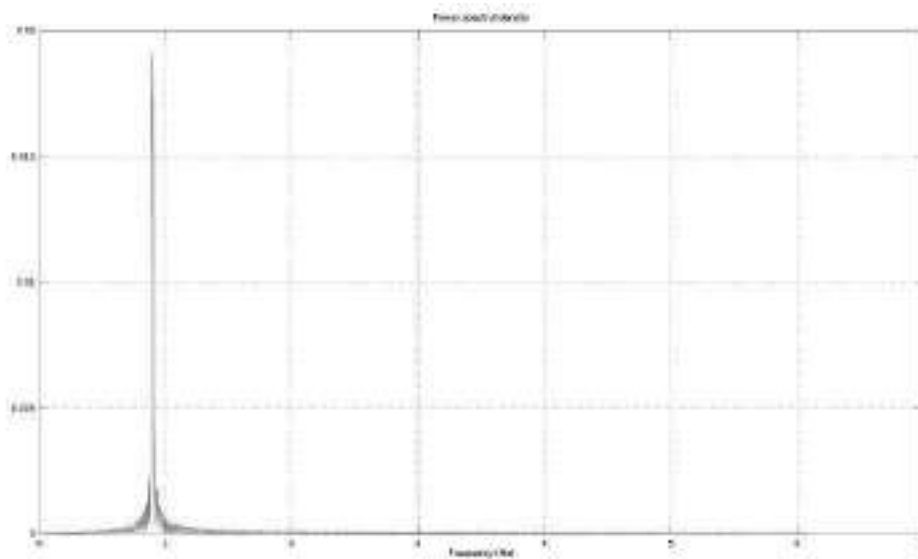


(B) Amplitude spectrum of the vertical displacement signal (see figure A) for a cylinder immersed in horizontal stream at $Re=5000$.

FIGURE A.7: Results for a cylinder immersed in horizontal stream at $Re=5000$

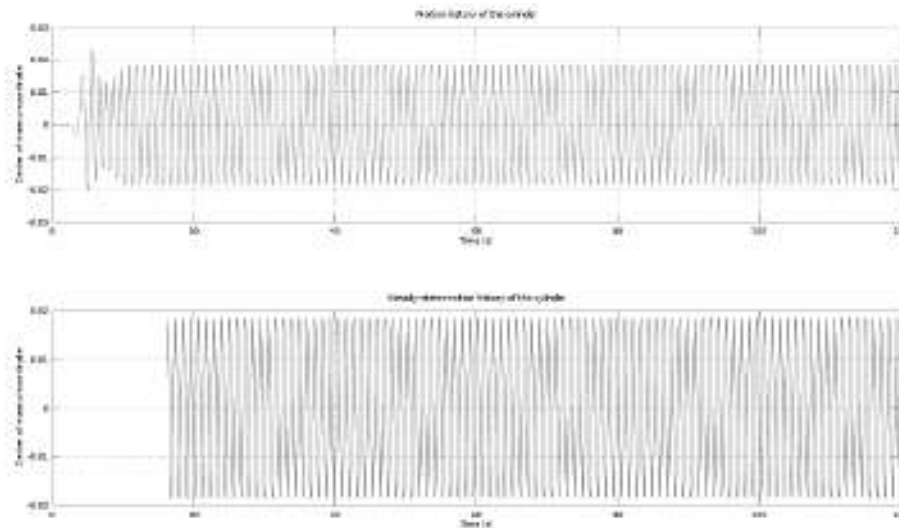


(A) The top plot represent the time history of a vertical displacement of a cylinder immersed in a horizontal stream with $Re=5500$. In the bottom plot we report the final regime solution used for Fourier analysis.

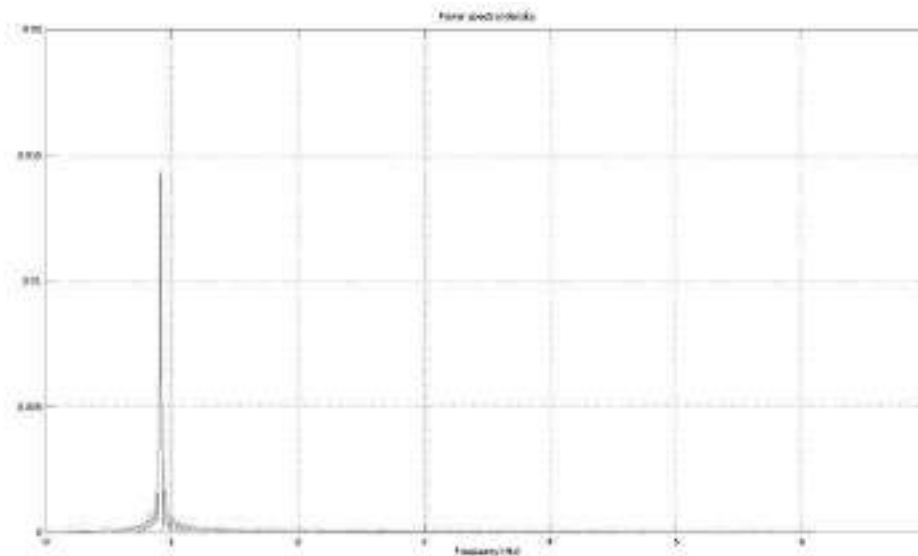


(B) Amplitude spectrum of the vertical displacement signal (see figure A) for a cylinder immersed in horizontal stream at $Re=5500$.

FIGURE A.8: Results for a cylinder immersed in horizontal stream at $Re=5500$

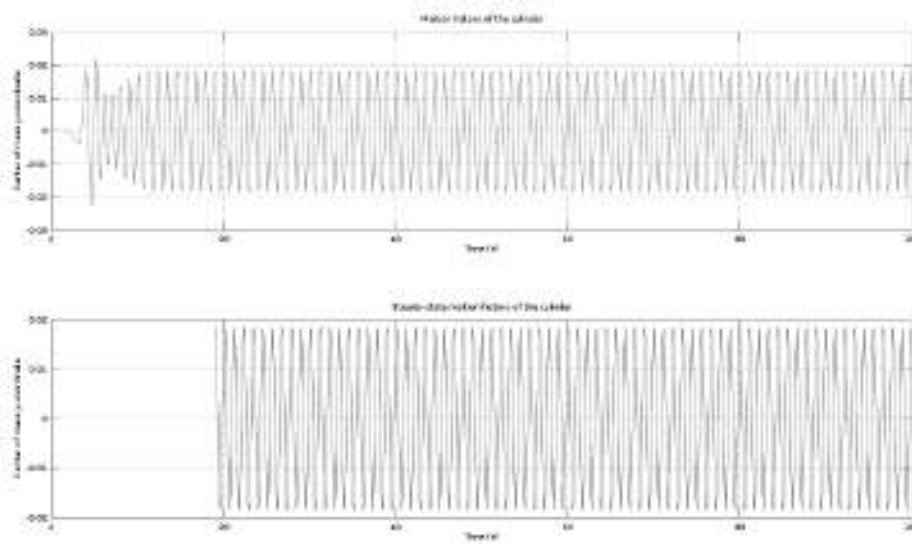


(A) The top plot represent the time history of a vertical displacement of a cylinder immersed in a horizontal stream with $Re=6000$. In the bottom plot we report the final regime solution used for Fourier analysis.

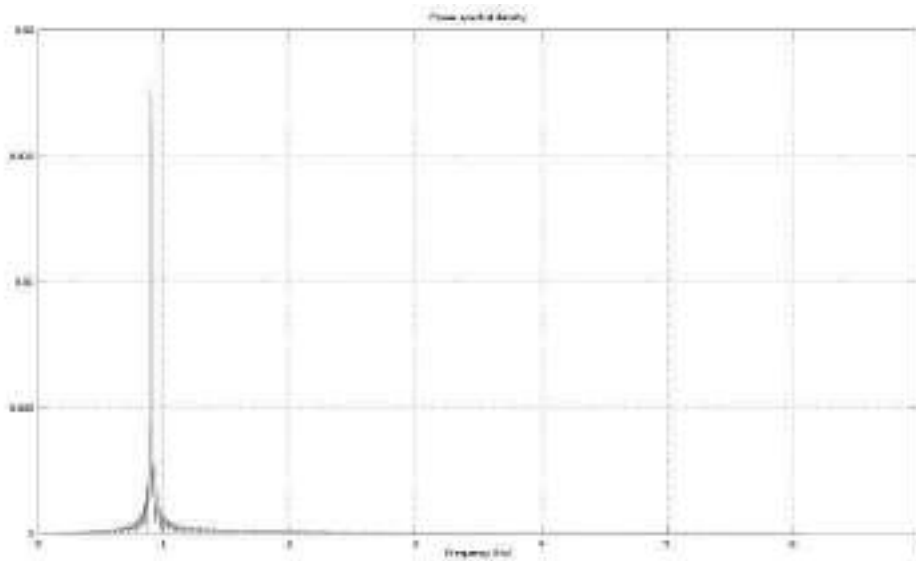


(B) Amplitude spectrum of the vertical displacement signal (see figure A) for a cylinder immersed in horizontal stream at $Re=6000$.

FIGURE A.9: Results for a cylinder immersed in horizontal stream at $Re=6000$

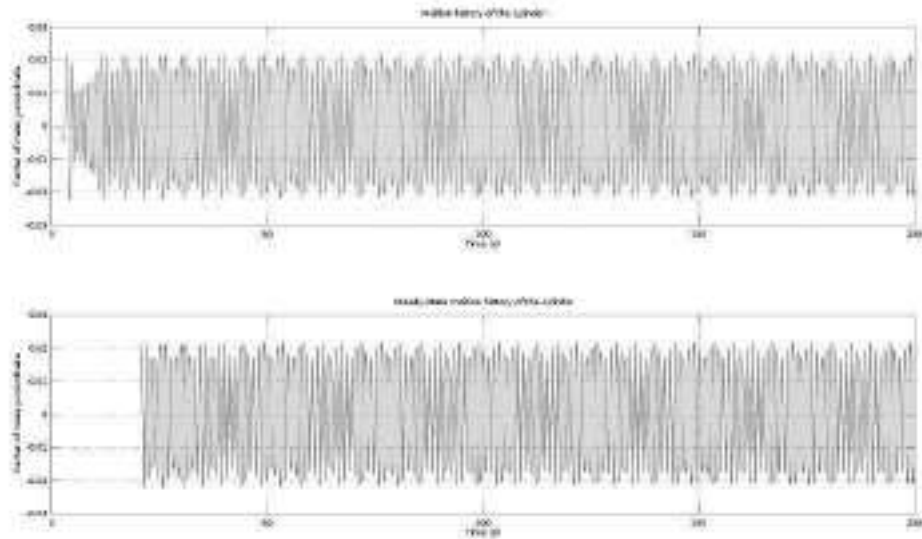


(A) The top plot represent the time history of a vertical displacement of a cylinder immersed in a horizontal stream with $Re=6500$. In the bottom plot we report the final regime solution used for Fourier analysis.

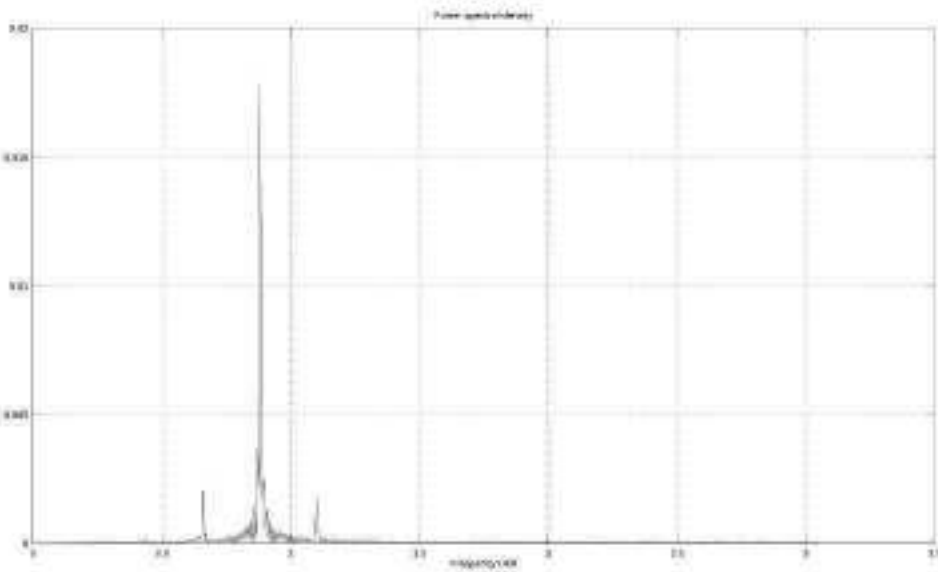


(B) Amplitude spectrum of the vertical displacement signal (see figure A) for a cylinder immersed in horizontal stream at $Re=6500$.

FIGURE A.10: Results for a cylinder immersed in horizontal stream at $Re=6500$

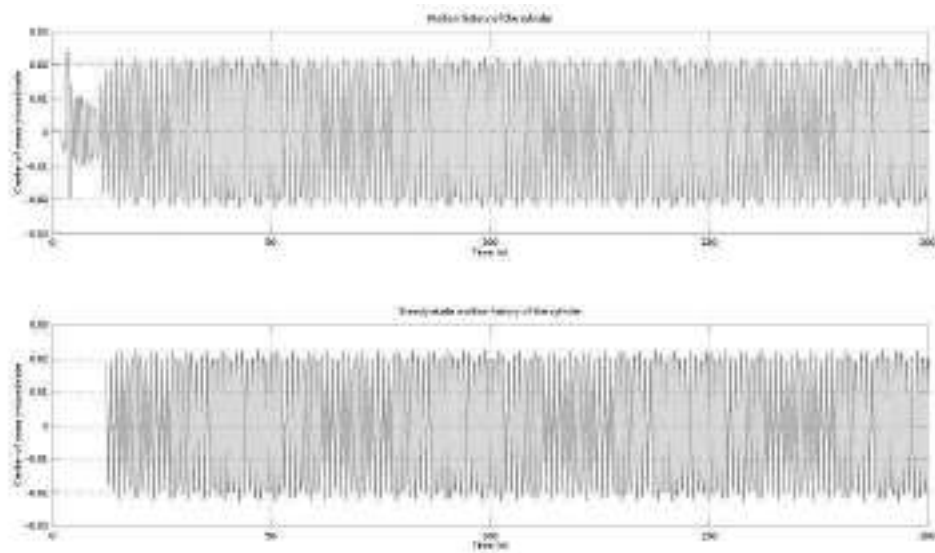


(A) The top plot represent the time history of a vertical displacement of a cylinder immersed in a horizontal stream with $Re=7000$. In the bottom plot we report the final regime solution used for Fourier analysis.

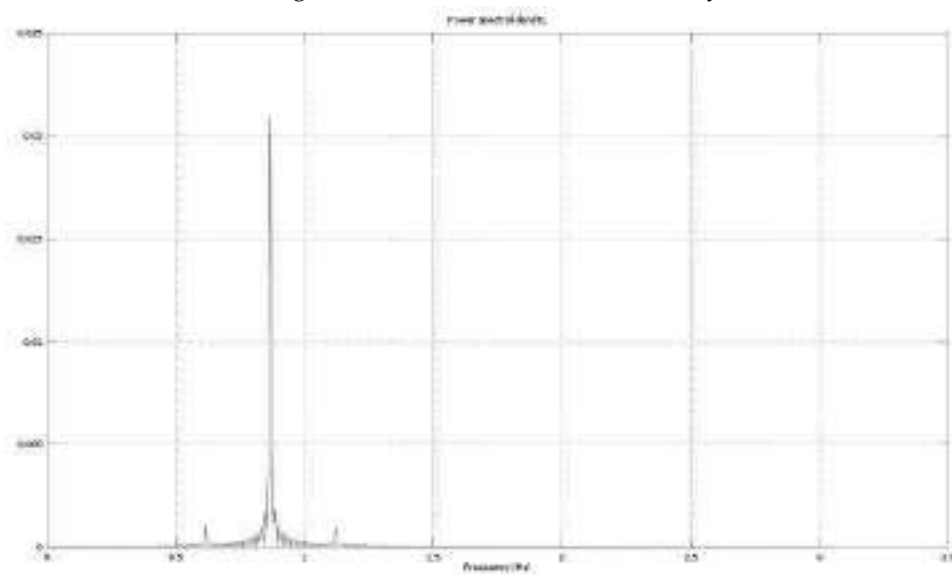


(B) Amplitude spectrum of the vertical displacement signal (see figure A) for a cylinder immersed in horizontal stream at $Re=7000$.

FIGURE A.11: Results for a cylinder immersed in horizontal stream at $Re=7000$

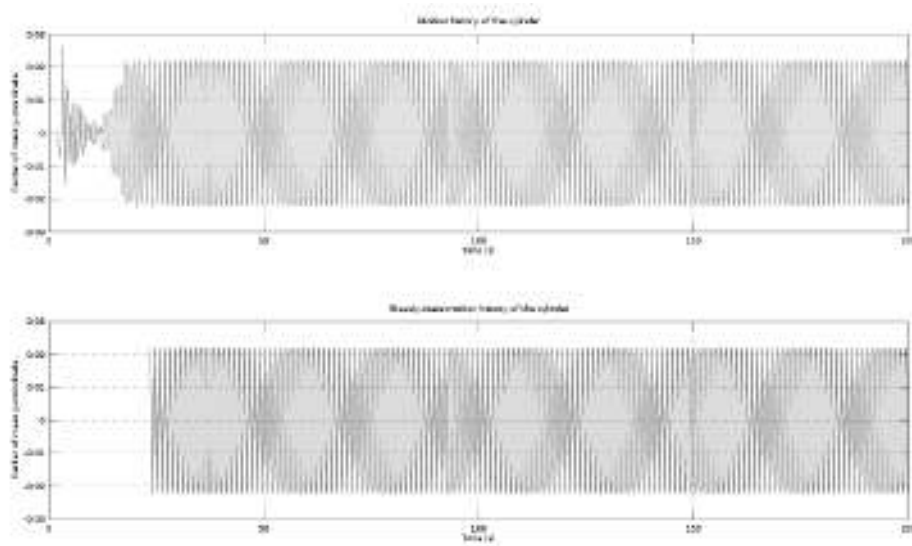


(A) The top plot represent the time history of a vertical displacement of a cylinder immersed in a horizontal stream with $Re=7500$. In the bottom plot we report the final regime solution used for Fourier analysis.

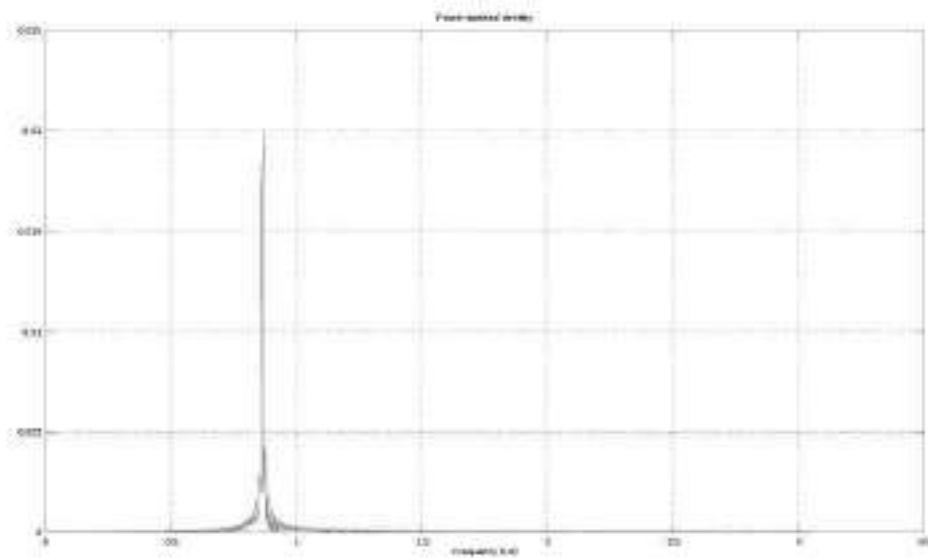


(B) Amplitude spectrum of the vertical displacement signal (see figure A) for a cylinder immersed in horizontal stream at $Re=7500$.

FIGURE A.12: Results for a cylinder immersed in horizontal stream at $Re=7500$

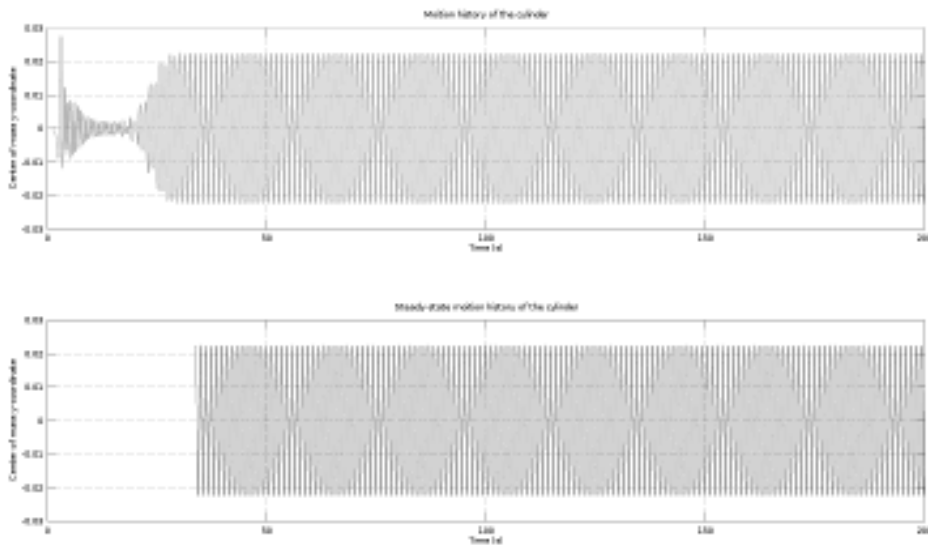


(A) The top plot represent the time history of a vertical displacement of a cylinder immersed in a horizontal stream with $Re=8000$. In the bottom plot we report the final regime solution used for Fourier analysis.

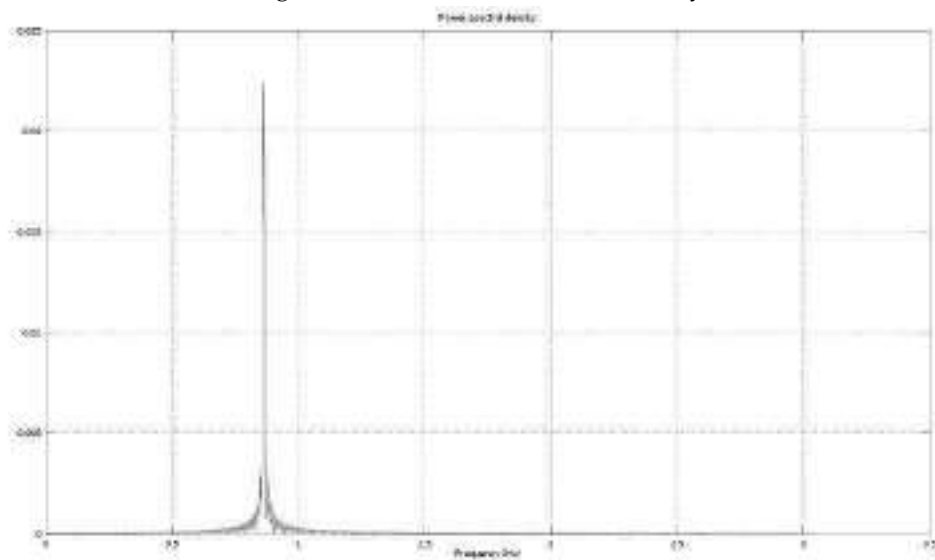


(B) Amplitude spectrum of the vertical displacement signal (see figure A) for a cylinder immersed in horizontal stream at $Re=8000$.

FIGURE A.13: Results for a cylinder immersed in horizontal stream at $Re=8000$

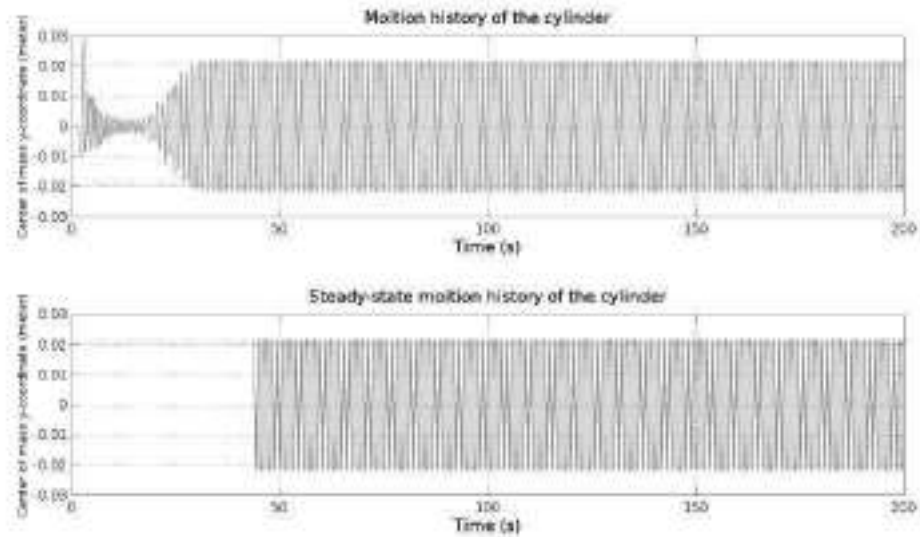


(A) The top plot represent the time history of a vertical displacement of a cylinder immersed in a horizontal stream with $Re=8500$. In the bottom plot we report the final regime solution used for Fourier analysis.

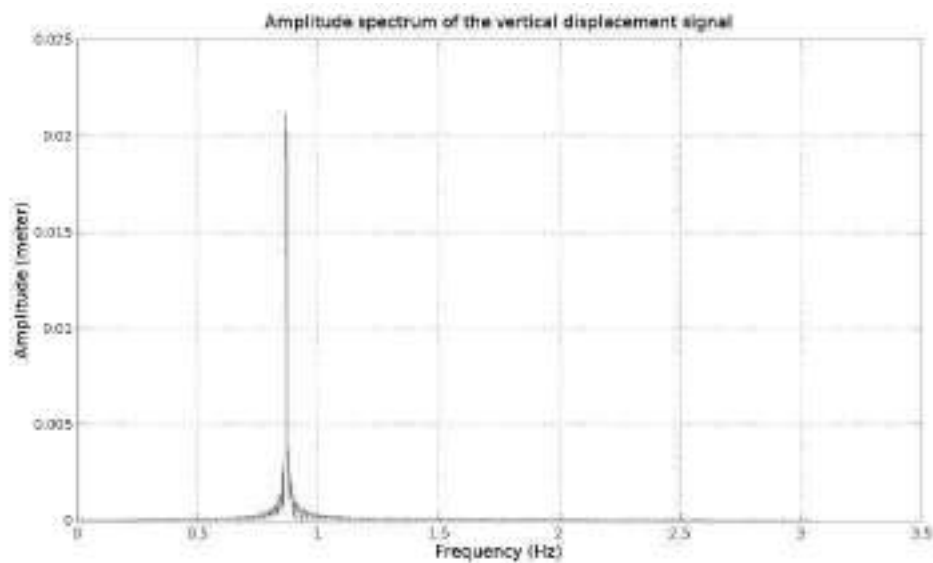


(B) Amplitude spectrum of the vertical displacement signal (see figure A) for a cylinder immersed in horizontal stream at $Re=8500$.

FIGURE A.14: Results for a cylinder immersed in horizontal stream at $Re=8500$

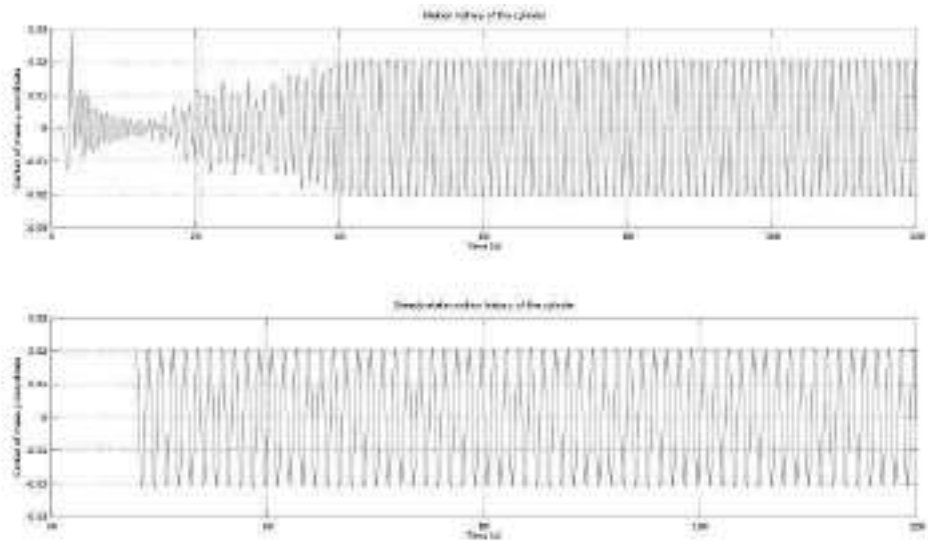


(A) The top plot represent the time history of a vertical displacement of a cylinder immersed in a horizontal stream with $Re=9000$. In the bottom plot we report the final regime solution used for Fourier analysis.

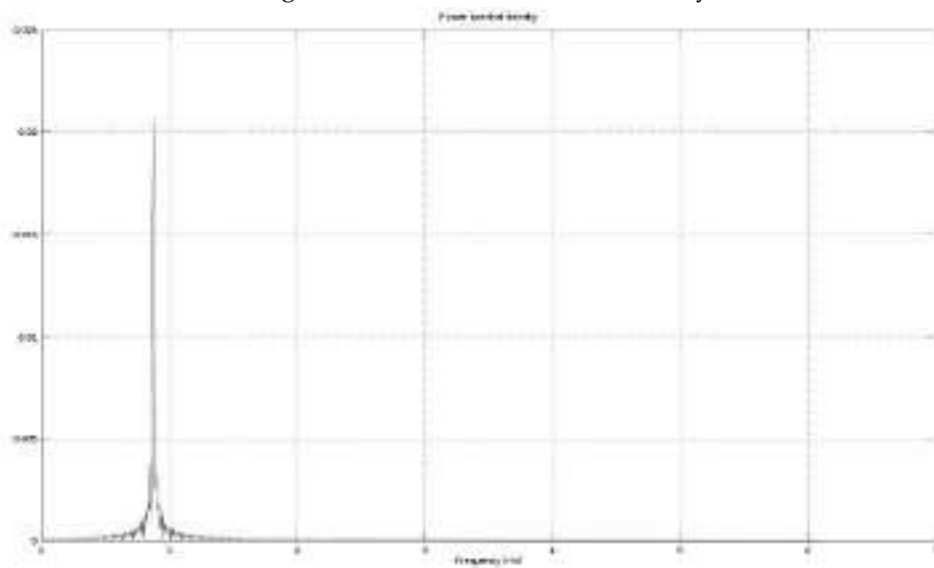


(B) Amplitude spectrum of the vertical displacement signal (see figure A) for a cylinder immersed in horizontal stream at $Re=9000$.

FIGURE A.15: Results for a cylinder immersed in horizontal stream at $Re=9000$

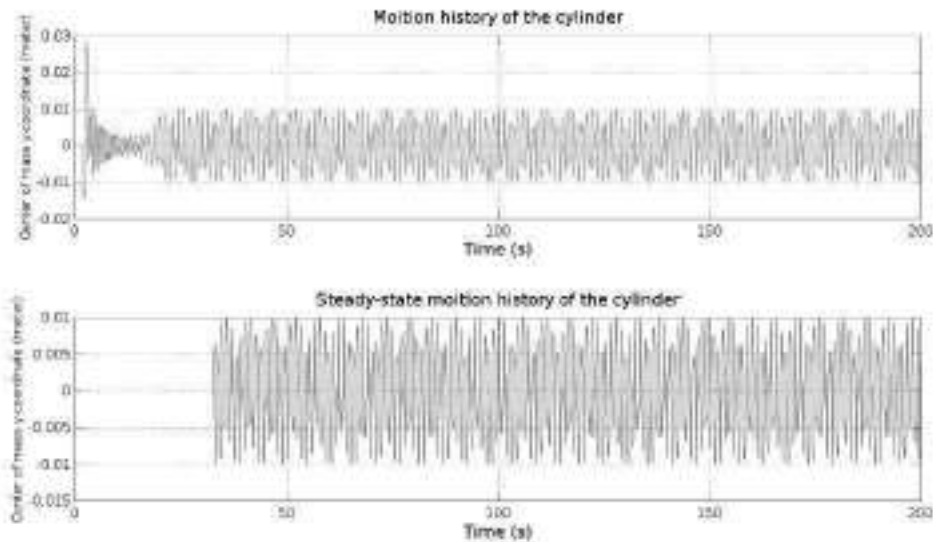


(A) The top plot represent the time history of a vertical displacement of a cylinder immersed in a horizontal stream with $Re=9500$. In the bottom plot we report the final regime solution used for Fourier analysis.

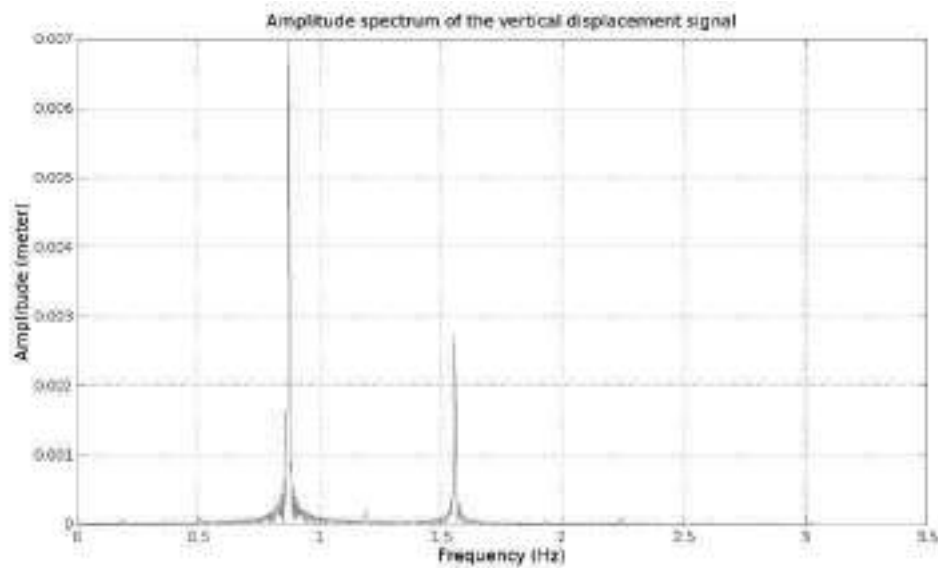


(B) Amplitude spectrum of the vertical displacement signal (see figure A) for a cylinder immersed in horizontal stream at $Re=9500$.

FIGURE A.16: Results for a cylinder immersed in horizontal stream at $Re=9500$

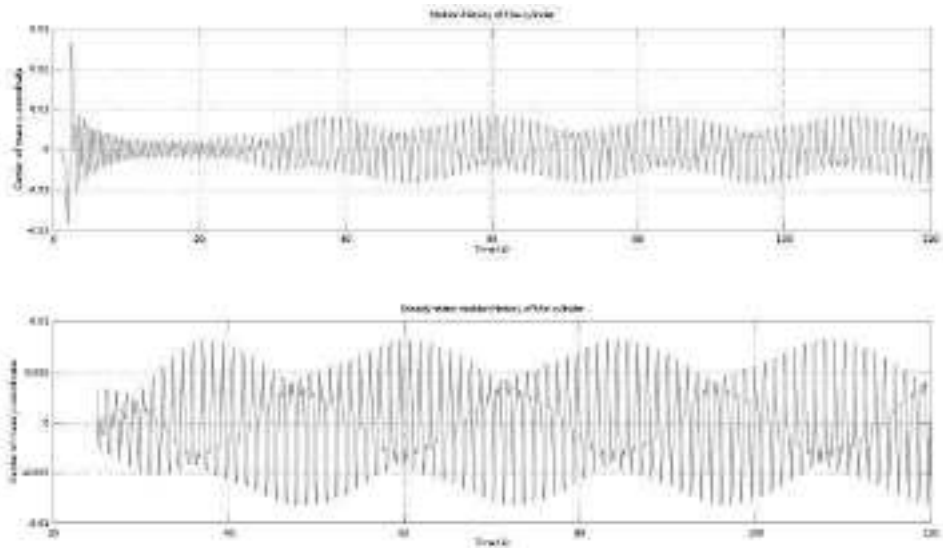


(A) The top plot represent the time history of a vertical displacement of a cylinder immersed in a horizontal stream with $Re=10000$. In the bottom plot we report the final regime solution used for Fourier analysis.

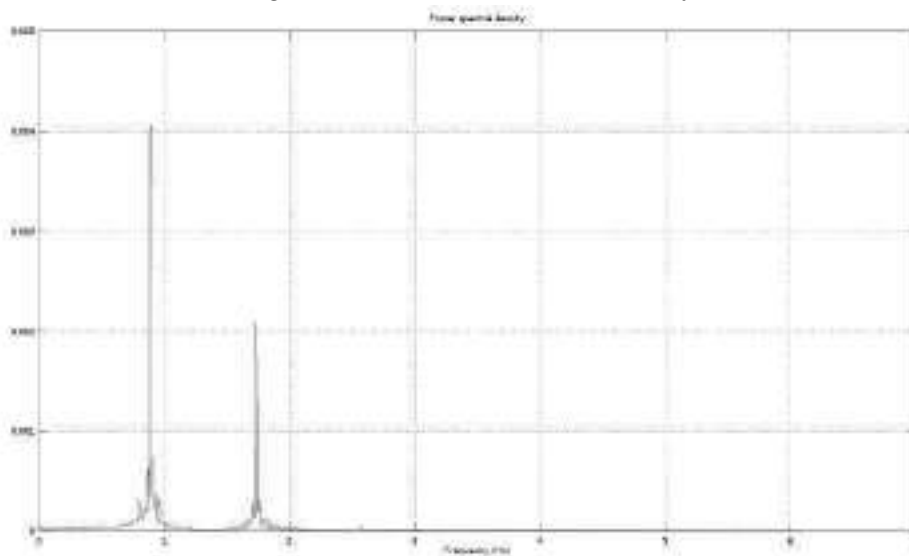


(B) Amplitude spectrum of the vertical displacement signal (see figure A) for a cylinder immersed in horizontal stream at $Re=10000$.

FIGURE A.17: Results for a cylinder immersed in horizontal stream at $Re=10000$

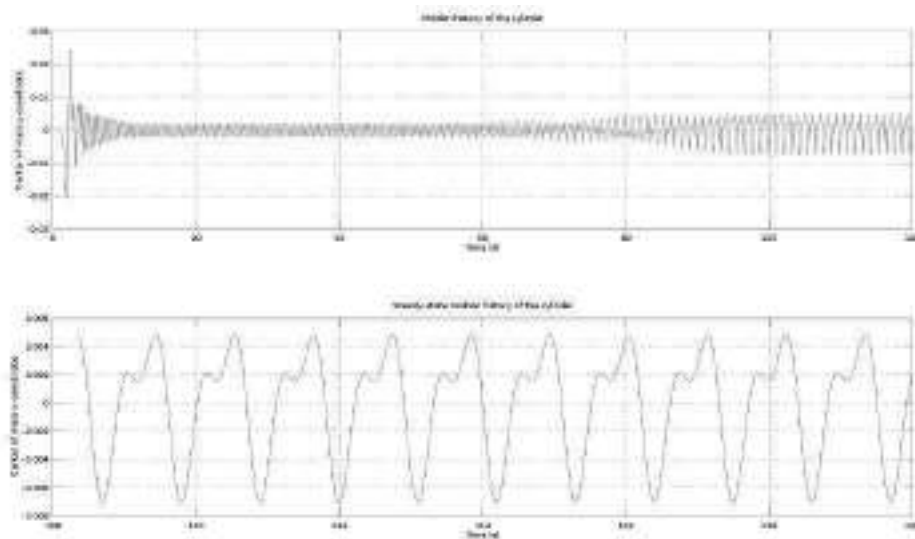


(A) The top plot represent the time history of a vertical displacement of a cylinder immersed in a horizontal stream with $Re=11000$. In the bottom plot we report the final regime solution used for Fourier analysis.

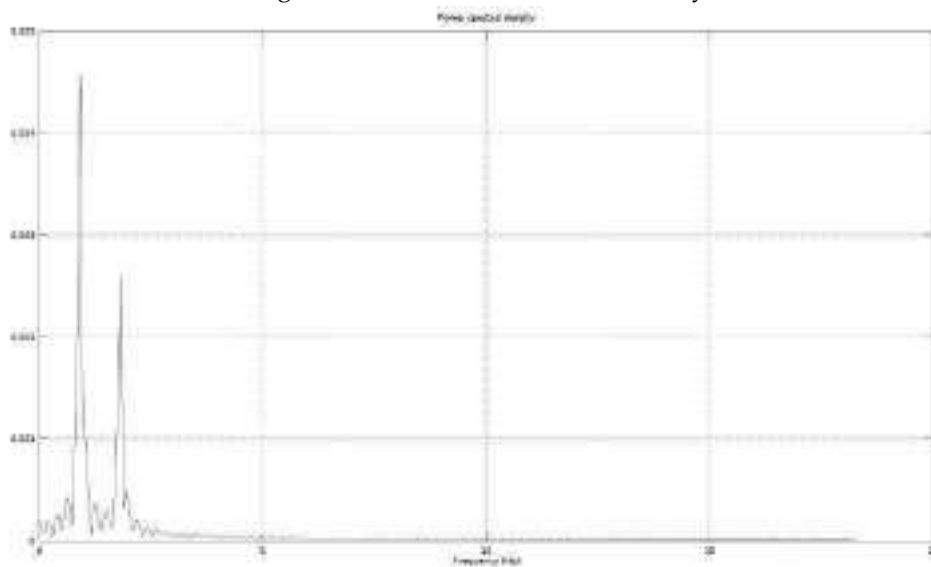


(B) Amplitude spectrum of the vertical displacement signal (see figure A) for a cylinder immersed in horizontal stream at $Re=11000$.

FIGURE A.18: Results for a cylinder immersed in horizontal stream at $Re=11000$

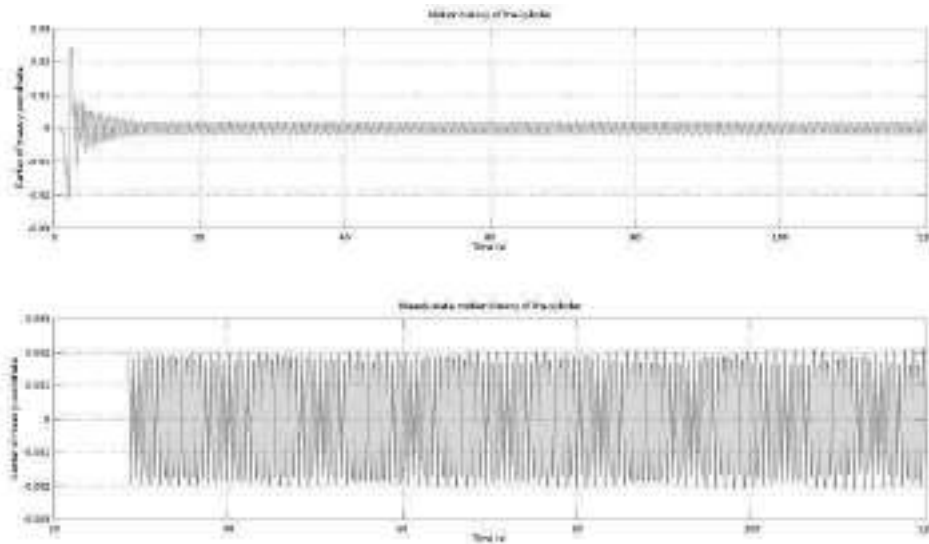


(A) The top plot represent the time history of a vertical displacement of a cylinder immersed in a horizontal stream with $Re=11500$. In the bottom plot we report the final regime solution used for Fourier analysis.

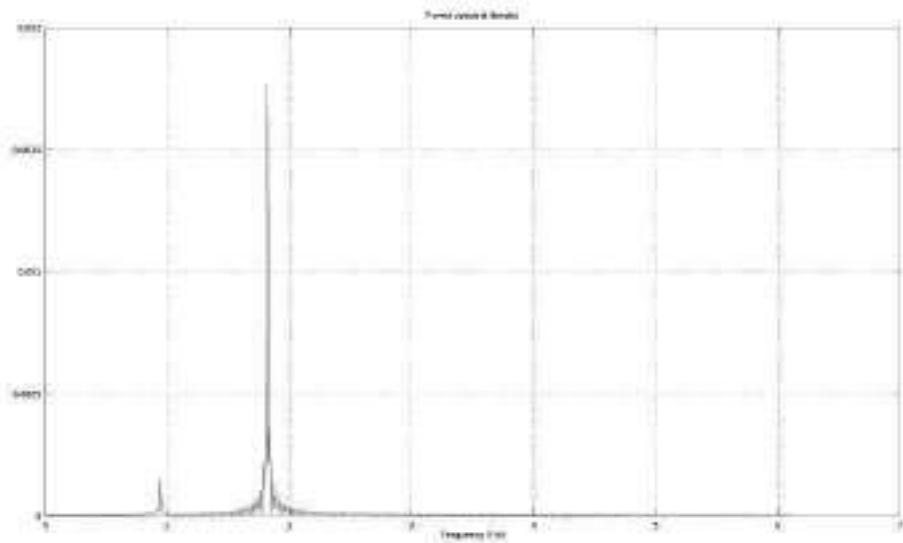


(B) Amplitude spectrum of the vertical displacement signal (see figure A) for a cylinder immersed in horizontal stream at $Re=11500$.

FIGURE A.19: Results for a cylinder immersed in horizontal stream at $Re=11500$

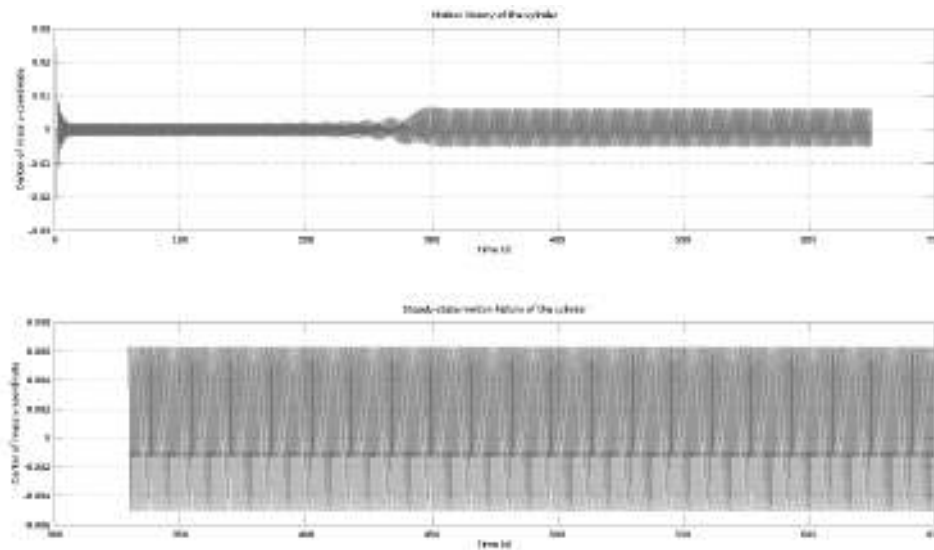


(A) The top plot represent the time history of a vertical displacement of a cylinder immersed in a horizontal stream with $Re=11600$. In the bottom plot we report the final regime solution used for Fourier analysis.

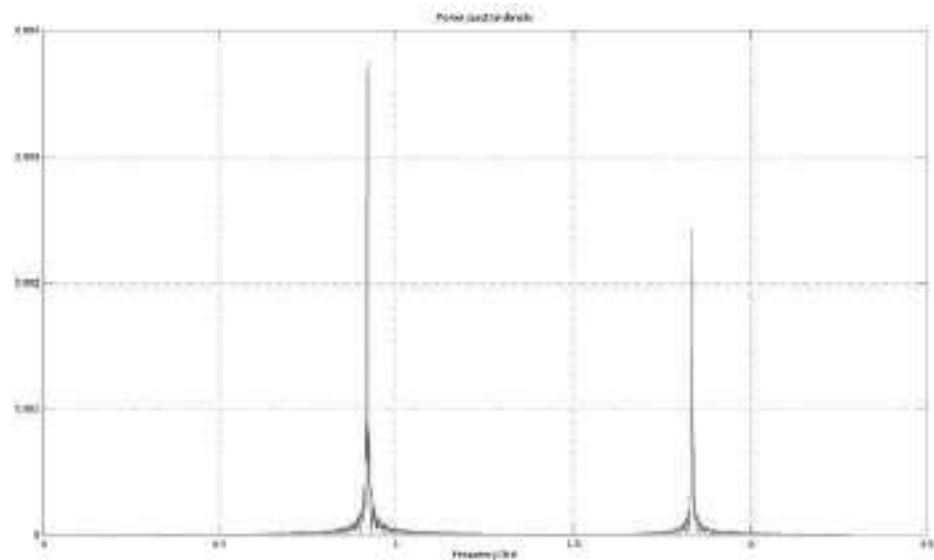


(B) Amplitude spectrum of the vertical displacement signal (see figure A) for a cylinder immersed in horizontal stream at $Re=11600$.

FIGURE A.20: Results for a cylinder immersed in horizontal stream at $Re=11600$

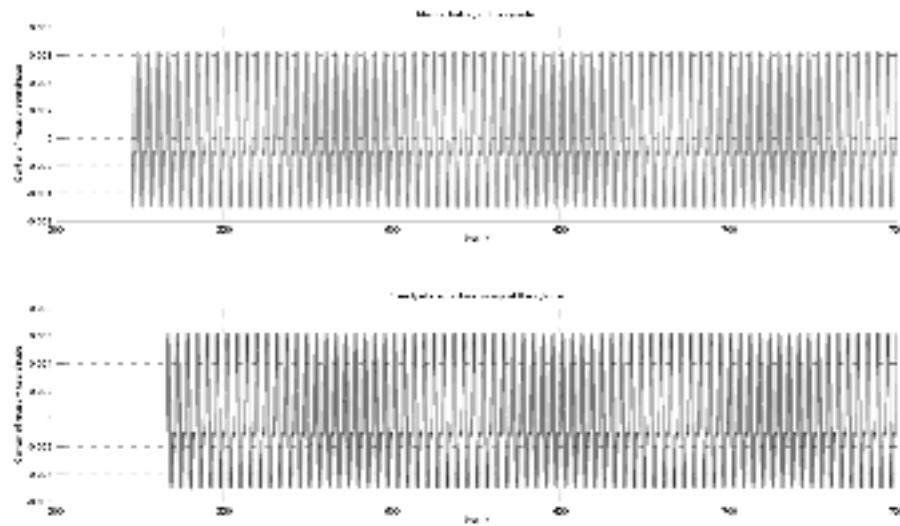


(A) The top plot represent the time history of a vertical displacement of a cylinder immersed in a horizontal stream with $Re=11620$. In the bottom plot we report the final regime solution used for Fourier analysis.

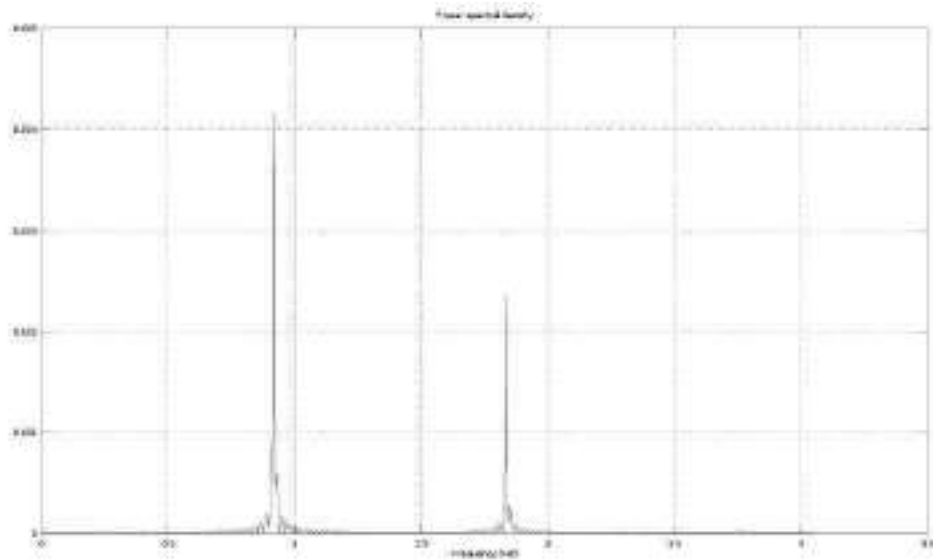


(B) Amplitude spectrum of the vertical displacement signal (see figure A) for a cylinder immersed in horizontal stream at $Re=11620$.

FIGURE A.21: Results for a cylinder immersed in horizontal stream at $Re=11620$

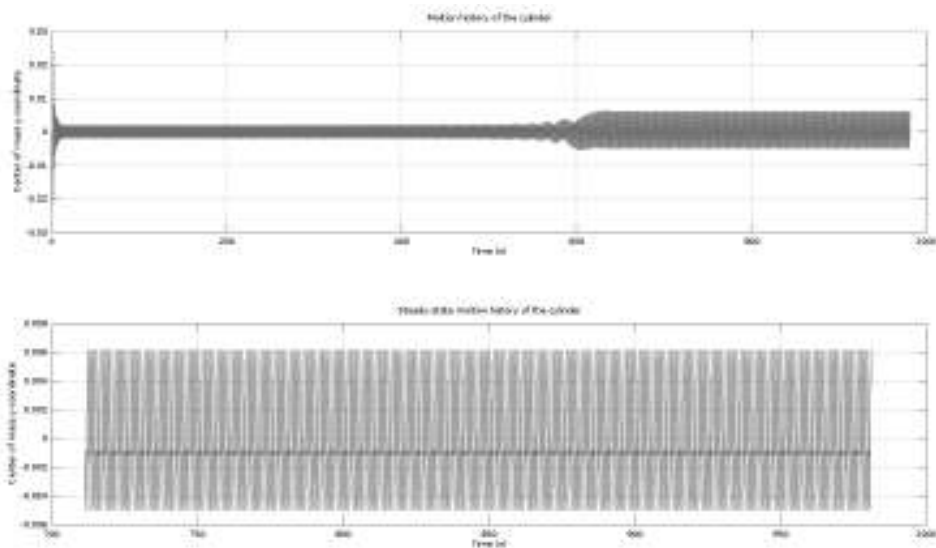


(A) The top plot represent the time history of a vertical displacement of a cylinder immersed in a horizontal stream with $Re=11630$. In the bottom plot we report the final regime solution used for Fourier analysis.

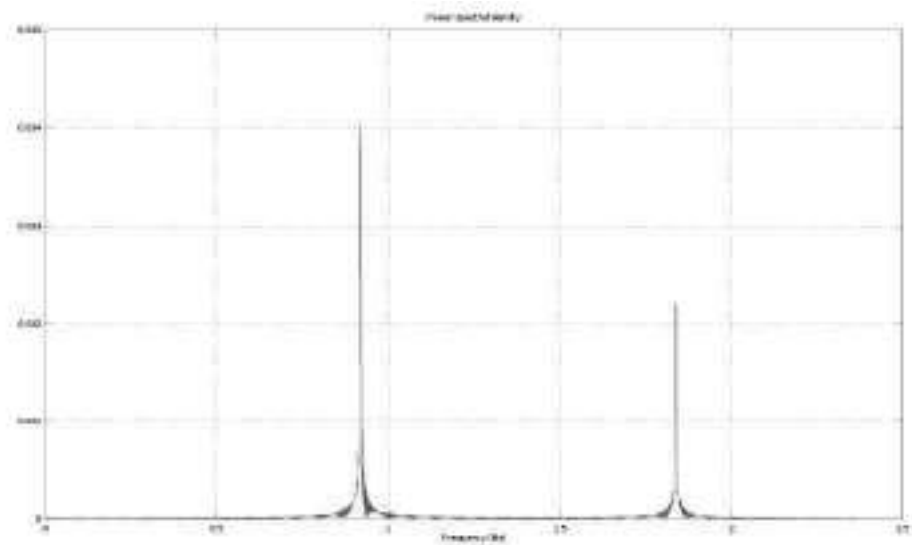


(B) Amplitude spectrum of the vertical displacement signal (see figure A) for a cylinder immersed in horizontal stream at $Re=11630$.

FIGURE A.22: Results for a cylinder immersed in horizontal stream at $Re=11630$

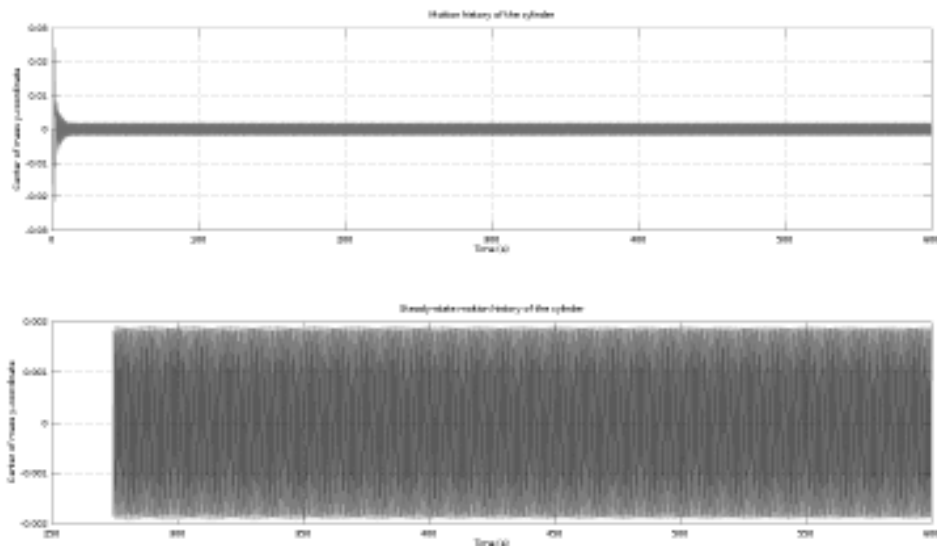


(A) The top plot represent the time history of a vertical displacement of a cylinder immersed in a horizontal stream with $Re=11640$. In the bottom plot we report the final regime solution used for Fourier analysis.

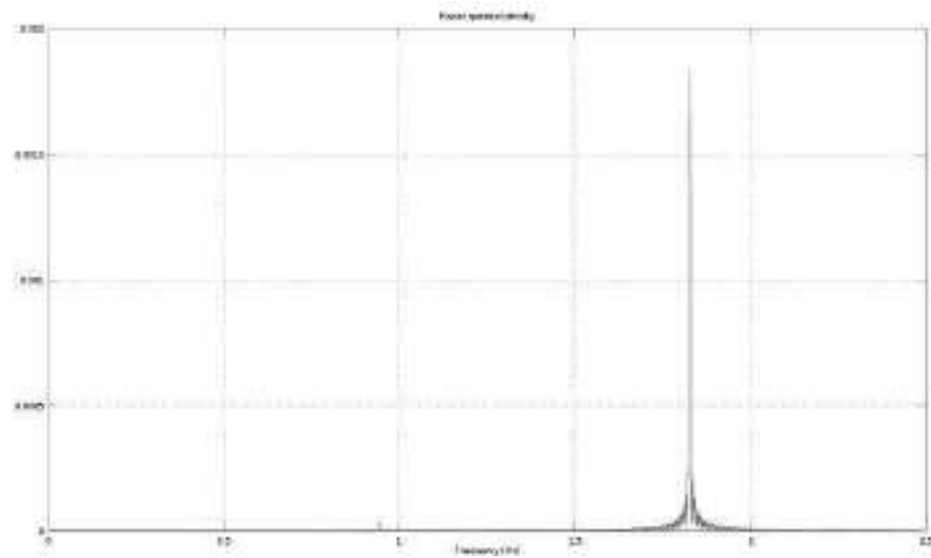


(B) Amplitude spectrum of the vertical displacement signal (see figure A) for a cylinder immersed in horizontal stream at $Re=11640$.

FIGURE A.23: Results for a cylinder immersed in horizontal stream at $Re=11640$

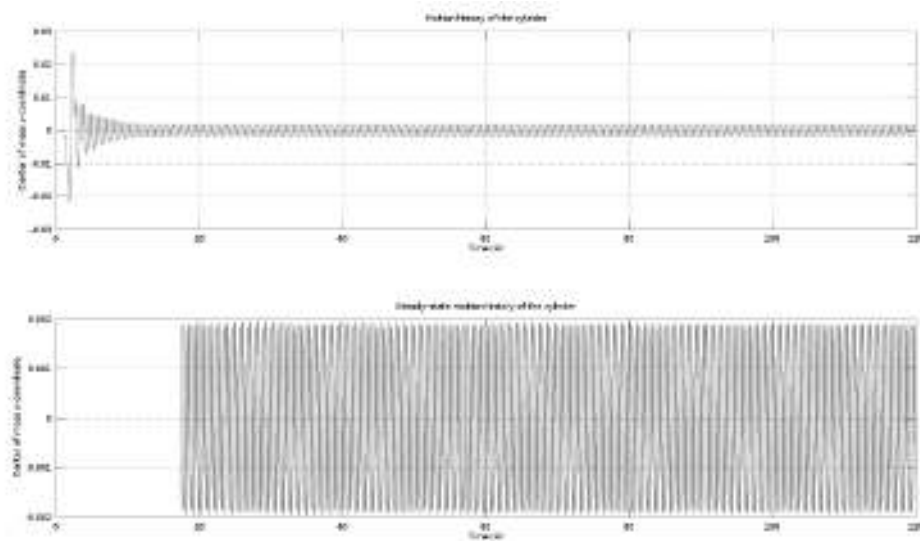


(A) The top plot represent the time history of a vertical displacement of a cylinder immersed in a horizontal stream with $Re=11650$. In the bottom plot we report the final regime solution used for Fourier analysis.

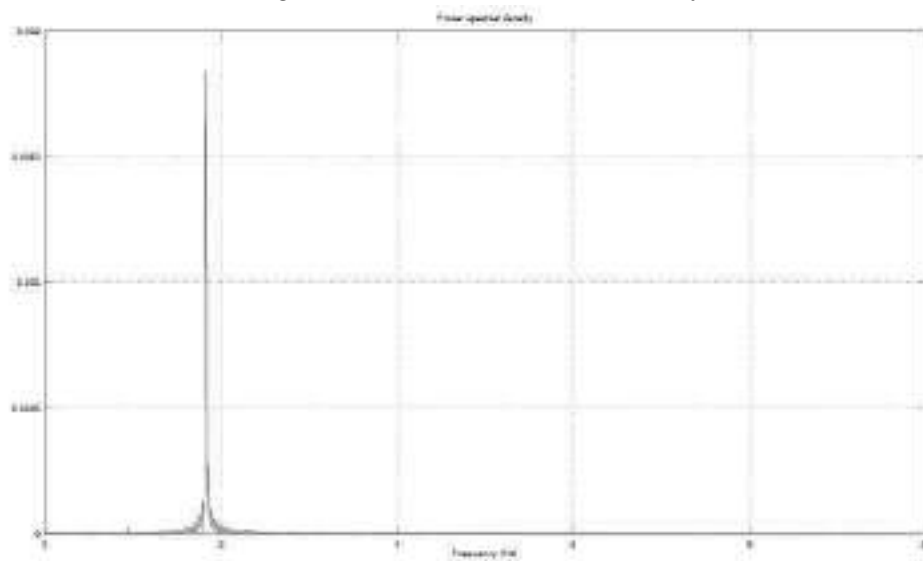


(B) Amplitude spectrum of the vertical displacement signal (see figure A) for a cylinder immersed in horizontal stream at $Re=11650$.

FIGURE A.24: Results for a cylinder immersed in horizontal stream at $Re=11650$

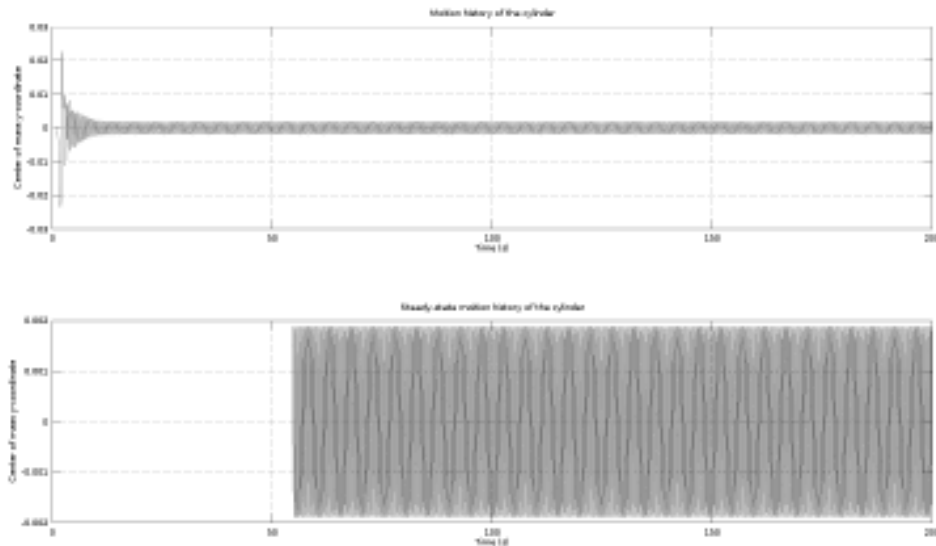


(A) The top plot represent the time history of a vertical displacement of a cylinder immersed in a horizontal stream with $Re=11700$. In the bottom plot we report the final regime solution used for Fourier analysis.

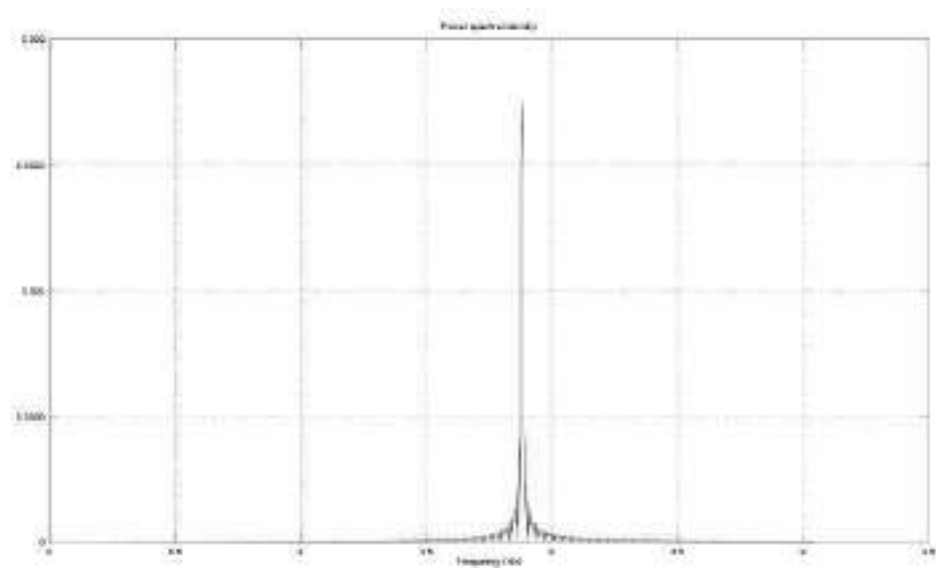


(B) Amplitude spectrum of the vertical displacement signal (see figure A) for a cylinder immersed in horizontal stream at $Re=11700$.

FIGURE A.25: Results for a cylinder immersed in horizontal stream at $Re=11700$

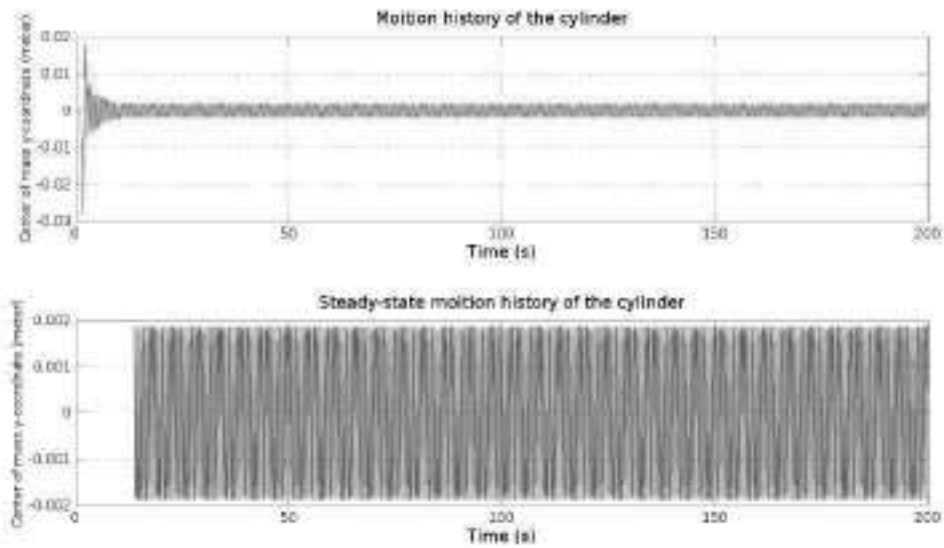


(A) The top plot represent the time history of a vertical displacement of a cylinder immersed in a horizontal stream with $Re=12000$. In the bottom plot we report the final regime solution used for Fourier analysis.

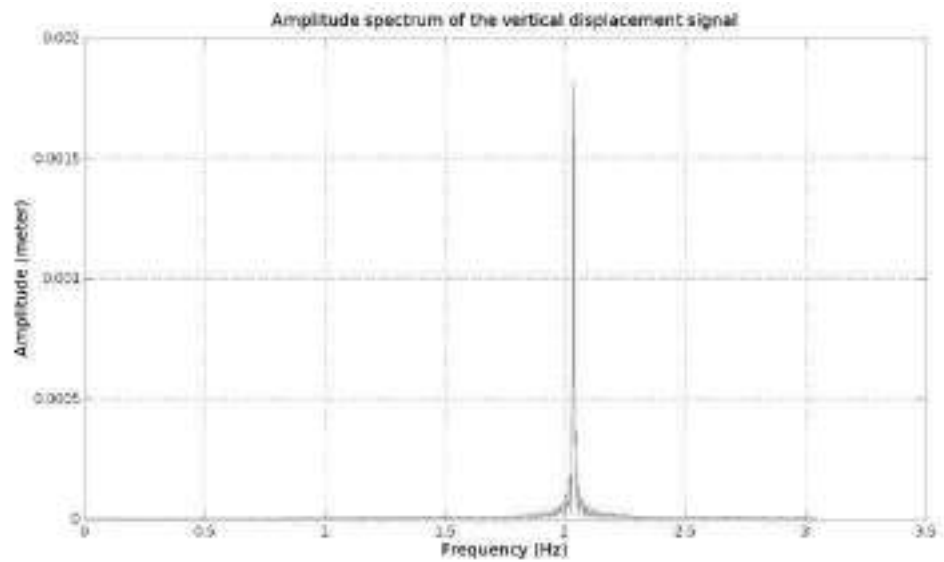


(B) Amplitude spectrum of the vertical displacement signal (see figure A) for a cylinder immersed in horizontal stream at $Re=12000$.

FIGURE A.26: Results for a cylinder immersed in horizontal stream at $Re=12000$



(A) The top plot represent the time history of a vertical displacement of a cylinder immersed in a horizontal stream with $Re=13000$. In the bottom plot we report the final regime solution used for Fourier analysis.



(B) Amplitude spectrum of the vertical displacement signal (see figure A) for a cylinder immersed in horizontal stream at $Re=13000$.

FIGURE A.27: Results for a cylinder immersed in horizontal stream at $Re=12000$

Bibliography

- [1] AKHTAR, I. *Parallel Simulation, Reduced-Order Modeling, and Feedback Control of Vortex Shedding using Fluidic Actuators*. PhD thesis, Virginia Polytechnic Institute and State University, 2008.
- [2] AUBRY, N., HOLMES, P., LUMLEY, J. L., AND STONE, E. The dynamics of coherent structures in the wall region of a turbulent boundary layer. *Journal of Fluid Mechanics* 192 (1988), 115–173.
- [3] BALLARIN, F., MANZONI, A., QUARTERONI, A., AND ROZZA, G. Supremizer stabilization of POD Galerkin approximation of parametrized steady incompressible Navier–Stokes equations. *International Journal for Numerical Methods in Engineering* 102, 5 (2015), 1136–1161.
- [4] BARRETT, A., AND REDDIEN, G. On the reduced basis method. *ZAMM-Journal of Applied Mathematics and Mechanics/Zeitschrift für Angewandte Mathematik und Mechanik* 75, 7 (1995), 543–549.
- [5] BERGMANN, M., BRUNEAU, C.-H., AND IOLLO, A. Enablers for robust POD models. *Journal of Computational Physics* 228, 2 (2009), 516–538.
- [6] BERKOOZ, G., HOLMES, P., AND LUMLEY, J. L. The proper orthogonal decomposition in the analysis of turbulent flows. *Annual review of fluid mechanics* 25, 1 (1993), 539–575.
- [7] BERS, L., BOCHNER, S., AND JOHN, F. *Contributions to the Theory of Partial Differential Equations*.(AM-33), vol. 33. Princeton University Press, 2016.
- [8] BIZON, K., AND CONTINILLO, G. Reduced order modelling of chemical reactors with recycle by means of POD-penalty method. *Computers & Chemical Engineering* 39 (2012), 22–32.
- [9] CHINESTA, F., LADEVEZE, P., AND CUETO, E. A short review on model order reduction based on proper generalized decomposition. *Archives of Computational Methods in Engineering* 18, 4 (2011), 395–404.
- [10] CUONG, N. N., VEROY, K., AND PATERA, A. T. Certified real-time solution of parametrized partial differential equations. In *Handbook of Materials Modeling*. Springer, 2005, pp. 1529–1564.
- [11] DAUTRAY, R., AND LIONS, J.-L. *Mathematical Analysis and Numerical Methods for Science and Technology: Volume 1 Physical Origins and Classical Methods*. Springer Science & Business Media, 2012.
- [12] DROHMANN, M., HAASDONK, B., AND OHLBERGER, M. Reduced basis method for finite volume approximation of evolution equations

- on parametrized geometries. In *Proceedings of ALGORITMY* (2009), vol. 2008, pp. 111–120.
- [13] FACCHINETTI, M. L., DE LANGRE, E., AND BIOLLEY, F. Coupling of structure and wake oscillators in vortex-induced vibrations. *Journal of Fluids and Structures* 19, 2 (2004), 123–140.
- [14] FENG, C. *The measurement of vortex induced effects in flow past stationary and oscillating circular and d-section cylinders*. PhD thesis, University of British Columbia, 1968.
- [15] FLETCHER, C. A. Computational galerkin methods. In *Computational galerkin Methods*. Springer, 1984, pp. 72–85.
- [16] GABBAL, R., AND BENAROYA, H. An overview of modeling and experiments of vortex-induced vibration of circular cylinders. *Journal of Sound and Vibration* 282, 3 (2005), 575–616.
- [17] GALLARDO, D., BEVILACQUA, R., AND SAHNI, O. Data-based hybrid reduced order modeling for vortex-induced nonlinear fluid–structure interaction at low Reynolds numbers. *Journal of Fluids and Structures* 44 (2014), 115–128.
- [18] GOTTLIEB, D., AND ORSZAG, S. A. *Numerical analysis of spectral methods: theory and applications*, vol. 26. Siam, 1977.
- [19] HARTLEN, R. T., AND CURRIE, I. G. Lift-oscillator model of vortex-induced vibration. *Journal of the Engineering Mechanics Division* 96, 5 (1970), 577–591.
- [20] HAUGAN, P. M., EVENSEN, G., JOHANNESSEN, J. A., JOHANNESSEN, O. M., AND PETTERSSON, L. H. Modeled and observed mesoscale circulation and wave-current refraction during the 1988 norwegian continental shelf experiment. *Journal of Geophysical Research: Oceans* 96, C6 (1991), 10487–10506.
- [21] HESTHAVEN, J. S., ROZZA, G., AND STAMM, B. Certified reduced basis methods for parametrized partial differential equations. *Springer-Briefs in Mathematics* (2015).
- [22] HUERTA, A., AND FERNANDEZ MENDEZ, S. Enrichment and coupling of the finite element and meshless methods. *International Journal for Numerical Methods in Engineering* 48, 11 (2000), 1615–1636.
- [23] ISSA, R. I., GOSMAN, A., AND WATKINS, A. The computation of compressible and incompressible recirculating flows by a non-iterative implicit scheme. *Journal of Computational Physics* 62, 1 (1986), 66–82.
- [24] JASAK, H. Error analysis and estimation for finite volume method with applications to fluid flow.
- [25] KHALAK, A., AND WILLIAMSON, C. Dynamics of a hydroelastic cylinder with very low mass and damping. *Journal of Fluids and Structures* 10, 5 (1996), 455–472.

- [26] KHALAK, A., AND WILLIAMSON, C. Fluid forces and dynamics of a hydroelastic structure with very low mass and damping. *Journal of Fluids and Structures* 11, 8 (1997), 973–982.
- [27] KHALAK, A., AND WILLIAMSON, C. Motions, forces and mode transitions in vortex-induced vibrations at low mass-damping. *Journal of fluids and Structures* 13, 7 (1999), 813–851.
- [28] LARSEN, C. M., VIKESTAD, K., YTTERVIK, R., AND PASSANO, E. Empirical model for analysis of vortex induced vibrations-theoretical background and case studies. In *Proceedings of 20th International Conference on Offshore Mechanics and Arctic Engineering, OMAE* (2001), vol. 1.
- [29] LARSEN, C. M., VIKESTAD, K., YTTERVIK, R., PASSANO, E., AND BAARHOLM, G. S. VIVANA–Theory Manual. *Marintek, Trondheim, Norway* (2001).
- [30] LASSILA, T., AND ROZZA, G. Parametric free-form shape design with PDE models and reduced basis method. *Computer Methods in Applied Mechanics and Engineering* 199, 23 (2010), 1583–1592.
- [31] LIENHARD, J. H. *Synopsis of lift, drag, and vortex frequency data for rigid circular cylinders*. Technical Extension Service, Washington State University, 1966.
- [32] LORENZI, S., CAMMI, A., LUZZI, L., AND ROZZA, G. POD-Galerkin method for finite volume approximation of Navier–Stokes and RANS equations. *Computer Methods in Applied Mechanics and Engineering* 311 (2016), 151–179.
- [33] MAINÇON, P. A Wiener-Laguerre model of VIV forces given recent cylinder velocities. *Mathematical Problems in Engineering* 2011 (2011), Article ID 414702, 43 pages.
- [34] MANZONI, A., QUARTERONI, A., AND ROZZA, G. Computational reduction for parametrized PDEs: strategies and applications. *Milan Journal of Mathematics* 80, 2 (2012), 283–309.
- [35] MARTINI, S. Analysis of 2d VIV of a single circular cylinder by an open-source CFD solver. Master’s thesis, Università degli Studi di Trieste, 2016.
- [36] MENTER, F. R. Two-equation eddy-viscosity turbulence models for engineering applications. *AIAA journal* 32, 8 (1994), 1598–1605.
- [37] MURAD, N. M., NASER, J., ALAM, F., AND WATKINS, S. Simulation of vehicle a-pillar aerodynamics using various turbulence models. Tech. rep., SAE Technical Paper, 2004.
- [38] NOACK, B. R., PAPAS, P., AND MONKEWITZ, P. A. The need for a pressure-term representation in empirical Galerkin models of incompressible shear flows. *Journal of Fluid Mechanics* 523 (2005), 339–365.
- [39] PAÏDOUSSIS, M. P., PRICE, S. J., AND DE LANGRE, E. *Fluid-structure interactions: Cross-flow-induced instabilities*. Cambridge University Press, 2010.

- [40] PRUD'HOMME, C., ROVAS, D. V., VEROY, K., MACHIELS, L., MADDAY, Y., PATERA, A. T., AND TURINICI, G. Reliable real-time solution of parametrized partial differential equations: Reduced-basis output bound methods. *Journal of Fluids Engineering* 124, 1 (2002), 70–80.
- [41] QUARTERONI, A., ROZZA, G., AND MANZONI, A. Certified reduced basis approximation for parametrized partial differential equations and applications. *Journal of Mathematics in Industry* 1, 1 (2011), 1.
- [42] QUARTERONI, A., AND VALLI, A. *Numerical approximation of partial differential equations*, vol. 23. Springer Science & Business Media, 2008.
- [43] RAMBO, J., AND JOSHI, Y. Reduced order modeling of steady turbulent convection flows using the POD. In *ASME 2005 Summer Heat Transfer Conference collocated with the ASME 2005 Pacific Rim Technical Conference and Exhibition on Integration and Packaging of MEMS, NEMS, and Electronic Systems (2005)*, American Society of Mechanical Engineers, pp. 837–846.
- [44] RAMBO, J. D. Reduced-order modeling of multiscale turbulent convection: application to data center thermal management.
- [45] RHEINBOLDT, W. C. On the theory and error estimation of the reduced basis method for multi-parameter problems. *Nonlinear Analysis: Theory, Methods & Applications* 21, 11 (1993), 849–858.
- [46] ROSHKO, A. Experiments on the flow past a circular cylinder at very high Reynolds number. *Journal of Fluid Mechanics* 10, 03 (1961), 345–356.
- [47] ROZZA, G. Fundamentals of reduced basis method for problems governed by parametrized PDEs and applications. In *Separated Representations and PGD-Based Model Reduction*. Springer, 2014, pp. 153–227.
- [48] ROZZA, G., HUYNH, D. B. P., AND PATERA, A. T. Reduced basis approximation and a posteriori error estimation for affinely parametrized elliptic coercive partial differential equations. *Archives of Computational Methods in Engineering* 15, 3 (2008), 229–275.
- [49] ROZZA, G., AND VEROY, K. On the stability of the reduced basis method for Stokes equations in parametrized domains. *Computer methods in applied mechanics and engineering* 196, 7 (2007), 1244–1260.
- [50] SALMOIRAGHI, F., BALLARIN, F., CORSI, G., MOLA, A., TEZZELE, M., AND ROZZA, G. Advances in geometrical parametrization and reduced order models and methods for computational fluid dynamics problems in applied sciences and engineering: overview and perspectives. ECCOMAS.
- [51] SARPKEYA, T. Vortex-induced oscillations: a selective review. *Journal of applied mechanics* 46, 2 (1979), 241–258.
- [52] SCRUTON, C. Wind-excited oscillations of tall stacks. *The Engineer* 199, 5185 (1955), 806–808.

- [53] SHARQAWY, M. H., LIENHARD, J. H., AND ZUBAIR, S. M. Thermo-physical properties of seawater: a review of existing correlations and data. *Desalination and Water Treatment* 16, 1-3 (2010), 354–380.
- [54] SIRISUP, S., AND KARNIADAKIS, G. Stability and accuracy of periodic flow solutions obtained by a POD-penalty method. *Physica D: Nonlinear Phenomena* 202, 3 (2005), 218–237.
- [55] SRINIL, N., AND ZANGANEH, H. Modelling of coupled cross-flow /in-line vortex-induced vibrations using double Duffing and van der Pol oscillators. *Ocean Engineering* 53 (2012), 83–97.
- [56] STABILE, G. *A Reduced Order Model for the Dynamics of Long Flexible Cylinders in an offshore environment*. PhD thesis, TU Braunschweig - University of Florence, 2016.
- [57] STROUHAL, E. [experiments of dr. vincenc strouhal at the klementine radiologic facility in prague]. *Sbornik lekarsky* 97, 3 (1995), 429–435.
- [58] SUMER, B. M., AND FREDSE, J. *Hydrodynamics around cylindrical structures*, vol. 12. World Scientific, 1997.
- [59] TRIANTAFYLLOU, M. VIVA extended user’s manual. *Massachusetts Institute of Technology, Department of Ocean Engineering, Cambridge, MA, USA* (2003).
- [60] VANDIVER, J. Dimensionless parameters important to the prediction of vortex-induced vibration of long, flexible cylinders in ocean currents. *Journal of Fluids and Structures* 7, 5 (1993), 423–455.
- [61] VANDIVER, J. K., AND LI, L. SHEAR7 V4. 4 program theoretical manual. *Department of Ocean Engineering, Massachusetts Institute of Technology* (2005).
- [62] VERSTEEG, H. K., AND MALALASEKERA, W. *An introduction to computational fluid dynamics: the finite volume method*. Pearson Education, 2007.
- [63] WANG, Z., AKHTAR, I., BORGGAAARD, J., AND ILIESCU, T. Two-level discretizations of nonlinear closure models for proper orthogonal decomposition. *Journal of Computational Physics* 230, 1 (2011), 126–146.
- [64] WILLCOX, K., AND PERAIRE, J. Balanced model reduction via the proper orthogonal decomposition. *AIAA journal* 40, 11 (2002), 2323–2330.
- [65] ZDRAVKOVICH, M. *Flow around circular cylinders-volume 1: Fundamentals*. 1997.
- [66] ZDRAVKOVICH, M. M. *Flow around Circular Cylinders: Volume 2: Applications*, vol. 2. Oxford University Press, 2003.
- [67] ZHENG, H., PRICE, R., MODARRES-SADEGHI, Y., TRIANTAFYLLOU, G. S., AND TRIANTAFYLLOU, M. S. Vortex-induced vibration analysis (VIVA) based on hydrodynamic databases. In *ASME 2011 30th International Conference on Ocean, Offshore and Arctic Engineering* (2011), American Society of Mechanical Engineers, pp. 657–663.